

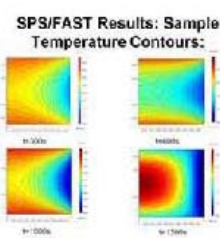
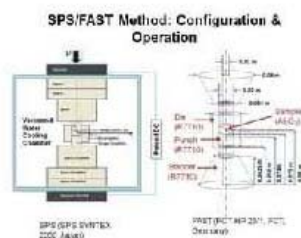
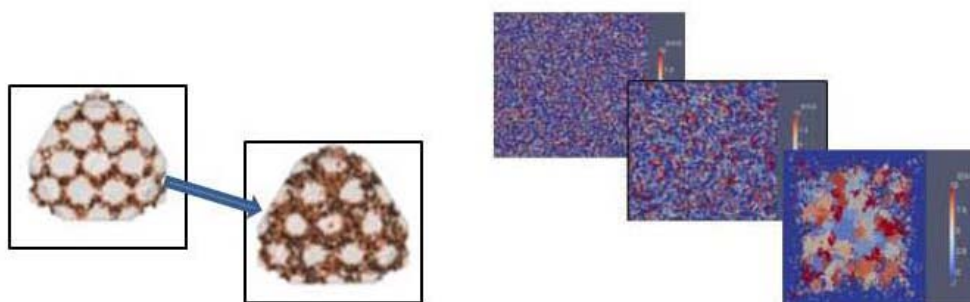


US Army Corps
of Engineers®
Engineer Research and
Development Center

Towards Development of a Super Ceramic Composite - Initial Investigation into Improvement of Strength and Toughness of Polycrystalline Ceramics

John F. Peters, Jeffrey P. Allen, Paul G. Allison,
Thomas A. Carlson, Mei Q. Chandler, Charles F. Cornwell,
Bryce D. Devine, Francis C. Hill, N. Jabari Lee, Charles P. Marsh,
Peter B. Stynoski, Laura Walizer, and Charles R. Welch

August 2012



Towards Development of a Super Ceramic Composite - Initial Investigation into Improvement of Strength and Toughness of Polycrystalline Ceramics

John F. Peters, Paul G. Allison, Mei Q. Chandler, Francis C. Hill, and Laura Walizer

*Geotechnical and Structures Laboratory
U.S. Army Engineer Research and Development Center
3909 Halls Ferry Road
Vicksburg, MS 39180-6199*

Charles P. Marsh, Peter B. Stynoski, and Thomas A. Carlson

*Construction Engineering Research Laboratory
U.S. Army Engineer Research and Development Center
2902 Newmark Drive
Champaign, IL 61822*

Jeffrey B. Allen, Charles F. Cornwell, Bryce D. Devine N. Jabari Lee, and Charles R. Welch

*Information Technology Laboratory
U.S. Army Engineer Research and Development Center
3909 Halls Ferry Road
Vicksburg, MS 39180-6199*

Final report

Approved for public release; distribution is unlimited.

Prepared for U.S. Army Corps of Engineers
Washington, DC 20314-1000

Under U.S. Army Engineer Research and Development Center Directed Research
Program "Nanoscale Studies of Polycrystalline Materials with Emphasis on Ceramics Synthesis," Section 219, Center Directed Research

Abstract

This report outlines the initial findings of the research team conducting the ERDC-directed research project “Nanoscale Studies of Polycrystalline Materials with Emphasis on Ceramics Syntheses.” It provides an assessment of the state-of-the-art in the multi-scale simulation methods that can predict polycrystalline ceramic mechanical properties and ceramic sintering from basic physics and material structure. The report’s findings will be used to identify strengths and weaknesses in the technology, to understand how the different simulation components must fit together, and to guide follow-on research programs towards the long-term development a ceramic composite that has fracture toughness and tensile strength approximately 5 times that of existing polycrystalline ceramics, such as silicon carbide or boron carbide. If such a ceramic composite were developed, then, based on current strength-to-weight and stiffness-to-weight ratios, it could replace steel and aluminum for most structural applications with an attendant two-thirds reduction in weight. This would have enormous impact on Army portable protective structures, equipment, and logistics. Key to this development is the growing capability in numerical simulations to predict material behavior based on atomic and crystalline morphology. Such simulations provide new insight into the causal relationships between material structure and material behavior. The simulations can guide both polycrystalline material design and synthesis methods such as sintering.

DISCLAIMER: The contents of this report are not to be used for advertising, publication, or promotional purposes. Citation of trade names does not constitute an official endorsement or approval of the use of such commercial products. All product names and trademarks cited are the property of their respective owners. The findings of this report are not to be construed as an official Department of the Army position unless so designated by other authorized documents.

DESTROY THIS REPORT WHEN NO LONGER NEEDED. DO NOT RETURN IT TO THE ORIGINATOR.

Contents

Abstract.....	ii
Figures and Tables.....	v
Preface.....	viii
Unit Conversion Factors.....	ix
1 Introduction.....	1
1.1 Multiscale design	4
1.2 Outline of report	7
1.3 Conclusions of 2010 effort.....	7
2 Atomic-Scale Modeling.....	9
2.1 Accurate reactive empirical potentials	10
2.2 Interface between the atomistic simulations and mesoscale simulations.....	12
2.3 Validating atomistic and mesoscale simulation results with experiment	12
2.4 Example: Effects of carbon nanotubes and graphene.....	12
2.5 Challenges	15
2.6 Progress	15
2.7 Technical gaps	17
2.8 Future plans.....	17
3 Modeling of Polycrystalline Materials	19
3.1 Mesoscale modeling methods.....	22
3.1.1 <i>Finite Element Method</i>	22
3.1.2 <i>Peridynamics method</i>	24
3.1.3 <i>Discrete Element Method</i>	26
3.2 Technical gaps in mesoscale modeling.....	32
3.3 High-fidelity 3-D digital microstructure models	33
3.4 Methods for validating the digital models.....	34
3.5 High-fidelity atomistic polycrystalline models.....	36
4 Material Synthesis	40
4.1 Polycrystalline ceramics.....	40
4.2 Sintering methods	41
4.3 SiC synthesis experiments	43
4.4 Product characterization	43
4.5 FY11 tasks	44
4.6 Technical gaps	46
4.7 Carbon nanotube functionalization	46
5 Modeling the Sintering Process	48

5.1	Particle-scale view of sintering	48
5.1.1	<i>Mesocale modeling of solid-state sintering</i>	48
5.1.2	<i>Mesoscale modeling of liquid phase sintering</i>	50
5.1.3	<i>Technical gaps</i>	51
5.2	Modeling the sintering environment	51
5.2.1	<i>Infinite rod</i>	52
5.2.2	<i>Modified Lely method</i>	54
5.2.3	<i>Electromagnetic field</i>	57
5.2.4	<i>Radiation heat transfer</i>	58
5.2.5	<i>Convective heat transfer</i>	60
5.2.6	<i>Numerical method</i>	61
5.2.7	<i>Results</i>	62
5.3	Conclusions	66
5.3.1	<i>Spark plasma sintering</i>	67
6	Material Diagnostics	68
6.1	Material preparation	69
6.2	Results and discussion	73
	References	79

Figures and Tables

Figures

Figure 1. Discrete element models (DEM) of reinforced SiC generated to match atomistic structures simulated in MD—grain for grain, linker for linker. MD and DEM simulations will be run for comparative analyses. Results from MD simulations will be used to parameterize DEMs.	13
Figure 2. Subsequent DEM simulations for reinforced SiC systems at larger length scales, comparable with those of the experiment. Comparative studies may include tests of hardness and tensile strength.	13
Figure 3. In the initial setup, a pristine graphene sheet comprising 480 graphene atoms was positioned near a hot gas composed of 2000 Si and C atoms in a $240\text{\AA} \times 110\text{\AA} \times 100\text{\AA}$ MD cell with periodic boundary conditions on all sides. In the second simulation, 30 percent of the atoms in the graphene sheet were removed to create vacancy defects, but all other setup parameters were the same.	14
Figure 4. Simulations of reinforced SiC grain segment failing under tension. Snapshot sequences show MD simulations of mechanical response of CNT-reinforced SiC grain segments to tensile stress. The purpose is to determine if embedded CNTs can increase tensile strength.	16
Figure 5. Simulations of reinforced SiC grain segment failing under compression. Snapshot sequences show MD simulations of mechanical response of CNT-reinforced SiC grain segments to compressive stress. The aim is to observe the effect of the embedded CNT on hardness.	17
Figure 6. Peridynamic model of a six-grain polycrystal. The colors are applied to distinguish the grains.	27
Figure 7. Peridynamic simulation results. The stiffness between grains is half that inside the grains. The critical stretch between the grains is the same as that inside the grains.	27
Figure 8. Peridynamic simulation results. The stiffness between grains is twice that inside the grains. The critical stretch between grains is the same as that inside the grains.	28
Figure 9. Peridynamic simulation results. The stiffness between grains is the same as that inside the grains. The critical stretch between grains is one-half that inside the grains.	29
Figure 10. Peridynamic simulation results. The stiffness between the grains is the same as that inside the grains. The critical stretch between grains is twice that inside grains.	30
Figure 11. Deformation and internal stress in the vertical direction of a specimen with close random packing. The color denotes the continuum stress at the vertical direction. Red denotes the highest stress.	31
Figure 12. The specimen has close, dense packing, and cohesive bonding force is small.	31
Figure 13. All the parameters are the same as for the specimen shown in Figure 12 except that the cohesive stress is twice that applied in the specimen shown in Figure 12. The color denotes the continuum stress at the vertical direction. Red denotes the highest stress.	32
Figure 14. The material is scanned using an automated EBSD in a Scanning Electron Microscope (SEM), also known as Orientation Imaging Microscopy (OIM) to examine two surfaces of the material.	34

Figure 15. Generation of geometric grain configuration by assigning Voronoi tessellations to ellipsoids.	35
Figure 16. Finite element mesh generated from a sample of aluminum (the model consists of 134 randomly colored grains). The technique can be used to produce microstructure models for finite element simulations and nanostructure models of SiC for atomistic simulations.	36
Figure 17. SiC system with two grains. Grain boundary is 1 nm wide and aligned perpendicular to the z-axis. The system dimensions are 10 x 10 x 10 nm. Both grains have the same crystallographic orientation.	38
Figure 18. SiC system with two grains. Grain boundary is 1 nm wide and the x-axis is rotated 15 deg out of the xy-plane. The system dimensions are 10 x 10 x 10 nm. Both grains have the same crystallographic orientation.	38
Figure 19. SiC system with nine grains: eight grains on the corners and one diamond-shaped grain located at the center. Grain boundaries are 1 nm wide. The system dimensions are 10 x 10 x 10 nm. All of the grains have the same crystallographic orientation.	39
Figure 20. Particle size for various milling times.	43
Figure 21. a-b) SiC disks before CIP. c) Press used to form disks. d) CIP unit.	44
Figure 22. Samples after sintering step.	45
Figure 23. Silica functionalized CNTs made at ERDC – CERL.	47
Figure 24. Harrick plasma cleaner used to functionalize CNTs.	47
Figure 25. Microstructure evolution of a random packing nonuniform powder.	50
Figure 26. Electric potential isolines together with current density vectors.	55
Figure 27. Numerical and analytical results.	55
Figure 28. Schematic of the RF induction heating system for growth of SiC crystals.	56
Figure 29. Computational grid for finite element method.	63
Figure 30. Contours of magnetic potential, out of phase (A_i) and in-phase (A_r), for a current of 1200 Amps and a frequency of 10 kHz.	63
Figure 31. Comparison of generated heat power along the radial direction at different heights with results from Chen et al. (2000).	64
Figure 32. Temperature contours for a current of 1200 A and frequency of 10 kHz.	65
Figure 33. Effect of applying radiation to the numerical simulation.	66
Figure 34. Optical micrograph image of 0.015-in.-thick notch.	70
Figure 35. Loading configuration for SENB specimens.	71
Figure 36. Fracture surface of SENB test specimen.	74
Figure 37. Plot of Young's modulus calculated using Oliver and Pharr (1992) versus peak indentation load. Bars represent maximum and minimum values of each data set.	75
Figure 38. Load versus displacement curves of QS nanoindentation method experiments for a cracked and uncracked test.	75
Figure 39. Oliver and Pharr (1992) calculated hardness versus peak indentation load. Bars represent maximum and minimum values of each data set.	77
Figure 40. XRD pattern of commercially available SiC.	78

Tables

Table 1. Material properties of ceramics compared with steel and aluminum.....	2
Table 2. Loading and support span lengths for the SENB specimens.....	71
Table 3. Polishing of SiC for Nanoindentation.	72
Table 4. Modified Murakami's solution used for etching.	73
Table 5. Mechanical property results for the fracture toughness specimens.....	73

Preface

This report provides an assessment of the state-of-the art in multi-scale numerical simulation methods necessary to model the mechanical properties and the synthesis of polycrystalline ceramics. It identifies strengths and weaknesses in these technologies and how the methods can be used synergistically to develop a fundamental understanding of the underlying phenomena. The findings of this report will be used to guide ERDC's materials development research whose long-term goal is the development of a structural ceramic that can replace steel and aluminum for most applications with significant (two-thirds) weight reduction.

This report is a product of the ERDC-directed research program "Nanoscale Studies of Polycrystalline Materials with Emphasis on Ceramics Syntheses." This program is a joint ITL-GSL-CERL-EL program under co-leads Dr. Charles R. Welch (ITL) and Dr. John F. Peters (GSL). The report was prepared by the research team members identified and was edited by Dr. John Peters. Marsha Gay and Holly Clavien provided technical editing and formatting. The report was prepared under the general direction of the Laboratory Directors of the four ERDC laboratories: Dr. Reed Mosher (ITL), Dr. David Pittman (GSL), Dr. Ilker Adiguzel (CERL), and Dr. Beth Flemming (EL), and under the general supervision of the GSL Technical Director, Dr. David Horner who oversaw ERDC's material development efforts.

COL Kevin Wilson was the Commander of ERDC during the time of this report; the Associate Director of ERDC was Dr. John Cullinane; and the ERDC Executive Director was Dr. Jeffery P. Holland.

Unit Conversion Factors

Multiply	By	To Obtain
degrees Fahrenheit	$(F-32)/1.8$	degrees Celsius
inches	0.0254	meters
pounds (force)	4.448222	newtons
pounds (force) per square inch	6.894757	kilopascals
pounds (mass) per cubic foot	16.01846	kilograms per cubic meter

1 Introduction

This report outlines the findings of the initial phase of the project “Nanoscale Studies of Polycrystalline Materials with Emphasis on Ceramics Syntheses.” The objective of the project is to develop multiscale modeling techniques for polycrystalline ceramic sintering, principally the sintering of silicon carbide (SiC). This research advances the long-term effort to increase the tensile strength and fracture toughness of polycrystalline ceramics to a factor of approximately five that of existing values. Sintering is the process by which polycrystalline ceramics are made from crystalline powder by applying heat, stress, and sometimes electric and magnetic fields. Polycrystalline ceramics offer the promise of superior structural materials having strength-to-weight and stiffness-to-weight ratios that are factors of three or more those of current structural materials such as aluminum and steel. In addition, ceramics retain their properties under high temperature (over 3000 °F),¹ resist corrosion, and are created from abundant materials. Unfortunately, bulk specimens of ceramic materials have low fracture toughness and tensile strength compared with the structural metals, making them unsuitable for many important structural applications. Moreover, it has been the experience of the research community that the mechanical properties of ceramics have not been improved significantly using traditional empirical approaches of manipulating composition, particle characteristics, and sintering properties. A deeper understanding of fundamental processes is required.

Technical ceramics have been around for over a century. SiC, for example, was manufactured and sold by Edward Acheson as early as 1893. It can be made by combining silicon sand and carbon in a graphite electric resistance furnace at temperatures of 1600 to 2500 °C. SiC has a density of 194 lb/ft³, compressive strength of 570 ksi, Young’s modulus of 59.5 million psi, a flexure strength (related to tensile strength) of 80 ksi, and a fracture toughness of 4.6 MPa m^{0.5}.

Fracture toughness is related to brittle behavior—the lower the fracture toughness, the more brittle the material. For comparison, high-strength 7075-T6 aluminum has a fracture toughness of 24 MPa m^{0.5}; 4340 steel, a

¹ A table of factors for converting non-SI units of measurement to SI units can be found on page ix.

very high strength, very tough steel, has a fracture toughness of 50 MPa m^{0.5}; while concrete has a fracture toughness of 0.2 to 1.4 MPa m^{0.5}.

Table 1 compares several common ceramics with high-strength aluminum and very high-strength steel. The ceramics have densities roughly that of aluminum; Young's moduli from four to six times that of aluminum, and compressive strengths from four to seven times that of aluminum. The densities of the ceramics are from one-third to one-half that of the steel; Young's modulus from 1.5 to 2 times that of steel; and compressive strength 1.5 to 3 times that of very high strength 4340 steel alloy. The extreme values for ceramics are the reasons they are used for tool cutting, for high-temperature applications, for aerospace applications, for bearing surfaces, for precision parts, and for armor, among other things. Their low tensile strength and low fracture toughness prevent their use in structures, bridges, vehicles, airplanes, ships, trains, gear sets, turbines, etc.

Table 1. Material properties of ceramics compared with steel and aluminum.

Material	Young's Modulus (Million psi)	Compressive Strength (ksi)	Density (lb/ft³)	Fracture Toughness (MPa m^{0.5})	Bending Strength (ksi)	Maximum Service Temperature (F Degrees)
Silicon Carbide (SiC)	59.5	566	194	4.6	80	3000
Boron Carbide (B ₄ C)	63.8	560	157	3.1	62	1112
Aluminum Oxide (Al ₂ O ₃)	43.5	305	230	3.5	47	3092
High-Strength Steel (4340)	29.7	160 - 200	490	50	160 to 200	(Melting Point - 2600)
Aluminum 7075-T6	10.4	74 - 78	170	24	74-78	(Melting Point - 900)

It is hypothesized (Welch et al., 2009) that if a ceramic matrix is appropriately married to carbon nanotubes or to graphene, the carbon nanotubes or graphene would provide the tensile strength and tensile load-carrying capability to overcome the fracture toughness and tensile weaknesses in ceramics. It is also hypothesized that such a composite would operate on a nanoscale much like steel-reinforced concrete operates on a macroscale, arresting cracking before it can propagate.

The technical literature provides encouraging results to support this hypothesis. The work for the most part is empirical. Karandikar et al. (2008) incorporated carbon fiber and carbon nanotubes into SiC and boron carbide matrices. They report an improvement in the SiC fracture toughness of from 4 to 7 MPa m^{0.5}, a 73 percent increase, although still below the long-term goals of the program. Yamamoto et al. (2008) built a highly homogenous composite of alumina and multiwalled carbon nanotubes that was found to exhibit a 27 percent improvement in bending strength and a 25 percent improvement in fracture toughness to 100 ksi and 5.0 MPa m^{0.5}, respectively. From the work of Steif and Trojnecki (1992) on ceramics, it can be inferred that increases in bending stress correspond to improvements in postyield behavior. Hence both parameter improvements reported by Yamamoto et al. suggest reductions in brittle behavior of the alumina as a result of the multiwalled carbon nanotubes. Kwon et al. (2009) reported aluminum (Al)/carbon nanotube (CNT) composites with tensile strengths that were three times larger than pure aluminum because of the CNT reinforcement.

Xia et al. (2004) constructed a highly ordered multiwalled CNT Al composite and subjected it to nanoindentation. Their analyses determined that the multiwalled CNT members improved the fracture toughness of the material by 5 Mpa-m^{0.5}. They also analyzed the apparent tensile strength of the CNTs in the matrix and the interfacial stresses between matrix and the CNTs and determined values of 15-25 GPa and 40-200 MPa, respectively, for these parameters. Wang et al. (2006) fabricated a CNT-SiC composite using a high-pressure (2 to 8 GPa), high-temperature (1770-1970 K) reactive sintering process. They report a fracture toughness of 6.8-7.1 MPa-m^{0.5} for the composite, well above the nominal values for SiC.

CNTs have improved mechanical performance in the cases cited. However, in some cases the addition of CNTs has produced marginal or inferior mechanical properties, as discussed in Zhan et al. (2003). One potential problem with adding CNTs is the difficulty in dispersing them completely throughout the SiC matrix. Without dispersal, the CNTs clump as a result of van der Waals forces between the molecules, ultimately leading to voids in the final polycrystalline matrix that become sites where fractures initiate to cause brittle failure. Evaluating reports of the success or failure of adding CNTs to enhance strength and toughness of ceramic composites

requires knowing details of how the CNTs were incorporated into the composite and whether they were functionalized beforehand.

The reported gains in mechanical properties indicate the following: performance improvements can be achieved with CNT-enhanced composites, the mechanisms contributing to these improvements are unclear, and the fundamental principles to guide improvements of the magnitude required to meet the longterm goals of this research are lacking. Ceramic researchers have recognized the twin weaknesses of the low tensile strength and brittle behavior of ceramics for decades. Their approach to improving ceramics, as in the studies cited, has been largely empirical, with the development being hit-and-miss and consisting of cycles of build then test; rebuild, test, etc. Their testing approach has largely been at the macroscale. This development approach is common to the historical development taken by most other material developers. Material response usually begins at the nanometer scale. Using only empirical approaches to material response often precludes the development of important understanding of underlying phenomena. Relying on macroscale experiments exacerbates the problem as details of important nanoscale phenomena remain hidden.

The use of atomistic simulations to understand material behavior at the nanoscale, coupled with coarse-grained simulations to propagate that understanding across larger material volumes, provides critical insight into what causes a particular material response. Such simulations must be validated—and in some cases calibrated—with experimental evidence across the same scales. Experiments likewise have error, either systematic or random, and leave gaps in defining important quantities. Simulations help to understand the experiments, define physical quantities that cannot be measured, and help identify experimental error. Thus experiments and simulations complement one another. Both nanoscale material diagnostics and response and multiscale material simulations are developing technologies that are being used as they are being developed. Used together they can change material development from being an evolutionary process to a revolutionary process.

1.1 Multiscale design

Heterogeneous composites such as polycrystalline ceramics must be understood from the perspective of various scales. The fundamental properties of the crystalline materials that make up the composites are

determined at the atomic scale. However, the engineering properties are determined as much by the interaction among crystalline grains as the strength of the grains themselves. Thus, a multiscale approach must be considered. In this report, five scales will be considered, based on the methods used to investigate the physics:

- At the smallest scale, quantum mechanics is needed to understand atomic interactions.
- At the molecular scale, Newtonian mechanics is applicable using potential functions derived from quantum-scale studies to define interatomic forces (e.g., molecular dynamics).
- Although a great deal can be learned about structural response using molecular dynamics (MD), the time scale of mechanical interactions is much shorter than that of diffusive mechanisms, which are important in considering material synthesis. For many processes, MD is simply not feasible and Monte Carlo (MC) methods, which determine equilibrium positions of atoms, must be used.
- At length scales of greater than a few nanometers, atomic models give way to mesoscale models that depict the material as discrete entities whose interactions are described through presumptive laws, either derived from MD computations or directly observed in nanoscale experiments.
- The mesoscale extends into the micron range where so-called continuum scale descriptions are used. The continuum scale refers to the ability to define a representative volume element that is large enough that mechanical interactions between discrete elements of the mesoscale can be homogenized into equivalent continuum properties, which then can be endowed to infinitesimal elements for purposes of engineering analysis.

While not formally considered here, there is also a structural scale in which the material can be idealized as structural elements (plates, beams, etc.) whose mechanics are derived from approximations to the continuum equations.

This report approaches the multiscale problem as consisting of the following steps:

- Given target properties, a mesoscale model is developed of the grain structure. This model spans the range of 10 nm-1 μm . In this step the

- optimal grain structure and required grain boundary properties are determined.
- Molecular dynamics models of the grain boundary are developed to determine the structure required to achieve the properties required. The scales involved are be less than 100 nm.
 - The feasible chemical structures that provide suitable mechanical properties of grain boundaries are determined from Monte Carlo simulations and *ab initio* computations. These simulations will define the pressure-temperature states required to synthesize the materials.
 - Continuum-scale models are used to examine the temperature-pressure regime within the sintering chamber. The scales of these models span the dimensions of the sintering device.
 - The characteristics of the green body (presintered) required to achieve the final material structure are evaluated using experiments and methods similar to granular media. The scale for these investigations is similar to that of the mesoscale modeling.

This process will be modified as necessary to accommodate developments in the research. Note that the process is neither a top-down nor a bottom-up sequence as is often depicted in descriptions of multiscale analysis. Rather, it reflects the process of material design in which material response must be considered in tandem with material synthesis. The properties of the homogenized medium are derived from interactions at the mesoscale. New concepts of nanostructure, derived from studies of biological materials (Buehler 2010; Garcia et al. 2010; Bratzel et al. 2010; Espinosa et al. 2011), provide avenues for advancement in performance that have been exploited but to a limited extent in ceramics research (Rim et al. 2011). Mesoscale analyses can be used to determine the mechanical behavior of proposed structures. Once the pressure and temperature environment favorable to the structure is determined, the issue of creating those conditions at a practical size must be addressed through continuum-scale computations. Finally, issues such as how the green body of granular powder is to be created and how it is to be modified through sintering must be addressed through mesoscale models. Beyond this modeling process, many practical considerations of material synthesis and composition can be addressed only through laboratory experimentation combined with material diagnostics.

1.2 Outline of report

The report is presented in six chapters in the approximate order of the five steps discussed in the previous section. The report is the product of the initial studies with the expectation that the report will be revised as needed as the technology and research progresses. The report is not a detailed description of the methods presented; rather documents the methods investigated, technical gaps identified, and the rationale for future research tasks.

1.3 Conclusions of 2010 effort

The technology necessary for implementing the five-step procedure for modeling improved SiC-based polycrystalline materials has been demonstrated, although several technical gaps remain:

- At the mesoscale the mechanical response of polycrystalline materials can be modeled up to the point of failure. Fracture along grain boundaries can be modeled with finite element technology although trans granular failure is more difficult. Methods proposed for modeling fracture, such as peridynamics, were investigated but their underlying physical foundations were unclear. The present capability is sufficient to compare polycrystalline assemblages in terms of resistance to intergranular failure.
- Molecular dynamics is applicable to assessing the structural response across grain boundaries and the effects of inserting CNT and graphene within the SiC matrix. MD is not suitable for modeling the synthesis process per se because of extreme mismatch between the time-steps that must be used in a stable MD computation and the computational duration required for the synthesis processes to play out. A critical element of the MD work is to find potential functions appropriate for each structure investigated.
- The sintering process can be captured with the so-called Potts model, although much of this work in the literature has been done in two dimensions. To be useful for the present work, three-dimensional (3-D) capabilities are needed. Monte Carlo methods can possibly provide critical information and will be the subject of further investigations.
- Once the ideal sintering conditions are determined, the ability to obtain these conditions in full-scale sintering devices can be evaluated using continuum modeling. A preliminary multiphysics analysis was

- performed to demonstrate this capability, which was documented in a conference presentation and paper (Allen et al., 2011).
- A number of sintering methods were reviewed. The Spark Plasma Sintering (SPS) , which is also known as the Field Assisted Sintering Technology (FAST) was identified as the focus of future laboratory efforts because SPS with its attendant lower sintering temperatures and faster sintering times was successful in producing SiC-CNT composites in which the CNTs remained intact (Inam et al., 2010). One intriguing aspect of SPS and CNTs is the apparent ability of the CNTs to act as a sintering aid, producing smaller crystalline grains in the composite.

An impression gained from the work of 2010 is that beyond a brute-force reinforcing of grain boundaries using CNT or graphene, the goal of increasing both strength and toughness can be met only by manipulating the polycrystalline structure. Previous studies using particle methods to study the nanogranular behavior of C–S–H (C=CaO, H=H₂O, S=SiO₂) in cement showed the brittle nature of equidimensional (nearly spherical) grains (Chandler et al. 2009). Comparison to biological materials further suggests that composites of strong and weak components are required for toughness. Thus, key questions are what structure is suitable and how might that structure be obtained?

2 Atomic-Scale Modeling

The purpose of atomic-scale modeling in this research is to use atomistic-scale and mesoscale simulation to study materials processing by linking the performance of high-performance materials with the thermo-mechanical processing steps required to produce them. This chapter discusses the atomistic modeling and simulation progress of polycrystalline materials synthesis by researchers at the U.S. Army Engineer Research and Development Center to date, which has focused on identifying the requirements for modeling the synthesis of ceramic polycrystalline materials at the atomic level. This chapter also presents plans for future research.

In recent years, significant progress in modeling the structural evolution of materials during processing has been made. These advances have been primarily in application of continuum methods where phenomenological constitutive relations are used to describe how a material will behave. These methods can be used to predict the final shape of a specimen following deformation processing and its temperature history. However, these models have had little impact on material design because they cannot quantitatively determine, predict, or manipulate the internal structure of the material. Novel materials are often manufactured via advanced processing techniques that greatly influence the structure of the material and thus its mechanical properties. It is the internal structure that controls the properties of a material, and it is the primary mechanism that materials scientists and engineers have to optimize material properties. Material optimization requires researchers to develop new material models that link theories for the properties and performance of materials with the thermo-mechanical processing steps required to produce them. Ideally, these models will be based upon understanding the relationship between composition, structure, and properties and the ability to process materials to achieve target compositions and structure.

Molecular dynamics simulations are used to determine the structural response at the atomistic scale and thus provide data to formulate constitutive equations for the coarse-grained simulations. For example, the structural response across grain boundaries can be modeled to atomic fidelity using MD; in coarse-grained simulations the boundary would be

modeled as simple finite elements having properties derived from the small-scale MD simulation.

MD can be applied to understanding synthesis processes to some extent, but is greatly limited in this application because of the time scales involved. To meet requirements for stability and accuracy, the time-step for MD is small relative to the time required to capture diffusion processes associated with synthesis processes. Also, for sintering processes, the length scale of individual grains makes the application of MD nearly intractable, giving rise to alternative techniques described in Chapter 5.

Critical to accurate MD simulations are the potentials that define the forces associated with atomic interactions. These potentials are not fundamental in the sense that the potential is not a direct result of quantum mechanical computations. Rather, the potentials are empirical relationships that are inferred from a combination of experimental and computational results. It is common to base the potential on binary interactions between atoms, although it is often necessary to consider multiple bond potentials. The selection of the appropriate potential is central to the science of MD; no general atomic potentials fit all cases.

A review of literature has identified several technical challenges involved with the design and development of advanced materials at the nanoscale to mesoscale:

- Develop accurate reactive empirical potentials.
- Develop high-fidelity 3-D digital microstructure models.
- Develop methods for validating the digital models.
- Develop high-fidelity atomistic polycrystalline models.
- Define the interface between the atomistic simulations and mesoscale simulations.
- Develop methods for validating atomistic and mesoscale simulation results with experiment.

2.1 Accurate reactive empirical potentials

The computation resources required to run *ab initio* MD simulations on systems containing millions of atoms are prohibitive. Classical potentials do not suffer from the same computational restrictions as the *ab initio* MD simulations. However, because the classical potentials are only model representations of interatomic interactions, classical simulations are

limited by the accuracy of these models. For these models to be useful, they must reproduce as closely as possible the experimental or *ab initio* information that is used to produce them. Attempts have been made to develop empirical potentials that are “transferable,” i.e., force field parameters fit for a given set of elements, and then expect the same force field parameters to give valid results for completely different sets of elements. Another approach is to develop a systematic parameter optimization scheme that can generate the force fields for a wide variety of molecular systems.

Reactive empirical potentials, potentials capable of making and breaking chemical bonds during a simulation, are required for molecular dynamics simulation of chemical reactions that take place during the sintering process. Various reactive empirical potentials have been evaluated to determine their suitability for modeling the sintering of SiC. James Lill (2010) evaluated the Reactive Empirical Bond Order potentials of Brenner (Brenner 1990); the Adaptive Intermolecular Reactive Empirical Bond Order (AIREBO) and the potentials of Stuart et al. (2000); as well as the Bond Order (BO) potentials of Professor David Pettifor (Pettifor 1989). Potentials developed by Yu, et al. (2007) (Shan_2010) and the Charge Optimized Many Body (COMB) potential that allows for dynamical electron transfer and bonding were also examined, in addition to the ReaxFF formalism developed by Professor William Goddard and Associate Professor Adri van Duin. ReaxFF (van Duin et al. 2001; Chenoweth et al. 2008) is perhaps the most sophisticated reactive force field yet proposed.

Currently, the Tersoff potential in Large-scale Atomic/Molecular Massively Parallel Simulator (LAMMPS) (Plimpton 1995) is being used to run the atomistic simulations on SiC. Based on Lill’s Reactive Potential Survey, the project “Using AIREBO Potentials to Optimize Properties of SiC Composites Reinforced with Carbon Nanotubes” (Lill et al. 2011) was initiated to develop an optimized parameter set for modeling the sintering of SiC using AIREBO potential. This work will develop new AIREBO force fields to support ERDC’s “Super Carbon Nanotube Tensile and Compressive Infrastructure Materials” project designed to develop “super” composite materials with dramatically improved compressive strengths, tensile strengths, and stiffness, as well as strength-to-weight and stiffness-to-weight ratios. Deliverables will include the following:

- Incorporation of new AIREBO force fields into LAMMPS

- Other enhancements to LAMMPS and Vienna Ab initio Simulation Package (VASP) including an option to perform constant-temperature, constant-stress (NST) dynamics
- The development of a training set to be used with a Multiple Objective Evolution Strategies (MOES) to evolve optimized AIREBO parameter sets
- Optimized AIREBO force fields for the SiC + CNT system

2.2 Interface between the atomistic simulations and mesoscale simulations

The validation between the atomistic and mesoscale simulations has not yet started in the ERDC research program. A target system size has been selected with which to conduct the validation. A system containing 3 by 3 by 3 10-mm grains each was selected as the system size that would be modeled for both the atomistic and mesoscale simulations (Figure 1).

2.3 Validating atomistic and mesoscale simulation results with experiment

The atomistic simulations are progressing to the point of coupling them with the mesoscale models. The experimental work is progressing independent of the simulations for now. The preliminary validation between the atomistic and mesoscale simulations with experimental results has started (Figure 2) and will continue to be updated as the software for constructing the 3-D digital models is progresses and the sintering capabilities have been developed.

2.4 Example: Effects of carbon nanotubes and graphene

SiC is a remarkably hard and strong ceramic material consisting of tetrahedral structures of carbon and silicon. Graphene is a one-atom-thick planar sheet of carbon atoms arranged on a hexagonal crystal lattice. Sp^2 bonds connect carbon atoms in graphene, which are the strongest bonds found in nature. As of 2009, graphene and carbon nanotubes appear the strongest material ever tested, with tensile strengths of about 105 GPa (15.5-million psi), or 150 times that of high-strength steel.

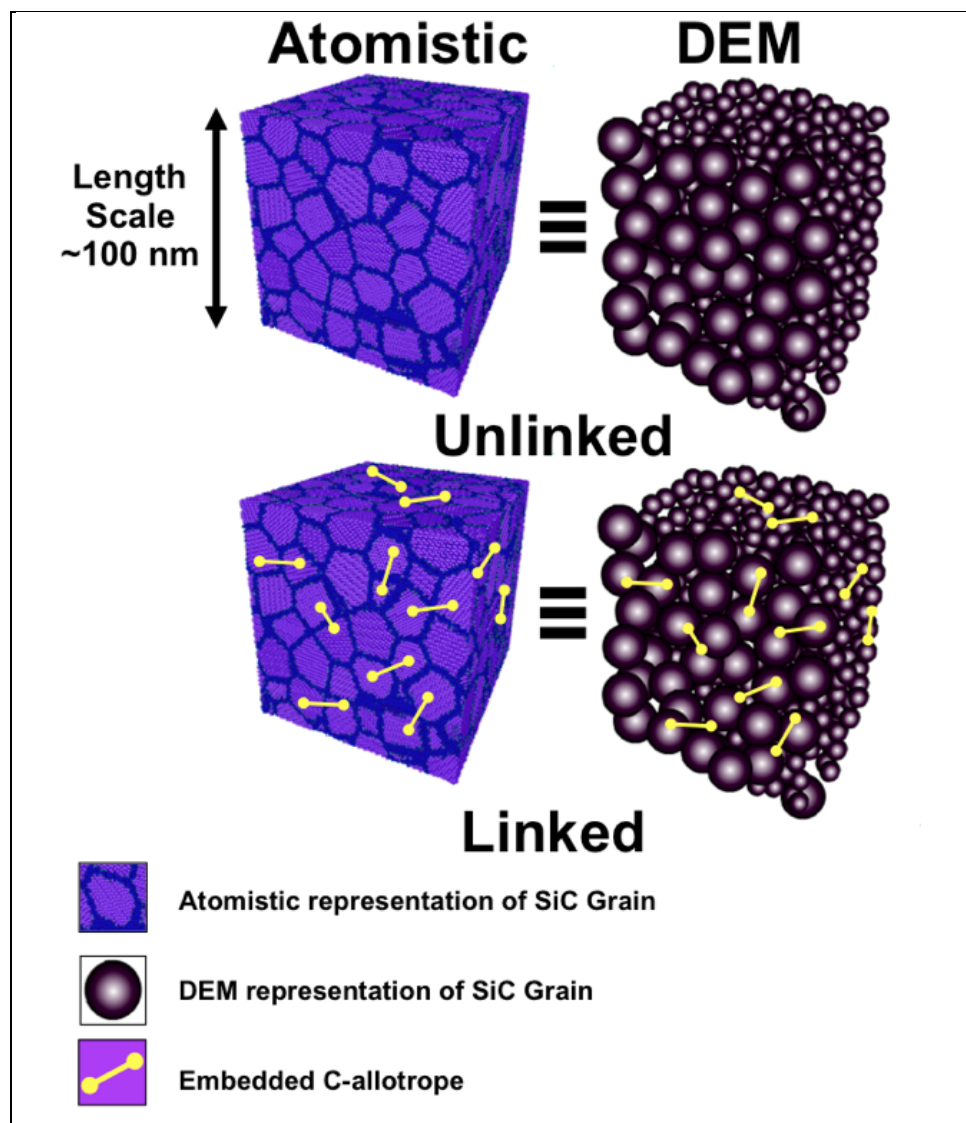


Figure 1. Discrete element models (DEM) of reinforced SiC generated to match atomistic structures simulated in MD—grain for grain, linker for linker. MD and DEM simulations will be run for comparative analyses. Results from MD simulations will be used to parameterize DEMs.

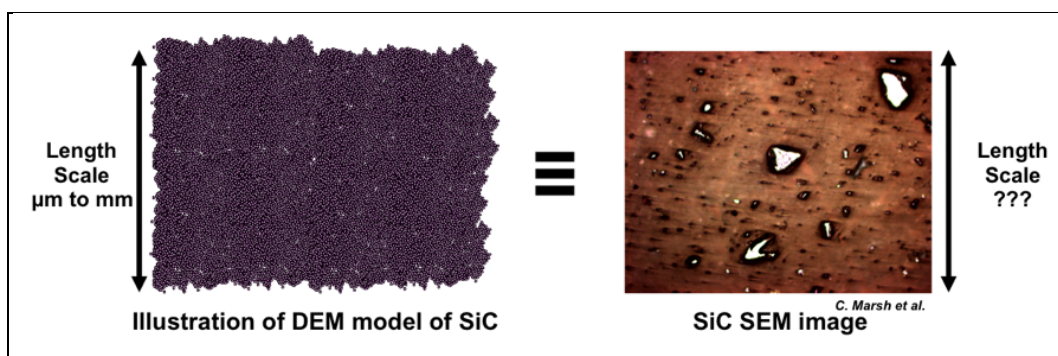


Figure 2. Subsequent DEM simulations for reinforced SiC systems at larger length scales, comparable with those of the experiment. Comparative studies may include tests of hardness and tensile strength.

Results from preliminary studies carried out at the Information Technology Laboratory, Vicksburg, MS, of the U.S. Army Engineer Research and Development Center suggest it might be feasible to synthesize graphene-embedded SiC composites with deposition methods. Classical MD simulations were performed to study the re-depositing sublimated SiC on pristine and porous sheets of graphene (Figure 3).

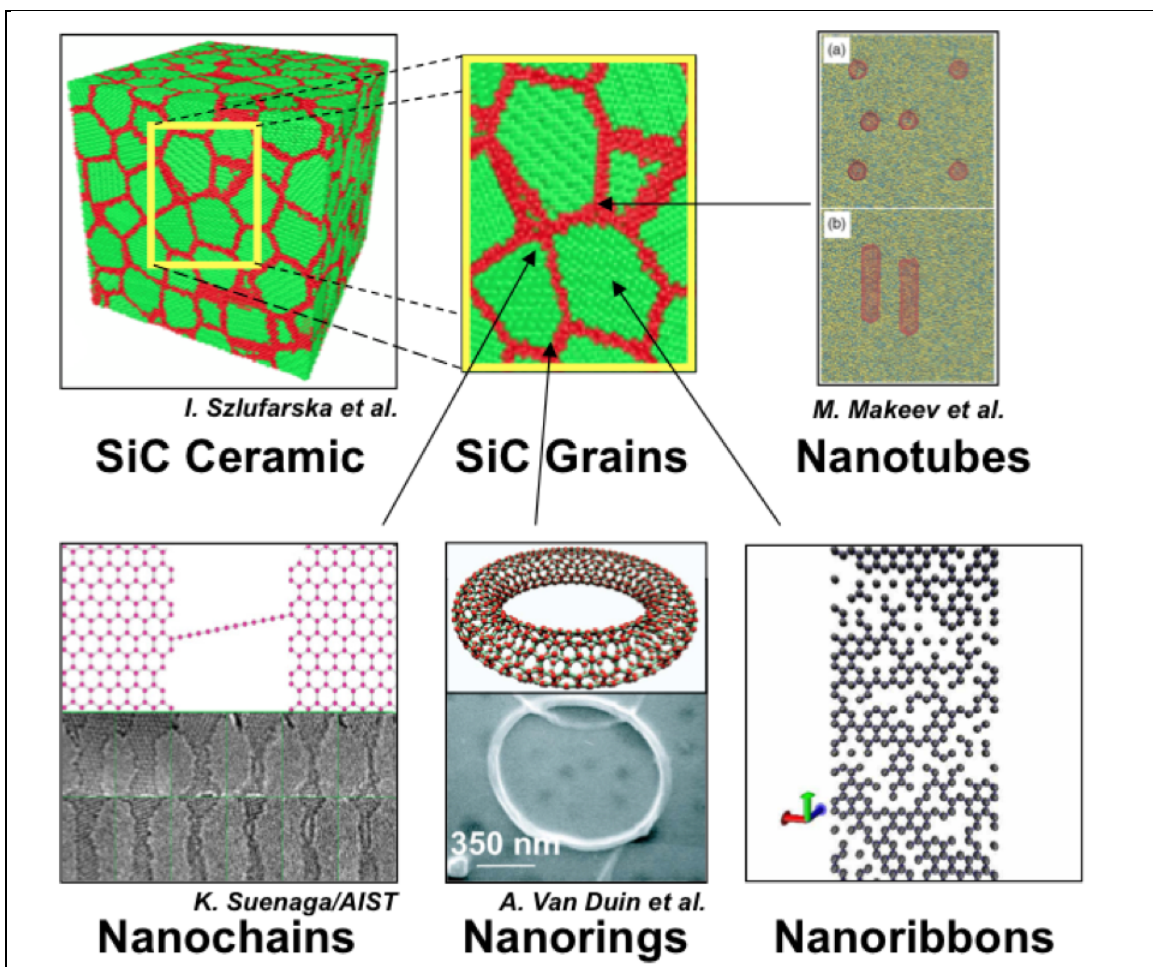


Figure 3. In the initial setup, a pristine graphene sheet comprising 480 graphene atoms was positioned near a hot gas composed of 2000 Si and C atoms in a $240\text{\AA} \times 110\text{\AA} \times 100\text{\AA}$ MD cell with periodic boundary conditions on all sides. In the second simulation, 30 percent of the atoms in the graphene sheet were removed to create vacancy defects, but all other setup parameters were the same.

Each simulation time-step (ts) is equal to 1 femto second (fs) in real time ($1\text{ ts} = 1\text{ fs}$). One million time-steps are required to simulate 1.0 ns in real time. Each simulation ran for a total of ~ 1.2 ns. Temperature was maintained between 1000 and 2000 K, well within the solid-phase regime for SiC. Monoatomic Si and C were observed to nucleate at the edges of pristine graphene, and at the edges and vacancy defects of porous

graphene. Smaller nanoparticles rapidly precipitated (in < 1 ns) from the gas to aggregate around the graphene as well.

It is expected that this process will continue and that solid polycrystalline matrices of SiC will eventually form around graphene, wherein strips of graphene will interlace through multiple crystalline domains.

It is hypothesized that when compressed and sintered, interlacing and possibly interconnecting strips of graphene will reinforce the SiC matrix to increase the toughness or tensile strength of the overall structure.

2.5 Challenges

Challenges would involve optimizing graphene strip width, length, distribution, and interconnectivity for greater tensile strength while avoiding fragmentation of the SiC matrix; and optimizing SiC grain size and morphology to maintain compressive strength and hardness. Classical MD can be used to investigate the mechanical properties in reinforced SiC composites at the nanoscale, and particularly how SiC might be engineered at the nanoscale to resist fracture.

What is not clear is how the presence of the graphene between the grains might affect the structure of the grain boundary region. Typically, the atomic structure within the grain boundary is amorphous, possibly because it represents a linkage between the mismatch in crystalline structures of the two grains making up the boundary. How will the presence of the crystalline graphene within the normally amorphous region affect this structure? Will the graphene affect the strength and toughness of the grain boundary beyond acting as a simple tensile element? Atomic-scale studies can complement experimental efforts to answer these questions (Walker et al. 2011).

2.6 Progress

Molecular dynamics simulations have been performed to study structural and mechanical properties of graphene-based SiC ceramics. SiC exhibits exceptional compressive strength and hardness, but poor tensile strength and fracture toughness. Graphene is currently accepted as the strongest material ever tested, with tensile strength 200 times greater than steel. This research seeks to address challenges in the development of

graphene-embedded SiC ceramic composites with significantly increased tensile strength and fracture toughness.

Graphene dissociates at 2800 °C, while SiC vaporizes at 2750 °C. It is believed that within this temperature range particular mixtures of gaseous SiC and graphene can combine, condense, and be annealed into graphene-interlaced SiC composites with enhanced mechanical properties. The relationships between atomic structure and mechanical properties need to be understood to determine whether interlacing SiC grains with C-allotropes can increase tensile strength, similar to rebar in concrete or straw in adobe. How hardness and compressive strength of SiC are affected when various C-allotropes are embedded needs to be determined.

Images in Figures 4 and 5 are snapshots from some of the first simulations carried out to investigate the mechanical response of CNT-reinforced SiC. They show two slab-shaped wurzite crystal grain segments, separated vertically by an amorphous layer of SiC, interlinked by a (26,0) CNT 20Å in diameter and 8Å in length. The 0001 directions of the crystals in each of the grain segments are aligned for this case. The system consists of ~50,000 Si and C atoms. Since the effect of Hall-Petch hardening is greatest in SiC when the average grain diameter is between 5 nm and 20 nm, the dimensions of the segments were chosen to explore this range.

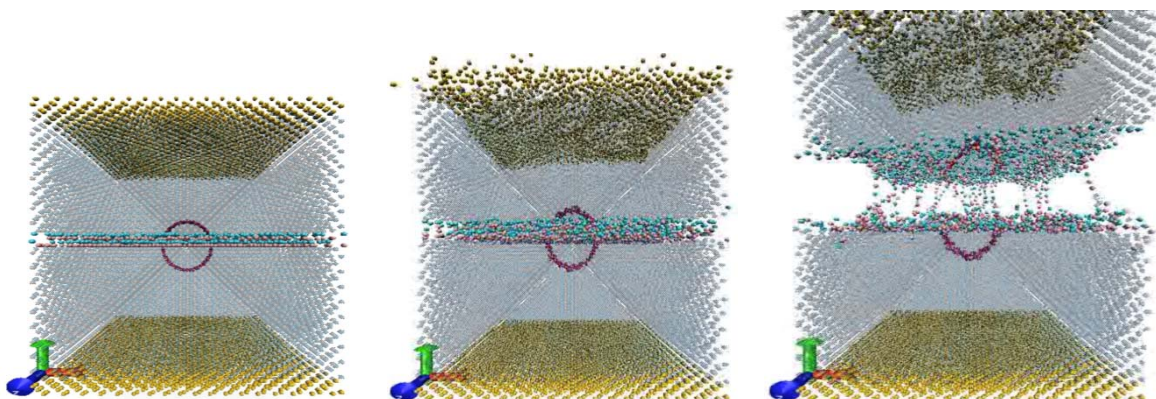


Figure 4. Simulations of reinforced SiC grain segment failing under tension. Snapshot sequences show MD simulations of mechanical response of CNT-reinforced SiC grain segments to tensile stress. The purpose is to determine if embedded CNTs can increase tensile strength.

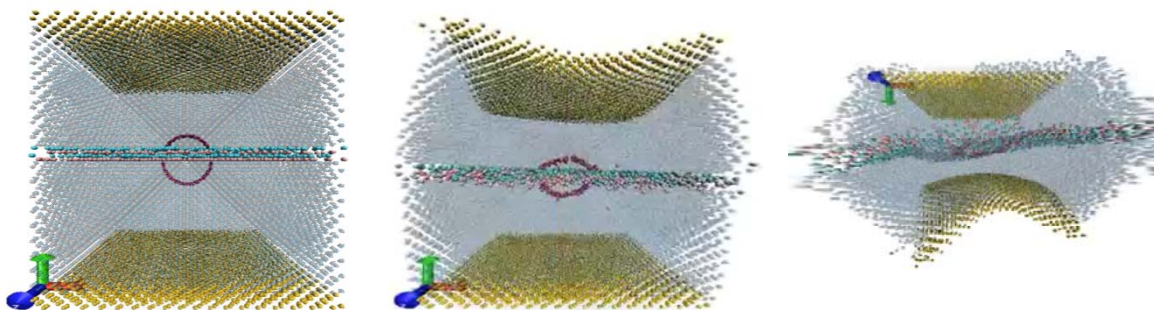


Figure 5. Simulations of reinforced SiC grain segment failing under compression. Snapshot sequences show MD simulations of mechanical response of CNT-reinforced SiC grain segments to compressive stress. The aim is to observe the effect of the embedded CNT on hardness.

Figure 4 shows the SiC-reinforced segment in initial, intermediate, and final points in time. Separation initiates at the amorphous buffer and continues across the amorphous interface until the two segments are separated. Likewise, Figure 5 shows the SiC-reinforced segment under compression to understand how the inserted CNT affects the overall hardness of the material. Simulations are still ongoing to study the effects of CNTs of different sizes and numbers on fracture in SiC.

2.7 Technical gaps

Nanotechnology is a relatively new discipline in materials science. Most of the technical gaps are associated with the ability to study and control materials with atomic and molecular precision, described as follows:

- Experimental gaps in the ability to characterize the atomic structure and composition of materials.
- Simulation gaps in the ability to construct high-fidelity 3-D digital models.
- Computational gaps in the reactive empirical potentials.
- Gaps in the ability to conduct verification and validation on all levels.

2.8 Future plans

The work described in this chapter is still in progress, and it will take most of FY11 to complete. In FY11, simulations using the models will begin as they become available. This should happen toward the end of the second quarter of FY11 with the simulation of the interaction between particles of differing size, grain-grain interactions, and the effect of grain boundary size and composition of grain growth during sintering. Virtual experiments

can be conducted once the MBuilder and atomistic model results are available. Simulations of CNT and CNT fibers embedded in a SiC matrix will be the last thing to come online, and simulations of these systems probably will not start until the end of FY11.

The software developed during FY11 will form the basis for all future simulations. This software must be robust enough to capture all modeling requirements for future simulations. The objective of the modeling and simulations is to support experimental efforts to understand and control the sintering process. One of the most challenging components of nanotechnology is the precise control of the atomic and molecular structure of the material during processing. The same level of precision is required for characterizing the materials and construction for the 3-D digital representation of the materials used in the simulations.

3 Modeling of Polycrystalline Materials

The mesoscale represents the scale that is larger than atomic scale, yet like the atomic scale, is composed of interacting discrete components, each consisting of millions of atoms. In many respects, mesoscale mechanics is similar to granular mechanics in that the mechanical response is as much controlled by interactions between discrete objects as by the atomic makeup of the objects themselves. The atomic interaction controls how the grains are formed and the nature of the grain boundary; but once formed, the mechanical response depends on the interaction of the grains.

To design materials to achieve properties for specific applications, a large number of parameters have to be evaluated. An experimental approach based on trial-error becomes prohibitively time-consuming and expensive, making attractive an approach based on numerical simulations. Numerical simulations have the advantage of being simpler and cheaper, but provide data about details not assessable through experimental measurement. Ideally, MD models that include all the atoms should be used to capture the material responses fully. However, such comprehensive MD models are not feasible considering the expense and limitation of computational power. As an alternative, mesoscale models focus on the size, shape, orientation and spatial arrangement of individual components and the properties and characteristics of interaction between components in lieu of modeling all atoms explicitly.

The granular nature of the mesoscale is derived from the scale of the heterogeneity whereby atomic attractions acting at the boundaries between discrete components are much smaller than those between atoms within the bulk of the components. In a general sense, therefore, materials at the mesoscale may be considered to be large assemblies of components or grains of different sizes, shapes, orientations, and compositions that are bonded together to form continuous bulk materials. The sizes of the components can range from nanometers to millimeters. The properties and performances of the materials result from an amalgam of properties and responses of individual components and, equally important, interactions between components. The size, shape, compositions, orientation, and spatial arrangement of individual components and the properties and

characteristics of interaction between components determine the strength, fracture toughness, ductility, and fatigue life of a material (Groeber et al. 2008), often to a greater extent than the properties of the components themselves. In that sense, mesoscale has a great deal in common with granular mechanics, and many of the methods used to model granular media are equally applicable to modeling the mesoscale.

For polycrystalline materials, the Hall-Petch effect, in which the yield strength of many materials increases with the decrease of grain sizes by increasing dislocation pileups at the grain boundaries, is reversed when the sizes of grains fall into the 10- to 100-nm range. At this point the deformation mechanisms change from dislocation motions across grains to grain boundary diffusion (Schiotz and Jacobsen 2003). A notable example is the superior properties of biologic materials that are possible because the otherwise weak and brittle components making up the materials have such small dimensions.

Natural materials derive their superior performance by incorporating small-scale particles into structures that inherently promote toughness. Lee et al. (2001) show that elongated grains enhance the fracture toughness of SiC ceramic by crack bridging and crack deflection. Yang (2007) shows that deformation mechanisms of Face-Centered-Cubic and Hexagonal-Close-Packing metals strongly depend on the grain orientations. Natural structural materials such as nacre, bone, fish scale, wood, bamboo, deer antler, and many others (Espinoza et al. 2009; Bruet et al. 2008; Fratzl 2007; Yao et al. 2010; Rhee et al. 2009; and Trim et al. 2010) illustrate the importance of spatial arrangements of individual components or grains because their extraordinary properties largely depend on their hierarchical arrangements of individual components. Natural structural materials are the best examples of how the size, shape, compositions, orientation, and spatial arrangement of individual components and the properties and characteristics of interaction between components all work together to achieve desired mechanical properties and responses of bulk materials.

SiC ceramic is a polycrystalline material with the size of grains ranging from hundreds of nanometers to microns (Cao et al. 1996). The crystalline structures of SiC include three major types: 6H(α), 4H(α), and 3C(β). The grain boundaries of SiC have thicknesses of a few nanometers and can be amorphous in structure largely depending on the sintering conditions

(Tsurekawa et al. 1995). As mentioned earlier, SiC has high compressive strength but limited tensile strength and fracture toughness because atomic bonding is covalent. The failure mechanism of SiC bulk materials can be cleavage through grains (transgranular failure) or cracks along the grain boundaries (intergranular failure). A lot of research has been performed to increase the fracture toughness or tensile strength of the SiC materials (Shinozaki et al. 1993). Cao et al. (1996) used sintering additives to achieve different fracture toughness by developing microstructures with different grain sizes and shapes. Kim et al. (1997) also used large ellipsoid-shaped grains among smaller and more equiaxial-shaped grains to improve the fracture toughness of bulk materials. LaSalvia et al. (2010) also demonstrated that the fracture toughness of the SiC bulk material was improved by weakening the grain boundaries and allowing cracks to grow intergranularly rather than transgranularly. Zhou et al. (2001) enhanced Young's modulus, hardness, flexure strength, and fracture toughness by changing the chemistry of intergranular phase in the SiC ceramic material. Fibers have been incorporated into SiC material to improve the bulk fracture toughness (Wang et al. 2006). Carbon nanotubes with their extraordinary strength and properties are also being used as reinforcement in SiC (Karandikar et al. 2008). Determination of how to take advantage of the properties of CNTs to improve the tensile strength and fracture toughness of SiC requires detailed modeling at multiple scales. Numerical simulation of SiC materials at the mesoscale can be a powerful tool for learning how to configure these materials for high-strength and high-fracture toughness.

To build detailed mesoscale models, the detailed mesostructure of materials needs to be digitally characterized and implemented in the computer models. To date, Electron Back-Scatter Diffraction (EBSD) serial sectioning is the most accurate way of characterizing samples and building digital 3-D mesostructure for computer models (Rollett et al. 2007). The mesostructure can also be built synthetically by building statistical representation of the mesostructure using data from experiments (Rollett et al. 2007). Model construction methods are critical to the success of mesoscale modeling and are described in detail in the section "High-fidelity atomistic polycrystalline models."

After mesostructured detail is implemented in the computer models, suitable modeling techniques are needed to study the mechanical properties and deformation mechanisms of the mesostructure. Researchers are

using a number of methods. The finite element (FE) method combined with cohesive elements to represent fractures is considered the traditional approach for such problems. Meshless approximations such as the peridynamics method have begun to garner greater interest because of their perceived ability to model fracture without using cohesive elements with their predefined orientations. The DEM is also being used for problems for which the grains have sufficient intergranular mobility to which continuum mechanics do not strictly apply.

The mesostructure models are not only built to study the deformation mechanisms within the mesoscale but also to generate constitutive laws to be used for macroscale models. The question thus arises, what are the smallest mesoscale models that can adequately capture the physics in mesoscale yet define a sufficiently large domain to constitute a valid representative elementary volume? Appropriate homogenization techniques have to be examined.

Structural SiC is produced by initially mixing fine (submicron) and pure SiC powder with nonoxide sintering aids. The powdered material is compacted and is then sintered under high temperature and sometimes under high pressure. The sintering of SiC can be solid phase or liquid phase (Cao et al. 1996). As mentioned previously, to achieve desired mechanical properties, the SiC mesostructure needs to be controlled. Modeling the sintering process at the mesoscale can be instrumental in guiding the selections of powders, sintering temperature, pressure, and sintering aid. However, the physics of sintering are more involved than mechanical response, as described in Chapter 5.

In the following sections in this chapter, different mesoscale modeling techniques will be discussed in detail, and some preliminary simulations of SiC will be presented. The technical gaps in this area will also be discussed.

3.1 Mesoscale modeling methods

3.1.1 Finite Element Method

Espinosa and coworkers (Zavattieri and Espinosa 2001, 2003; Espinosa and Lee 2002; Espinosa and Zavattieri 2003) performed grain-level simulations of ceramic materials under dynamic loading. The grain structure either comes from digitalization of an actual microstructure or is

generated from Voronoi tessellation. Only two-dimensional grain structures were modeled. The grains were discretized into triangular finite elements, and the grain boundaries were modeled with cohesive elements inserted between grains. The elastic and thermal anisotropic model is used to describe the single crystal anisotropic behavior stress tensor S_{ij} of the grains:

$$S_{ij} = C_{ijkl} H_{kl} \quad (1)$$

where H_{kl} is a logarithmic strain, and C_{ijkl} is the elastic anisotropic material stiffness tensor in the global coordinates. Each grain is assumed to be elastic-orthotropic, and the orientation of the principal material directions differs from grain to grain. The cohesive law used for grain boundaries is:

$$\lambda = \sqrt{\left(\frac{u_n}{\delta_n}\right)^2 + \xi^2 \left(\frac{u_t}{\delta_t}\right)^2} \quad (2)$$

where

λ = nondimensional effective displacement jump

u_n, u_t = normal and tangential displacement jumps at the interface

δ_n, δ_t = critical values at which interface failure takes place

δ_n and δ_t depend on the maximum normal traction and the fracture toughness at the interfaces.

The models predefine the cracks to grow along grain boundaries. For dynamic loading, experimental results show that cracks nucleate at triple joints and grow along grain boundaries. The assumption of intergranular failure of models is justified for dynamic loading. However, for static loading, Cao et al. (1996) and Kim, et al. (1997) show that cracks can grow transgranularly through cleavage for brittle ceramic materials. Current finite element models cannot capture transgranular crack growth.

Postek et al. (2005) also used the finite element method to model ceramic brittle materials. Their models considered the grain boundaries to be a thick layer of materials with different properties from the materials inside the grains. They considered the material inside grains to be elastic and the

grain boundaries to be elastic-plastic materials undergoing finite strain. The failure criteria for the grain boundary material were based on the equivalent plastic strain. Zhang, et al. (2005) also used the finite element method to study 3-D Voronoi polycrystal (i.e., the boundaries of the crystals are computer-generated Voronoi cells). In their model, crystal plasticity laws are applied to the grains, and cohesive elements are used to model grain boundaries.

3.1.2 Peridynamics method

Peridynamic theory (Silling and Askari 2005; Askari et al. 2008) is employed as a nonlocal meshless method that adopts a computational framework similar to MD. Unlike classic continuum mechanics, the local balance of linear momentum is expressed as:

$$\rho \ddot{u}(x,t) = \int_{H_x} f[u(X',t) - u(x,t), X' - X] dV_{x'} + b(X,t) \quad (3)$$

where

- ρ = mass density in the reference configuration
- \mathbf{u} = displacement vector field
- \mathbf{x} = position of particle X
- \mathbf{x}' = position of particle X'
- t = time
- H_x = a neighborhood volume of particle X
- $dV_{x'}$ = infinite small volume around particle X'
- \mathbf{f} = a pairwise force function whose value is the force vector (per unit volume squared) that the particle X' exerts on the particle X
- \mathbf{b} = body force density field

The pairwise force function includes the bonding laws between material points. The peridynamic method is implemented in a general molecular dynamics code LAMMPS (Parks et al. 2010). In LAMMPS, only a microelastic brittle bonding law is currently implemented. The microelastic bonding law is as follows:

$$\mathbf{f}[u(\mathbf{x}',t) - u(\mathbf{x},t), \mathbf{x}' - \mathbf{x}] = \frac{C}{\|\mathbf{x}' - \mathbf{x}\|} \left\| [u(\mathbf{x}',t) - u(\mathbf{x},t)] - (\mathbf{x}' - \mathbf{x}) \right\| \frac{(u(\mathbf{x}',t) - u(\mathbf{x},t))}{\|u(\mathbf{x}',t) - u(\mathbf{x},t)\|} \quad (4)$$

where C is the spring constant of the bond. The stretch of the bond is defined as

$$S = \frac{\|[\mathbf{u}(\mathbf{x}',t) - \mathbf{u}(\mathbf{x},t)] + (\mathbf{x}' - \mathbf{x})\|}{\|\mathbf{x}' - \mathbf{x}\|} \quad (5)$$

When the stretch of a bond reaches the critical value, the bond is considered to be broken. Damage is calculated by dividing the number of broken bonds by the total number of bonds.

Silling and Askari (2005) used the peridynamic method to study polycrystalline fracture of silicon in two dimensions. They generated Voronoi polycrystals with a grain-size distribution close to a Weibull distribution, with each grain assigned a random orientation. The microstiffness of the grains depends on the orientation of the grains and the direction of the bonds. The critical bond S_o at which a bond breaks is associated with the fracture energy and the peridynamic horizon, which is the cutoff distance of the bonds.

$$S_o = \sqrt{\frac{5G_o}{9k\delta}} \quad (6)$$

where

G_o = fracture energy of the material

k = bulk modulus

δ = horizon (the cut-off radius of material volume around particle X)

The critical bonds between grains are related to grain boundaries as follows:

$$S_o^{GB} = \beta.S_o \quad (7)$$

where β is the interface strength coefficient.

The authors attempted to use the peridynamic method to study a 6-grain SiC polycrystalline model. The LAMMPS formulation was used with a simple microelastic brittle bonding law. Initially, a 3-D 6-grain

microstructure with a bimodal distribution was generated using Mcbuilder developed by Rollett et al. (2007). Based on Silling and Askari (2005) the following equation was used to calculate the spring constant of the grains:

$$C = \frac{18k}{\pi\delta^4} \quad (8)$$

Equations 6 and 7 were used to calculate the critical bond. The bulk elastic modulus and fracture energy are from Li and Bradt (1987) and Kikuchi et al. (2005). The elastic stiffness of the bonds between the grains was determined using Equation 8. A preliminary study was performed on the effects of relative elastic stiffness and critical bond between inside grains and across the grains (grain boundaries). A uniaxial strain was applied on the specimen.

Figure 6 shows the plot of a peridynamic model of a six-grain polycrystal. Figure 7 shows the plots of the fracture path and damage when the stiffness between grains is half of that inside grains, and the critical stretch between grains is the same as that inside grains. The simulation results in Figure 8 show that cracks grow across grains, when the stiffness of the bonds between grains is twice as that inside the grains and the critical stretch between grains is the same as that inside the grains. The simulation results in Figure 9 show that cracks grow through the middle of the specimen as primarily transgranular fractures when the stiffness between grains is the same as that inside grains, and the critical stretch of the bond between grains is half of that inside grains. The simulation results in Figure 10 show that cracks develop at random locations, when the stiffness between the grains is the same as that inside the grains, and the critical stretch between grains is twice that inside the grains. Note that the grain orientations are not considered and the average size of the grains is in millimeters, which is not realistic for SiC grains. However, those models show that both elastic properties and fracture properties of grains and grain boundaries affect the fracture mechanisms of the grain structures.

3.1.3 Discrete Element Method

The discrete element method treats a material as an assembly of interacting particles that are rigid except at interparticle contacts. Steinhäuser et al. (2008) used the discrete element method to model alumina and SiC under loading at high strain rate at coarse-grain level. The particles are arranged in hexagonal packing within each grain, whereas the particles at

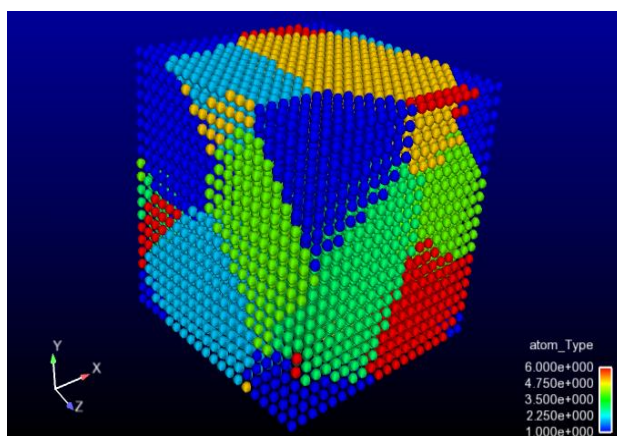
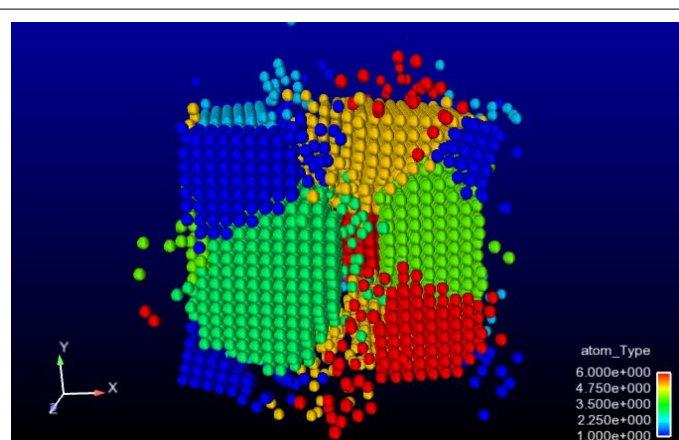
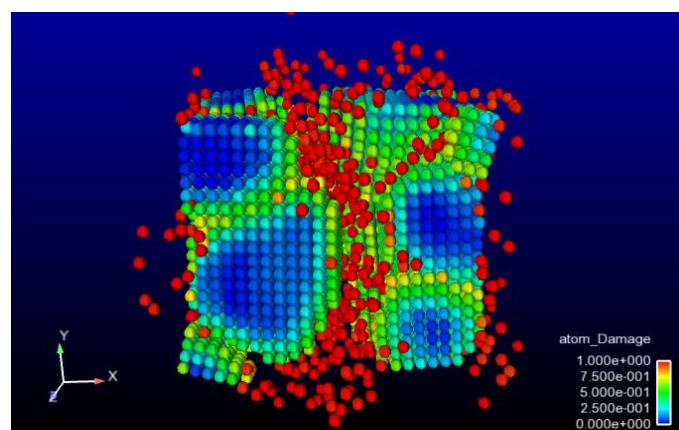


Figure 6. Peridynamic model of a six-grain polycrystal.
The colors are applied to distinguish the grains.



(a) Fracture path. The colors represent different grains.



(b) Damage. The colors denote the extent of damage. The red denotes that damage reaches one. When damage reaches one, the crack develops.

Figure 7. Peridynamic simulation results. The stiffness between grains is half that inside the grains. The critical stretch between the grains is the same as that inside the grains.

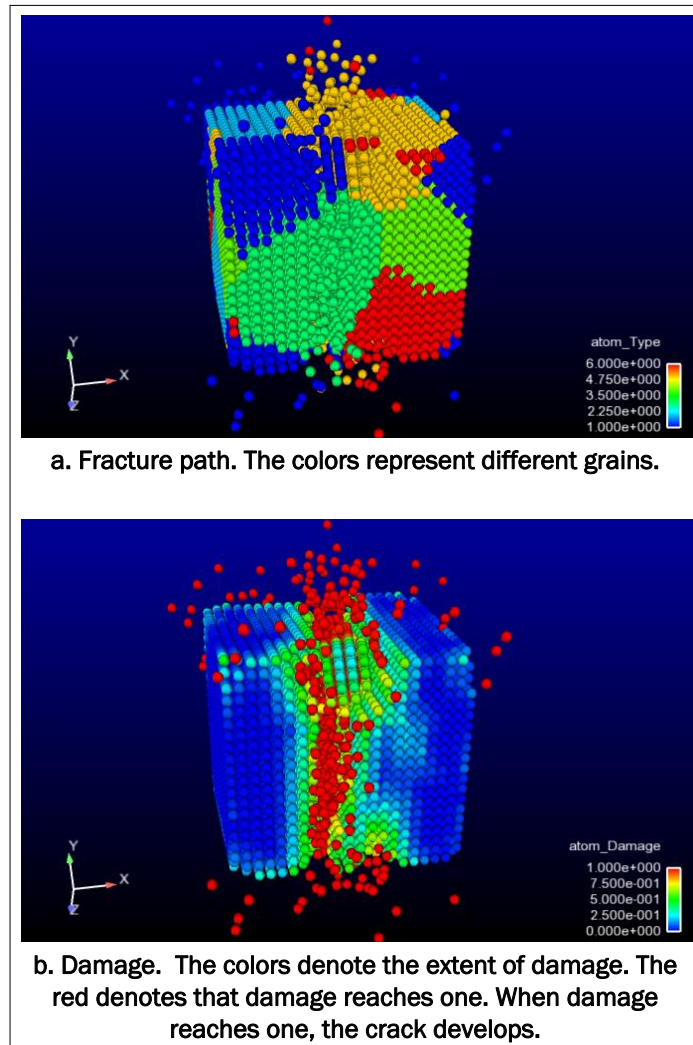


Figure 8. Peridynamic simulation results. The stiffness between grains is twice that inside the grains. The critical stretch between grains is the same as that inside the grains.

grain boundaries are packed randomly. The bonding forces between particles include contact forces and cohesive bonding force. This method is able to capture fracture at the grain boundaries and cleavage across grains.

To study whether DEM methods can capture possible plastic deformation in the grains, small-scale DEM simulations were performed to study how the packing arrangement of the particles may affect the fracture mechanisms. In this model, the specimen size is 40nm x 40nm x 160 nm. The applied interparticle forces include contact normal force, friction force, and cohesive normal bonding force. The bottom of the specimen is fixed, and a downward velocity is applied on the top. Figure 11 shows the deformation and internal stress in the vertical direction of a specimen with

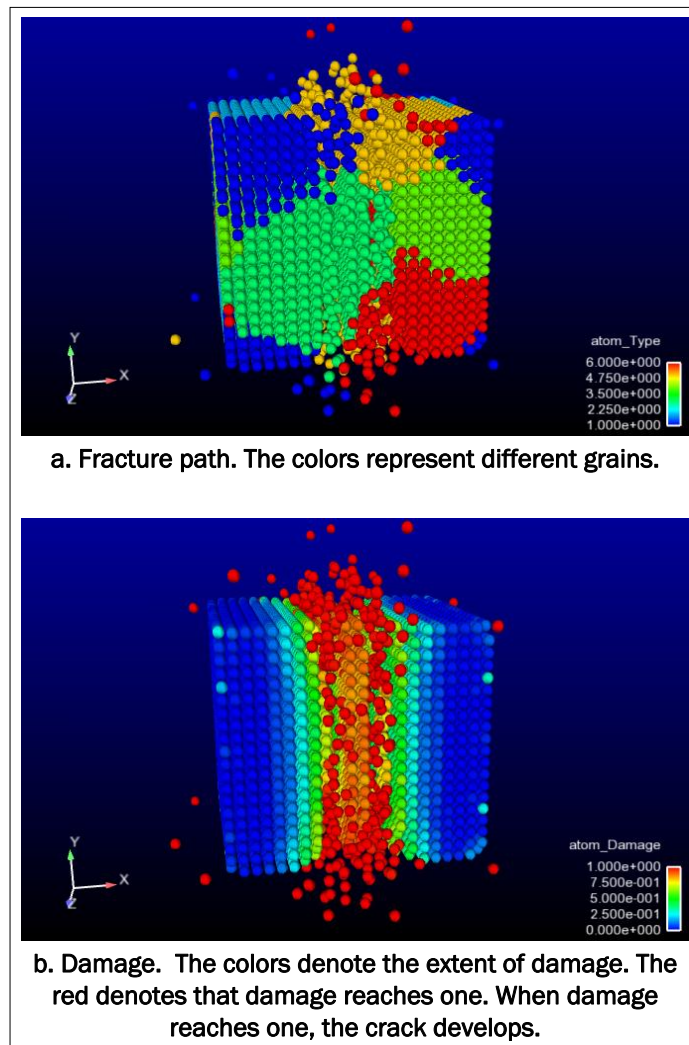


Figure 9. Peridynamic simulation results. The stiffness between grains is the same as that inside the grains. The critical stretch between grains is one-half that inside the grains.

close random packing. The color denotes the internal stress in the vertical direction. Figure 11 shows that the particles form force chains—signified by linear groups of red particles—under compressive loading. Figure 12 shows the deformation and internal stress in the vertical direction of a specimen with a face-centered close dense packing. Figure 12 shows that the specimen slips at approximately a 45-degree angle under compressive loading. However, if the cohesive force is high (twice that in Figure 12), Figure 13 shows that there are slip bands, but the specimen fails by splitting in the middle. Figures 11-13 show that packing particle in Face-Centered Cubic (FCC) packing may capture plastic deformation such as slip bands, but the interparticle force needs to be tuned to capture experimentally observed deformation mechanisms inside the grains. Note that the DEM particles are being used here as surrogates to finite elements as a

means to accommodate fracture paths which are not preselected as in the case of using cohesive elements. Arguably, such a model lacks many physical aspects of the real material, in particular an accurate depiction of wave propagation within the grains. These simulations do demonstrate that stiffness as well as strength controls qualitative features of failure.

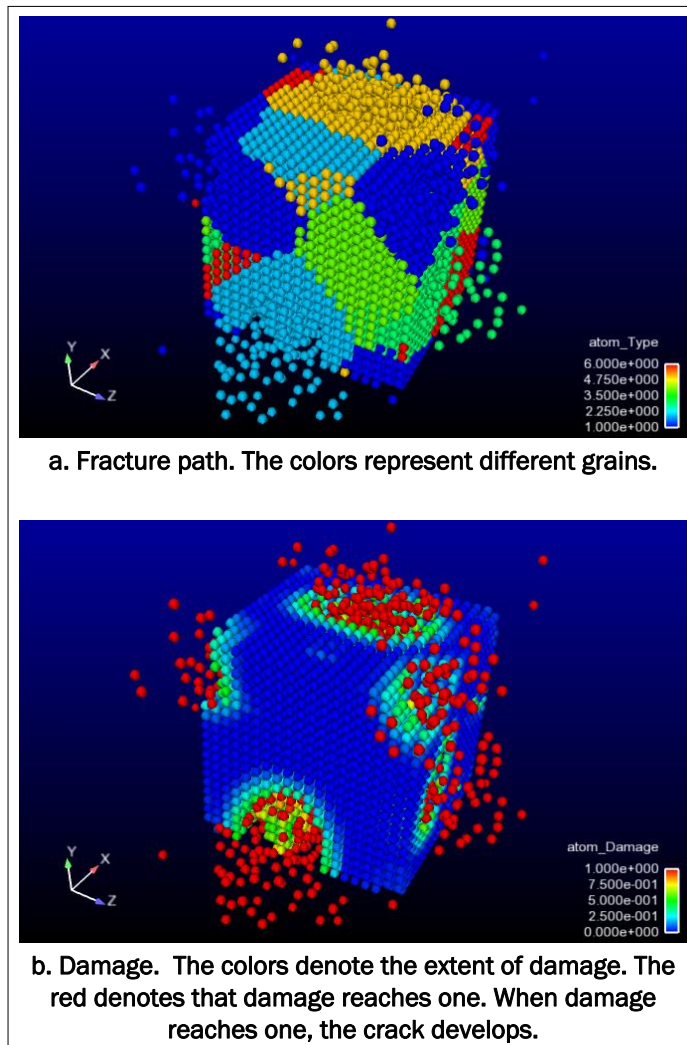


Figure 10. Peridynamic simulation results. The stiffness between the grains is the same as that inside the grains. The critical stretch between grains is twice that inside grains.

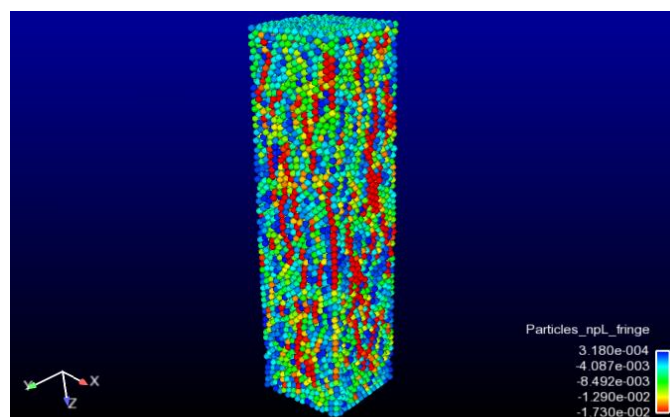
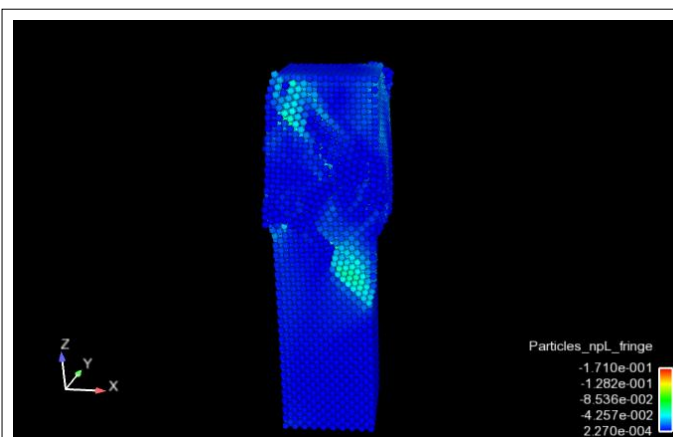
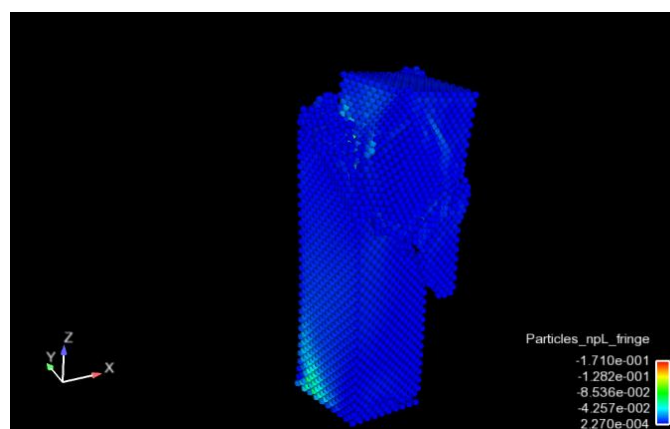


Figure 11. Deformation and internal stress in the vertical direction of a specimen with close random packing. The color denotes the continuum stress at the vertical direction. Red denotes the highest stress.



a. The slip just initiated.



b. The slip progressed until complete failure. The color denotes the continuum stress at the vertical direction. Red denotes the highest stress.

Figure 12. The specimen has close, dense packing, and cohesive bonding force is small.

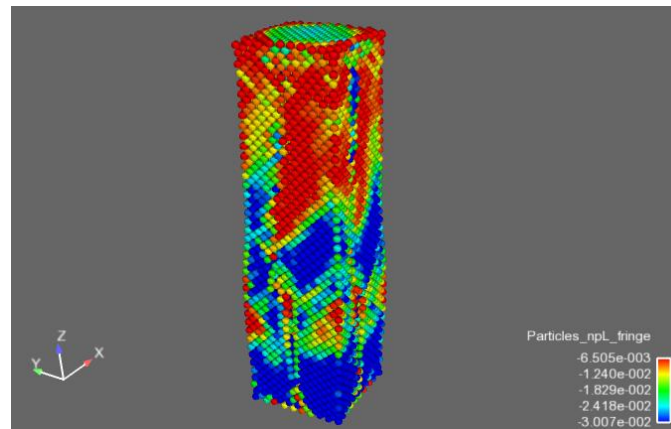


Figure 13. All the parameters are the same as for the specimen shown in Figure 12 except that the cohesive stress is twice that applied in the specimen shown in Figure 12. The color denotes the continuum stress at the vertical direction. Red denotes the highest stress.

3.2 Technical gaps in mesoscale modeling

Based on the information provided in the previous sections, the following shortcomings were found for all the methods described:

- The finite element method is the best established for modeling polycrystalline material at the mesoscale. This method can address possible plastic deformation inside the grains. However, it can address the intergranular cracking only where the orientation of the potential fracture is known. Although cohesive elements can be placed between boundaries of the elements, doing so makes the discretization, which should be arbitrary, a property that controls fracture toughness. Prediction of general fractures within a solid medium is still beyond the capabilities of continuum theories.
- Methods based on peridynamics can address failure inside the grains and at the grain boundaries. However, it does not address possible plastic deformations inside the grains. Moreover, many details about the actual physical mechanisms captured by the peridynamic formulation have yet to be resolved.
- The DEM may be used to address both intergranular and transgranular cracking, and it may even address plastic deformations. As noted previously, the method is not fundamental for modeling continuum media, although it could be argued that the method is no less suited for this application than peridynamics. In any case, for the method to give realistic quantitative results, suitable particle packing for the grains

and grain boundaries and appropriate interparticle forces between particles need to be developed.

3.3 High-fidelity 3-D digital microstructure models

Realistic microstructure and nanostructure models for finite element, mesoscale, or atomistic simulations of the sintering process are difficult to produce without special-purpose preprocessing software. Professor Anthony Rollett at Carnegie Mellon University, Pittsburgh, PA, has developed a method for constructing high-fidelity 3-D digital material models. ERDC initiated a project, “High-fidelity 3-D digital polycrystalline microstructure models,” to produce the models needed for the submicron-scale simulations of the sintering process of SiC. The project will produce models that allow the evolution of material structure during processing to be studied at resolutions ranging from atomistic to microscale. The project is supported through the PETTT program. The principal investigators on the project are Anthony Rollett and James Larentzos, High Performance Technologies, Inc. (HPTi). This project will develop the technology needed to produce accurate 3-D digital microstructure models needed to assist experimental efforts to design and test novel high-strength materials. Polycrystalline materials such as ceramics, concrete, and some biomaterials include grains, particles, flaws, and reinforcements with different morphologies. The new tools will be used to build accurate digital microstructures with grains with large aspect ratios, flaws, and fiber reinforcement and will be based on Carnegie Mellon’s Microstructure Builder (MBuilder) tool. The digital microstructure will be validated against the microstructure data collected via experimental techniques. The digital microstructures will then be incorporated into atomistic, peridynamics, finite element numerical models to study the response of materials at the multiple scales. The project will focus on the generation of digital macrostructures with flaws, grains with large aspect ratios, irregularities, and fiber reinforcements such as carbon nanotubes and carbon nanotube-based fibers.

Any attempt to simulate the structural evolution of materials accurately during processing must begin with a faithful digital representation of the initial state of the material. However, capturing the initial state of the complex structural geometry of a material remains problematic. For modeling and simulation to be viable tools for studying the behavior and performance of materials, research scientists must provide a solid link between the experimental material under study and the abstract digital representation of the material used in the simulations. The experimental

characterization of the material provides this link. The material building process employs a combination of experimental and computational techniques to capture the complex structure of the material. This technique then creates a statistically equivalent representative 3-D digital model for input into computer simulations. It takes geometric and crystallographic observations from two orthogonal sections of a polycrystalline material (Figure 14). The experimental data collected from the two observation planes of the sample material are used to construct experimental distribution functions. The distribution functions created during the scanning process are used to guide the construction of the 3-D digital structure (Figure 15). In the end, the characterization criteria provide a quantitative measure for gauging the accuracy and quality of the abstract model. Furthermore, the method can be used to generate a wide variety of hypothetical material states systematically for 3-D digital structures for computer simulation. These hypothetical models provided a practical means of conducting virtual experiments to examine material synthesis under a wide variety of experimental conditions. These models will have the predictive capability necessary to model the evolution of the material structure during processing.

3.4 Methods for validating the digital models

Three critical elements of this technology are the following:

- An accurate 3-D digital representation of the microstructure of the material
- An efficient method for generating the finite element mesh needed for modeling and simulations
- A software package that automates the process as much as possible.

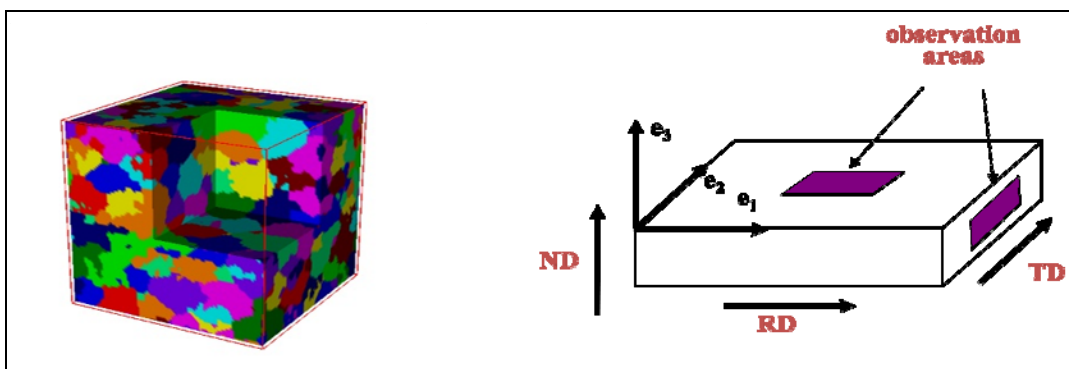


Figure 14. The material is scanned using an automated EBSD in a Scanning Electron Microscope (SEM), also known as Orientation Imaging Microscopy (OIM) to examine two surfaces of the material.

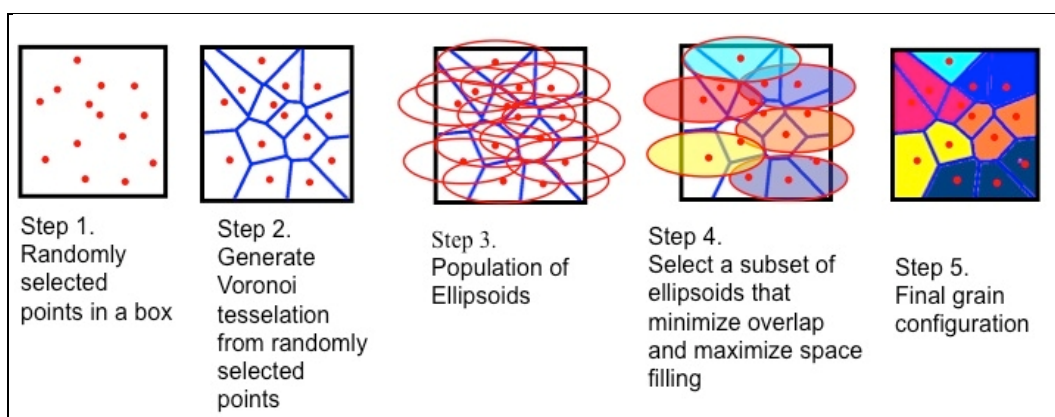


Figure 15. Generation of geometric grain configuration by assigning Voronoi tessellations to ellipsoids.

The first step in the process is to collect the data from the two orthogonal observation planes of a polycrystalline material. The MBuilder uses automated EBSD in a Scanning Electron Microscope (SEM), also known as Orientation Imaging Microscopy (OIM), to examine two surfaces of the material. The experimental distribution functions are obtained from the data collected from the orthogonal section planes for each of the measured parameters. At present, distribution functions are generated for the size, shape, and orientation of the grains and the crystallographic orientations and misorientations across grain boundaries for each grain in the observation planes. Here, it is assumed that the region covered by the observation planes is adequate to serve as a representative volume element of the material and that the experimental distribution functions obtained from this data can adequately characterize any anisotropy associated with the experimental data. To simulate the microstructure geometry, ellipsoids (grains) were generated according to the experimental distribution function. Ellipsoids were chosen to represent grain geometries because they are simple geometric forms that describe both the size and aspect ratio of the different grains that compose a polycrystalline microstructure. Grain geometries were then constructed based on the packed ellipsoids using a continuous nucleation and growth model to fill space (Rollett et al. 2004).

Once the geometric 3-D description of a polycrystalline microstructure is complete, the crystallographic information is assigned to each grain forming the abstract microstructure such that the distribution of grain orientations is equivalent to the measured distribution in the real polycrystalline material. The distribution in the misorientations across grain boundaries is reproduced using a Monte Carlo simulation technique.

The Monte Carlo simulation uses the root-mean-squared difference between the distribution functions in the real and simulation materials for the acceptance criteria in the Monte Carlo simulation. Changing or swapping the orientations of the grains generates trial crystallographic orientations. The difference in the distribution functions is recalculated. If the trial configuration results in a lower difference function, the trial configuration is accepted. If the difference function is greater for the trial configuration but the difference is small enough, it is probabilistically accepted. Otherwise, it is rejected. This process continues until some convergence criteria (input parameter) are met at which point the process stops. The crystallographic orientations of the real material and abstract model are considered statistically equivalent to the extent that the differences in the distribution functions have been minimized. Once the grains are produced, a finite element mesh is generated for each of the grains (Figure 16) (Cornwell and Noack, 2005).

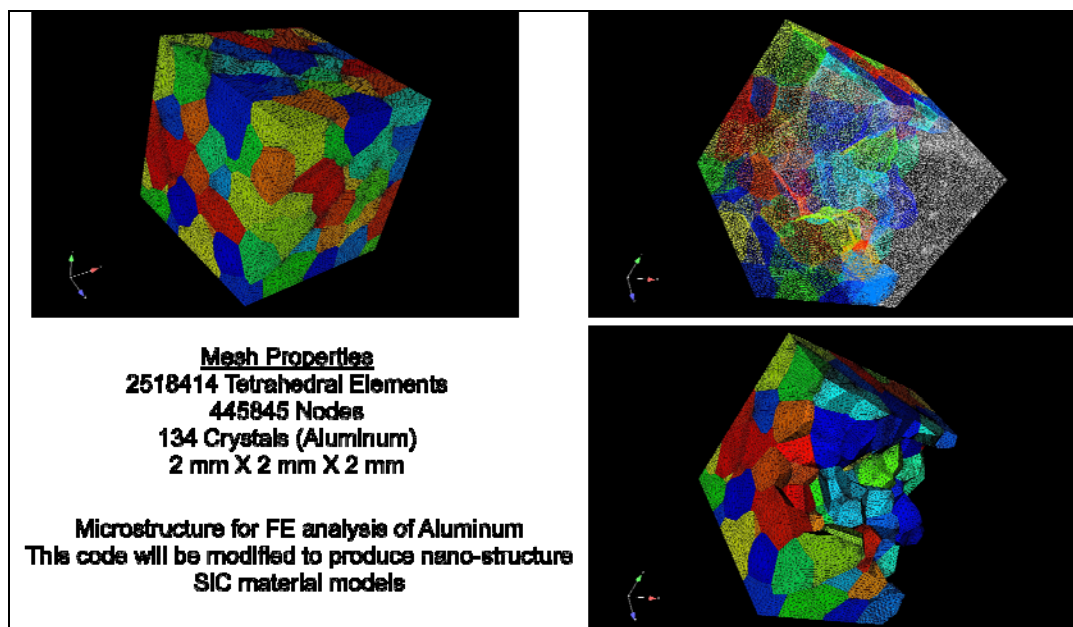


Figure 16. Finite element mesh generated from a sample of aluminum (the model consists of 134 randomly colored grains). The technique can be used to produce microstructure models for finite element simulations and nanostructure models of SiC for atomistic simulations.

3.5 High-fidelity atomistic polycrystalline models

The MBuilder project will capture the structure of the materials and provide a way to validate the structure of the models against experimental data. The atomistic simulations will require a way to populate the structure with atoms having correct crystal structure and orientations.

This information is also provided by the experimental data. Software is being developed that will:

- Generate atomic crystal grains
- Control crystallographic orientation for each grain
- Produce correct mismatch distribution at grain boundary
- Provide a method for controlling the size and composition of grain boundaries
- Construct boundary conditions for simulation
- Insert CNTs and CNT fibers into the SiC matrix.

This work is being done in parallel with the MBuilder project. The software package QHULL is used to produce the grain structure needed to develop the atomistic models of the material structures. Initially, simple grain structures are used to develop the code for the atomic crystal structures. This technique can be applied to any closed volume and will work equally well with the data that are provided by the MBuilder project. Figures 17 and 18 show examples of systems with two grains and a grain boundary with different orientations. The crystallographic orientation of each grain is the same, but the software will be extended to change the crystallographic orientation of the grains to produce a crystallographic orientation mismatch between adjacent grains.

Figure 19 is a system with nine grains: eight grains on the corners and one diamond-shaped grain located at the center.

These simple models can be used to capture the effect of particle size on grain growth during sintering. They can also model the interaction at the grain boundaries and the effect of grain size and composition on grain growth. Some evidence in the literature suggests that MD simulations are able to capture aspects of particle-particle interactions that are not possible in the current versions of mesoscale and continuum models. It may be possible to improve the coarser grained models based on information obtained from the MD simulations. On the other hand, there always may be information about the sintering process that is obtainable only through atomistic simulations.

CNTs and CNT fibers have not begun to be inserted into the SiC matrix yet. The software for constructing the CNTs and the CNT fibers is available from a previous project designed to study the design of CNT fibers and

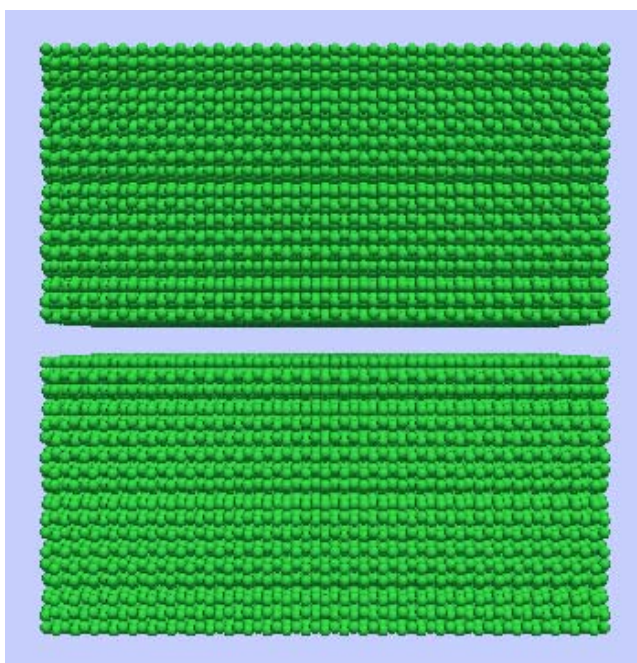


Figure 17. SiC system with two grains. Grain boundary is 1 nm wide and aligned perpendicular to the z-axis. The system dimensions are 10 x 10 x 10 nm. Both grains have the same crystallographic orientation.

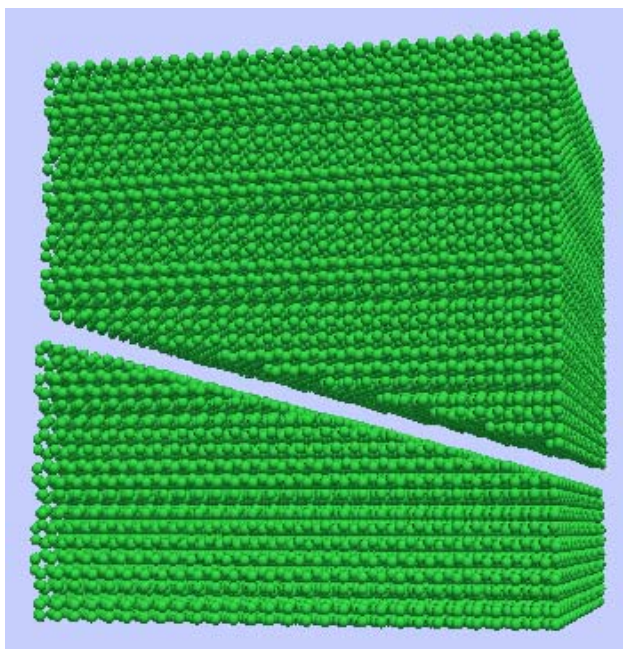


Figure 18. SiC system with two grains. Grain boundary is 1 nm wide and the x-axis is rotated 15 deg out of the xy-plane. The system dimensions are 10 x 10 x 10 nm. Both grains have the same crystallographic orientation.

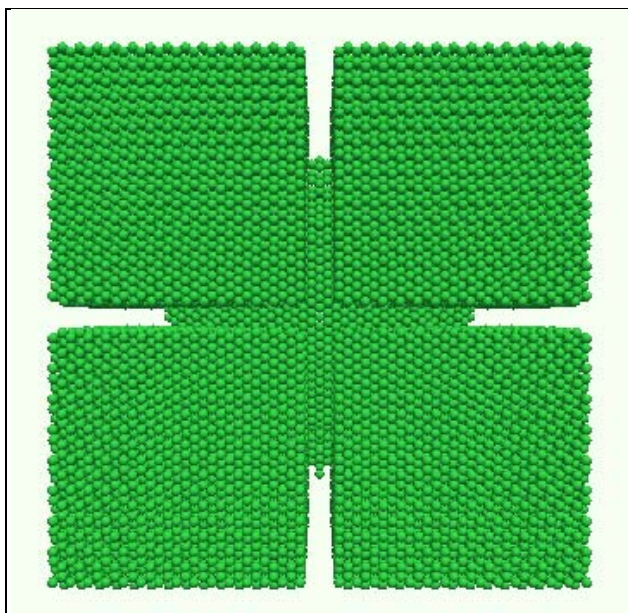


Figure 19. SiC system with nine grains: eight grains on the corners and one diamond-shaped grain located at the center. Grain boundaries are 1 nm wide. The system dimensions are 10 x 10 x 10 nm. All of the grains have the same crystallographic orientation.

membranes. This work will be completed in FY11. Also, the models are constructed using a single crystal structure of SiC. The modular form of the software will allow other crystal structures to be added on an as-needed basis. Once the MBulider project provides the structure for the materials, simulations can begin on 3-D digital material models constructed from experimental data. At this point, the experimental data will begin to be used to validate the simulation results with the results from experiments. The results from atomistic and mesoscale simulations will be able to be validated with experiment.

4 Material Synthesis

The initial nanoscale studies of the synthesis of ceramic (polycrystalline) materials involved a number of tasks. A critical task was to identify the most promising sintering methods. Attendant to those tasks was the acquisition of initial ceramic synthesis equipment. In addition, ceramic synthesis experiments were required to establish baseline methods. These experiments involved SiC and geopolymers with iterations and refinements of the simulation-synthesis experimental cycle.

SiC is a well-studied class of materials consisting of a silicon and carbon crystal structure with over 250 polytypes. Since SiC is not abundant in nature, it is usually grown in one of several ways. Single crystals of low quality can be made using the Acheson Process. This is a commercial process that involves high temperatures and long processing times. Bulk single crystals of high quality can be produced using the Lely Method and the Modified Lely Method. Dense polycrystalline ceramics are formed by compacting and sintering small SiC grains (powder sintering).

4.1 Polycrystalline ceramics

Much processing is done to form the desired starting material for sintering. The smaller the starting powder, the more likely it is to sinter. The powder is compacted and then heated (sometimes while under pressure) to form a dense body. The dense body comes about through the diffusion of matter between adjacent particles to form what are called grains. The driving principle behind the sintering process is the tendency to minimize surface energy by minimizing surface area and maximizing radius of curvature. Between the grains are pores. To eliminate the pores, the grains are allowed to grow. However, larger grains have less desirable mechanical properties. To minimize grain growth, pressure can be used while sintering to cause the grains to rearrange themselves, thereby eliminating the pores without enlarging the grains. Another method used to limit grain growth is to increase the heating rate while sintering. This allows the diffusion to occur before grain growth takes place. Pressure in addition to high heating rates is beneficial for reducing void and particle sizes.

4.2 Sintering methods

Many methods of sintering SiC have been identified, although the common feature of all is an SiC powder “compact” that is heated in a resistance furnace. Densification occurs in several stages. First, the particles join at their contact points via diffusion driven by a minimization in surface energy. Continued diffusion produces a 3-D network of solid matter as well as a 3-D network of open space (pores). Grain growth causes the porosity to decrease until the pores become isolated and sometimes coalesce. Densification stops, but the grains may continue to grow, sometimes engulfing the pores.

Several factors influence the ability of SiC to sinter. Sintering is a competition between minimizing surface energy of the particles and the grain boundaries. Smaller particles will have a higher incentive to sinter. However, the decrease in surface energy is countered by an increase in energy of the grain boundaries. Another factor that affects the final sintered density is the green density (i.e., the density of the powder before final sintering). Usually, the higher the green density, the higher will be the sintered density.

Either solid-state methods or liquid-state methods can achieve sintering. Liquid-state sintering is similar to solid-state sintering except for the addition of sintering additives to the SiC powder. Typically, these are metal oxides (yttria, alumina, magnesia). These additives form a eutectic composition and melt at the sintering temperature forming a liquid phase between the SiC grains. This liquid effectively reduces the friction between the SiC particles, allowing them to move around and settle, and increases the rate of diffusion. This procedure is typically done in conjunction with pressureless sintering, hot pressing, or sintering forging. The only equipment needed is that for solid-state sintering. The advantages of liquid-state sintering are lower sintering temperatures, higher density, and less grain growth. Nevertheless, since the liquid phase is located in the grain boundary, the strength of this phase is a limiting factor to the strength of the polycrystalline composite. In addition, the working temperature range cannot exceed that of the liquid phase.

In hot pressing, heat and pressure are applied to a sample (up to 2000 °C and 50 MPa) and can be done in a vacuum. Hot pressing is less effective for fine powder samples that are already well compacted because the compaction process has already reduced the void space. Special hot press

equipment is required for the method. Hot pressing results in good microstructure, high density, moderate grain growth, but again is a time-consuming process.

Similar to hot pressing, sinter forging samples are not confined laterally. High strains effectively push out voids. Although a hot press is used, in contrast to hot pressing, the sample in sinter forging must be smaller than the die. The result is higher density and minimal grain growth, although the process usually results in an aligned grain structure because of high strains.

In hot isostatic pressing, inert gas pressures up to 30,000 psi and temperatures up to 2000 °C surround the SiC compact. A hot isostatic Press (HIP) unit is required for isostatic pressing. The benefit to this time-consuming and complicated process is uniform pressure leading to uniform microstructure.

Microwave sintering is achieved through interaction between microwaves and atoms forming the material, causing rapid heating (reported up to 1000 °C/min). Through a combination of frequencies from 2.5 to 85 GHz, densification is enhanced, although the mechanisms involved are unclear. Microwave sintering can be used in conjunction with pressure. A microwave furnace is needed. The process produces a higher density than traditional methods. High heating rates mean shorter sintering times.

Plasma Assisted Sintering is a variant of microwave sintering in which the sample is surrounded by plasma that is ignited by the microwaves. The plasma promotes enhanced densification, although it is unknown whether the cause is the plasma or the high temperature inside the plasma.

Spark plasma sintering (SPS) involves passing an electrical current pulse through the sample while under pressure (30-50 MPa). Spark discharges in the voids between the particles are assumed to cause high heating rates (reported up to 600 °C/min) leading to high densification rates. This method is useful for nano-sized particles. This method is used because of its fast sintering times, minimal grain growth, and high density. The SPS sintering method using an arc discharge between adjacent particles requires very special equipment. Several companies make these systems including FCT in Germany (<http://www.fct-systeme.de/en/start/Home.html>) and SPS Syntax in Japan (<http://www.scm-sps.com/>).

4.3 SiC synthesis experiments

SiC polycrystalline samples have been made using commercially bought SiC powder and sintering additives. The powders were milled to fine sizes, mixed with additives, and heated to high temperatures. By the end of 2010, these steps were being optimized to form a dense polycrystalline ceramic.

The as-received powders were characterized for particle size and density. After planetary milling for various durations, the particle size was again determined. Representative data are shown in Figure 20.

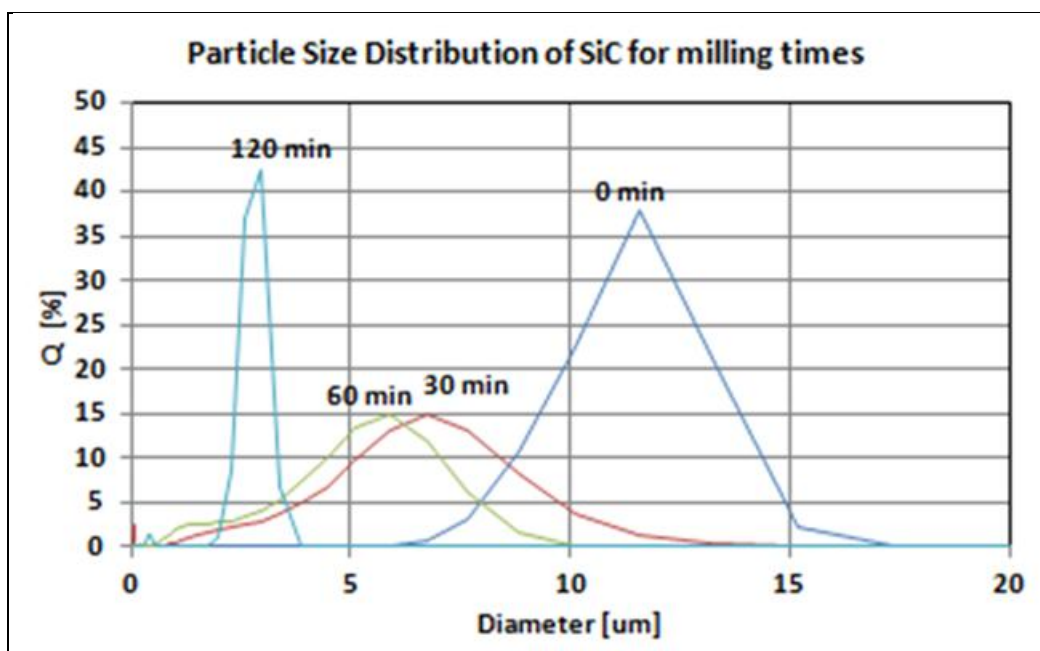


Figure 20. Particle size for various milling times.

The powders were then placed into a forming mold and pressed into small disks, which were subsequently isostatically cold-pressed to approximately 45,000 psi. The samples were then placed in graphite crucibles in a vacuum furnace at 2000 °C for 1 hour. These steps are shown in Figure 21.

4.4 Product characterization

The surface and interior surface were characterized by SEM images. The samples shown in Figure 22 are not fully sintered. They do not have significant density, but do show the start of grain diffusion. Mechanical testing has yet to be completed for any samples.

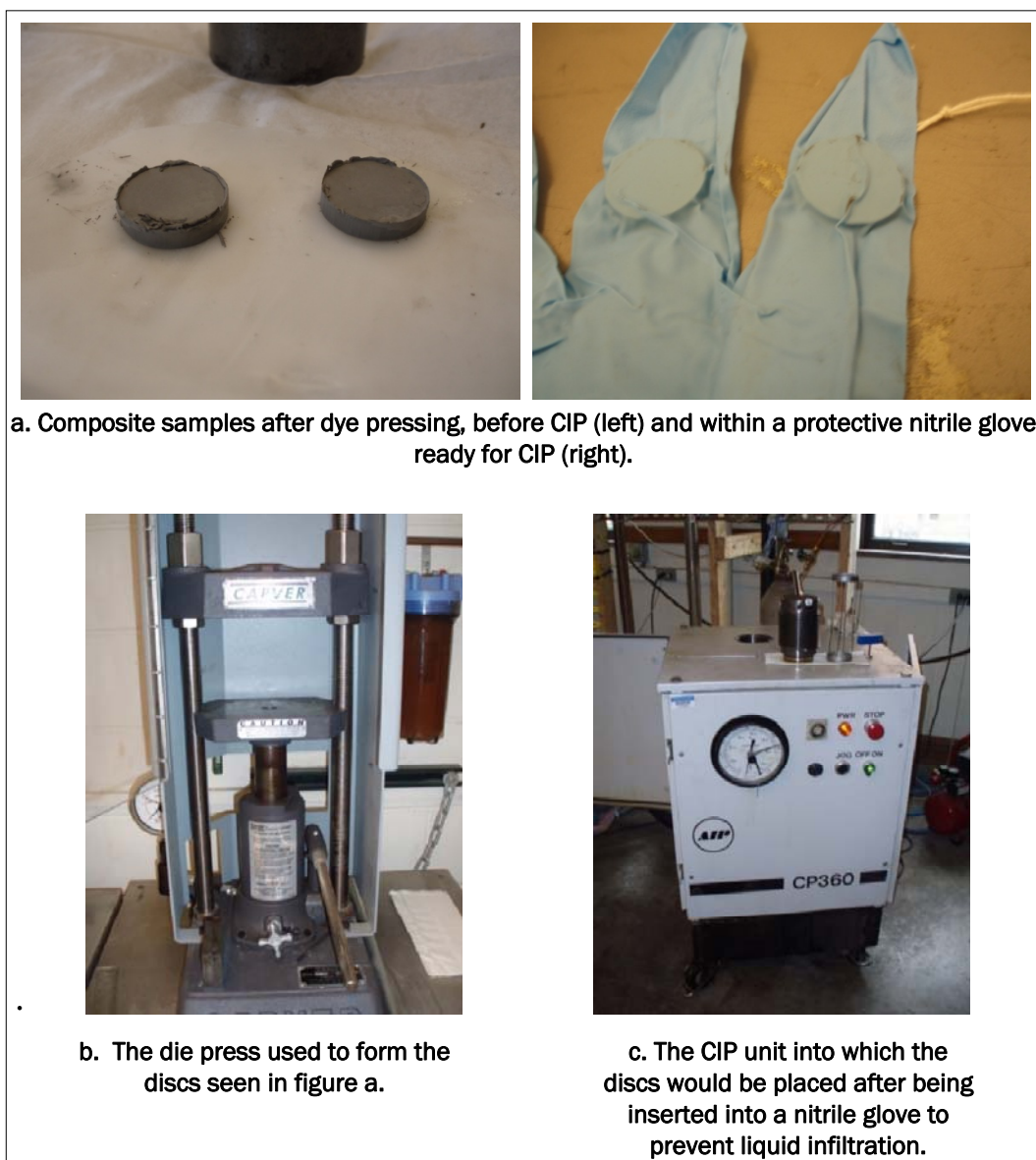


Figure 21. a-b) SiC disks before CIP. c) Press used to form disks. d) CIP unit.

4.5 FY11 tasks

The tasks of acquiring use of ceramic synthesis equipment, ceramic synthesis experiments, and making refinements to the simulation-synthesis experimental cycle will continue. The authors hope to have access to an SPS unit for high-rate sintering.

Synthesis methods will continue to be explored, particularly attempting to understand what occurs at each of the many processing steps. Powder synthesis methods including ball milling and mechanical-chemical grinding will be studied. Powder characterization including particle size, agglomeration, density, crystal structure, and surface chemistry will be

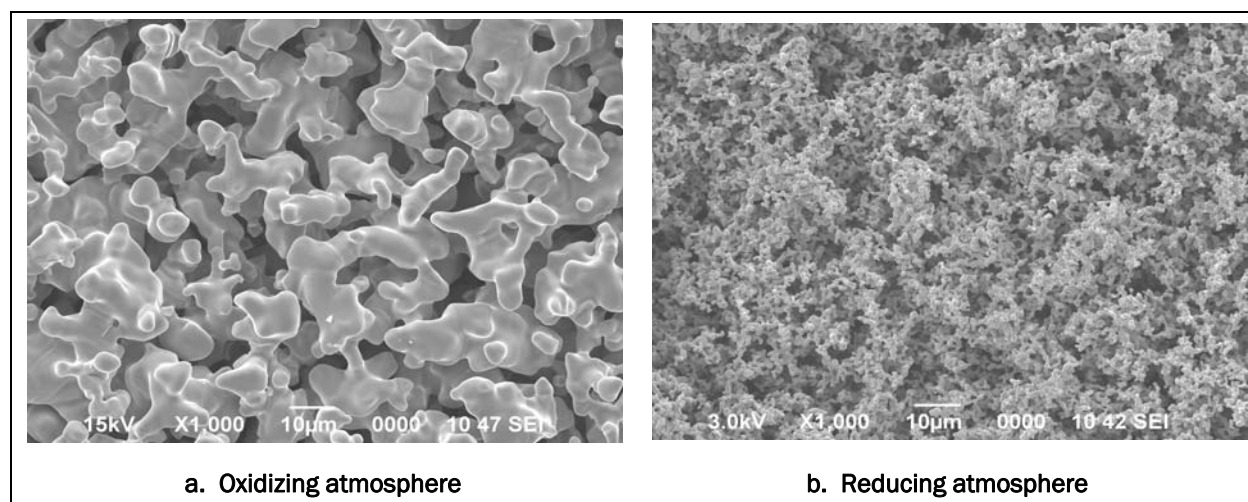


Figure 22. Samples after sintering step.

investigated. Experiments for mixing, packing, and forming of powders will be performed. The sintering techniques chosen will be employed; and the influences of particle size, particle geometry, grain growth, coarsening, pore mobility, green body density, and heating schedules on the resulting microstructure will be documented.

Using the knowledge gained on the methods of polycrystalline ceramic synthesis, SiC samples will continue be made and refined. The objective is to make a polycrystalline material that has as close to 100 percent density as possible and contains the smallest grains possible. This work necessarily includes two components: synthesis and characterization. Both components are straightforward, but take considerable time. Processing, forming, and sintering (the three steps in the synthesis part) are time consuming and require attention to detail. The characterization component includes activities such as scanning electron and transmission electron microscopy, atomic force microscopy, x-ray diffraction, density measurements, and mechanical testing. Each of these activities is also time consuming and will need to be repeated for each sample made.

The simulation-synthesis experiment cycle will begin for each sample by determining the microstructure and mechanical properties, which will be sent to the modeling and simulation teams, who will model the microstructure for simulation of mechanical tests. This procedure will allow verification that the algorithms used are correct. Once verified, the modeling and synthesis teams can begin to work together on the improvement of specific properties based on changes in modeled microstructure.

Once an appropriately dense SiC sample is made, silica-functionalized carbon nanotubes will be added to the initial powders. A description of work being done to functionalize CNTs with silica is given later in this technical report. The method for synthesizing polycrystalline ceramics has been chosen to be powder sintering. The sintering methods chosen are liquid phase sintering, hot pressing, and SPS.

4.6 Technical gaps

Fundamental research needs to be conducted to determine why SPS works. So far all that is known is that it works very well (i.e., produces dense ceramics), but no one has a definitive answer as to what occurs during the sintering process. The authors would be able to guide their multiscale modeling more accurately if they knew the answer to this question, particularly the physical synthesis. In addition, knowing what happens during the SPS process will allow better prediction of what might happen to CNTs dispersed in the matrix, how to protect them from degradation, how to allow for better bonding, and how to make full use of their strength. Ceramic synthesis and sintering have been around for quite some time, but the new method of SPS has brought about the capability to make dense ceramics with small grain size. How these small grain sizes interact with carbon allotropes is one question that needs to be investigated during this project.

4.7 Carbon nanotube functionalization

A review of literature covering the functionalization of CNT with silica affords several different methods, each with their own drawbacks. Li et al. (2009) claim that their process does not damage CNT and is economical and environmentally friendly. Their procedure relies on the Stober method for producing nanoscale silica, wherein an ammonia-activated cocondensation reaction occurs between ethanol, hydroxyl functional groups on CNTs, and tetraethyl orthosilicate. When complete, the CNTs are functionalized with a silica layer 2 to 10 nm in thickness with varying uniformity (Figure 23). The thickness and uniformity may be controlled by various reaction parameters.

First, multi-walled CNTs or single-walled CNTs are functionalized with hydroxyl groups 50 - 250 mg at a time using a Harrick Plasma Cleaner (Figure 24). The instrument provides an inductively coupled air plasma at about 150 mtorr and is cycled three times for 20 seconds each cycle. These

CNTs are then ultrasonically dispersed in 100 - 250 mL of ethanol using a Cole-Parmer CPX130PB. In this research, sonication imparts a total of 1.5 kJ of ultrasonic energy to the suspension by applying 30 percent power for 5 min using a 1/4 inch probe. Following the sonication process, 4 – 20 mL of 28 percent NH_3 and 1 - 4 mL of tetraethyl orthosilicate are added to the mixture, which is then covered, stirred, and heated at 65 °C for 0.5 - 4 hours. The mixture is then immediately filtered over a membrane. To obtain a suspension of the silica-functionalized CNT in water, the functionalized product may be added to water and sonicated.

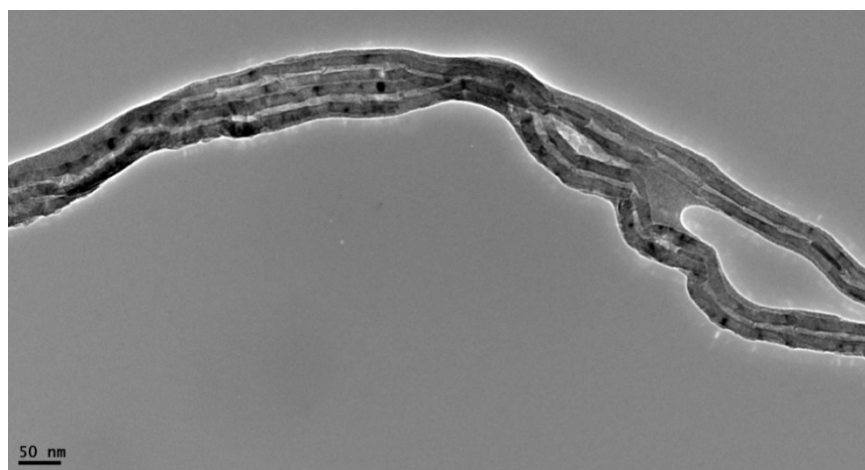


Figure 23. Silica functionalized CNTs made at ERDC –CERL.



Figure 24. Harrick plasma cleaner used to functionalize CNTs.

5 Modeling the Sintering Process

Sintering is a process by which powdered SiC is coalesced into a solid polycrystalline mass through heating and sometimes using pressure. The grain size distribution of the polycrystalline material differs from that of the original powder depending on the particular sintering process and values of the control parameters (see Chapter 4). In modeling the sintering process, two questions arise: What are the physical conditions required to achieve the specified material properties, and can those conditions be achieved uniformly throughout the body? The first question requires consideration of atomic-scale and mesoscale processes. The second involves modeling the energy transfer within the mass using continuum models.

5.1 Particle-scale view of sintering

SiC structural materials are formed by either solid- or liquid-state sintering (Niu et al. 2011 and Biswas 2009). Solid-phase sintering includes two stages: necks form at the contact points between particles, then the grain boundary diffusion causes shrinkage, and the material is densified. Liquid-phase sintering is the process of including an additive in the powder that will melt before the matrix phase. The process of liquid phase sintering has three stages: rearrangement, solution-precipitation, and final densification. Mesoscale models have been developed to study the evolution of microstructure during both solid sintering (Braginsky et al. 2005) and liquid sintering (Lee et al. 2007).

5.1.1 Mesoscale modeling of solid-state sintering

Braginsky et al. (2005) used a kinetic Monte Carlo (KMC) model to simulate two-dimensional microstructure evolution during solid-state sintering. The model can capture grain growth by short-range diffusion from one side of a grain boundary to the other, and it can also model long-range diffusion of pores by surface diffusion and vacancy annihilation at grain boundaries.

In the model by Braginsky et al. (2005), grains, pores and vacancies are represented by an assemblage of points. Each point is assigned a state corresponding to a unique integer value, $q_{\text{grain}} = [1, 2, \dots, Q]$, that

corresponds to Q different crystallographic orientations. Each pore site is assigned only one state $q_{pore} = -1$. Each grain consists of contiguous sites with the same orientation (i.e., same integer value). Grain boundaries are therefore represented as the surfaces between sites of different grains, and grain surfaces are the boundary between grain sites and pore sites. A vacancy is defined in this model as a single pore site that is entirely surrounded by grains.

The primary driving force for this model may be expressed as the reduction in interfacial free energy. The equation of state is thus the summation of interaction energy of the system, defined as

$$E = \sum_{i=1}^N \sum_{j=1}^n J_{ij} [1 - \delta(q_i, q_j)] \quad (8)$$

where

N = total number of points

n = number of adjacent neighbor points

J_{ij} = neighbor interaction energy between sites i and j

q_i = state of the grain or pore at site i

q_j = state of the nearest neighbor at site j

$\delta(q_i, q_j)$ = Kronecker delta with $\delta(q_i = q_j) = 1$ and $\delta(q_i \neq q_j) = 0$

The standard metropolis algorithm is then used to perform the grain growth step with probability P given by

$$P = \begin{cases} \exp\left(\frac{-\Delta E}{k_B T}\right) & \text{for } \Delta E > 0 \\ 1 & \text{for } \Delta E \leq 0 \end{cases} \quad (9)$$

where

E = total energy using Equations 8 and 9

K_B = Boltzmann constant

T = temperature

Figure 25 provides an example utilizing an in-house-developed 2D KMC model involving the microstructural evolution of a sintered powder compact over a total duration of 1 million Monte Carlo steps (MCS). The time in a KMC model is measured in MCS, such that 1 MCS corresponds to

N attempted grain growth steps. As indicated, the initial microstructure shows a large numbers of fine grains and pores. As the simulation continues, the number of pores decreases and the grain sizes are several times larger than those at the initial stages of sintering.

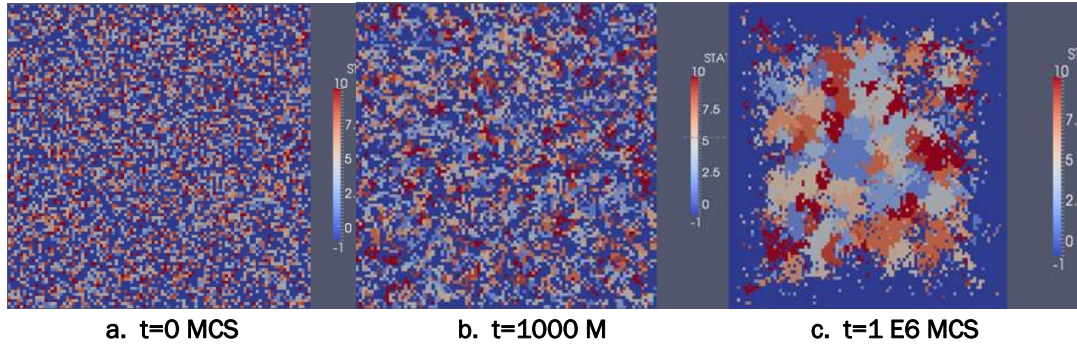


Figure 25. Microstructure evolution of a random packing nonuniform powder.

5.1.2 Mesoscale modeling of liquid phase sintering

Lee et al. (2007) performed three-dimensional simulations of isotropic coarsening in liquid phase sintering. In liquid phase sintering, particle coarsening occurs by mass transport through the liquid surrounding solid particle. The driving force is determined by the solubility of particles (Lee et al. 2007):

$$\ln \left(\frac{S_r}{S_\infty} \right) = \frac{2M\gamma}{R_g T \rho r} \quad (10)$$

where

- S_∞ = solubility of a solid particle with an infinite radius
- M = molecular weight of the solid with density ρ
- γ = interfacial free energy between the solid and liquid phases
(assumed to be isotropic)
- R_g = gas constant
- ρ = density of solid
- r = radius of solid particle
- T = absolute temperature

Monte Carlo simulations also are used to model the grain growth in the liquid-phase sintering. Similar to the model used for solid-phase sintering, an assembly of voxels populates the solid phase and liquid phase. Each

solid voxel is assigned a spin number based on the local particle orientation, and each liquid voxel is assigned a spin number of -1. The kinetic Monte Carlo simulations are performed to minimize the interface energy.

5.1.3 Technical gaps

Both solid-phase sintering and liquid-phase sintering are complex processes. Many factors such as temperature, pressure, and sintering additives affect the development of microstructure (Maizza et al. 2007; Dillon and Harmer 2008; Pan and Gong 2010). Current mesoscale sintering models typically address only grain growth, pore migration, and vacancy annihilation at grain boundaries by minimizing the total surface energy. This will often include grain boundary mobility effects, which take into account the curvature-driven grain growth of boundaries toward their centers of curvature. The effects of temperature, pressure, and additives are not included in the current models. The size, shape, and distribution of initial powders also affect the microstructure development. The powders are usually compacted into green bodies before the high temperature is applied. The current models usually use spherical particles with random radius and packing to represent powders, and do not include the compaction process. Additives can affect grain growth and phase transformation (Pan and Gong 2010). The effects of additives are not included in the grain growth models.

5.2 Modeling the sintering environment

The continuum scale modeling of SiC synthesis due to heat transfer is complex. This complexity is due largely to the varied and closely coupled heat transfer mechanisms that occur during the heating process. These mechanisms include conduction, convection, and radiation. Additionally, the primary heat sources are electromagnetic in nature, and as such, require the numerical solution of Maxwell's equations.

Because of this modeling complexity, a “bottom-up” approach was selected for this work. The approach, as its name suggests, begins with the successful development, execution, and validation of the simplest models and continues, iteratively, toward models of higher complexity. The first of these models consists of an infinite rod of constant radius and current density, for which an analytical solution exists. This model incorporates a

simplified version of the electromagnetic equations and is based on a solution to the electric scalar and vector potentials.

Following the infinite rod problem, the modified Lely method was selected as the next phase in the development process. The method involves sublimation of SiC from a hot powder source, transport of vapor through an inert gas environment, and condensation on a seed that is colder than the source. The deposition continues until a bulk crystal of reasonable size is grown. The method, in addition to low-frequency induction heating, requires the numerical modeling of several heat transfer mechanisms, including conduction, radiation, and potentially convection. The numerical modeling effort is further complicated by the fact that the growth apparatus is nonhomogenous, but is composed of several different materials types, with temperature-dependent properties.

The final phase of the bottom-up approach is still under initial development. This phase attempts to predict the temperature and stress field evolution during the SPS process. SPS is a powder consolidation technique that employs pulsed electric current and mechanical pressure to assist in the sintering process (Munoz 2010). This coupled electrical-thermal-mechanical analysis will not only incorporate all of the aforementioned modeling capabilities encountered in both the infinite rod problem and modified Lely method, but will also require modeling the stress distribution due to mechanical inputs.

The primary objective of this research is thus to provide a status of capabilities toward the ultimate goal of modeling the continuum SPS synthesis process. From an overall context, this includes providing sufficiently accurate thermal and stress field calculations to be used by other members of the Advanced Material Initiative (AMI) team.

5.2.1 Infinite rod

Process. As a first approximation to the solution of the set of electromagnetic equations, a static electromagnetic problem, with a known analytical solution was selected (Sass-Tisovskaya, M. 2009). Taking into account the assumptions of electroneutrality, quasi-steady state, and neglecting the Hall and induction currents, Maxwell's electromagnetic equations take the following form:

$$\nabla \cdot \mathbf{j} = 0 \quad (11)$$

$$\nabla \cdot \mathbf{B} = 0 \quad (12)$$

$$\nabla \cdot \mathbf{E} = 0 \quad (13)$$

$$\nabla \times \mathbf{B} = \mu_o \mathbf{j} \quad (14)$$

$$\nabla \times \mathbf{E} = 0 \quad (15)$$

$$\mathbf{j} = \sigma_c \mathbf{E} , \quad (16)$$

where

j = current density

\mathbf{B} = magnetic flux density

E = electric field

μ_o = magnetic permeability in a vacuum

σ_c = electric conductivity.

Combining the set of Equations 12-17, the potential form of the electromagnetic field may be written as:

$$\begin{aligned} \nabla \cdot (\sigma_c \nabla \phi) &= 0 \\ \nabla^2 A &= \sigma_c \mu_o \nabla \phi , \end{aligned} \quad (17)$$

where ϕ and A are the electric scalar potential and magnetic vector potential, respectively.

Consider an infinite rod of constant radius r_o , and a constant current density running parallel with the rod axis. The electrical conductivity is constant inside the rod, representing a hot argon gas column at a fixed temperature of $T = 10,600$ K.

Inside the cylinder, the analytic solution of the magnetic vector potential ($A_{x,in}$) takes the form

$$A_{x,in} = A_0 - \frac{\mu_o j_x r^2}{4}, \text{ if } r \leq r_o \quad (18)$$

where A_0 is the magnetic vector potential at the fixed temperature. Outside the cylinder, the magnetic vector potential ($A_{x,out}$) takes the form

$$A_{x,out} = A_0 - \frac{\mu_0 j_x r^2}{2} [0.5 + \ln(r/r_0)], \text{ if } r > r_0, \quad (19)$$

where j_x can be found via the current intensity I from:

$$j = \frac{I}{\pi r_0^2} \quad (20)$$

Because of the symmetry of the problem, the geometry was modeled as a two-dimensional, axisymmetric wedge, and a uniform hexagonal mesh was used. The boundary conditions for the magnetic scalar potential included zero gradients normal to all domain surfaces except the outer surface of the wedge. The electric scalar potential ϕ was prescribed similarly except for the two ends of the rod, which were fixed at $\phi = 0V$ and $\phi = 707V$.

Results. The numerical results are presented in Figures 26 and 27. The isolines corresponding to the electric potential (see Figure 26) run parallel to each other inside the rod and curve symmetrically outward from the rod. This pattern is due primarily to the prescribed boundary conditions for the electric potential. Figure 27 compares the numerical and the analytic solutions for the x-component of the magnetic vector potential along the radius of the domain ($x = 0.5E-2$ m) and shows good agreement with the analytical results computed from Equations 18 and 19.

5.2.2 Modified Lely method

Sublimation growth via the modified Lely method has been one of the most successful and most widely used SiC single crystal growth techniques of recent years (Klein et al. 2000). The process involves sublimation of SiC from a hot powder source, transport of vapor through an inert gas environment, and condensation on a seed that is colder than the source. The deposition continues until a bulk crystal of reasonable size is grown.

As shown in Figure 28, an SiC growth apparatus typically consists of a Radio Frequency (RF) copper coil, a quartz tube, a graphite susceptor, insulation, and an RF induction-heated graphite crucible containing

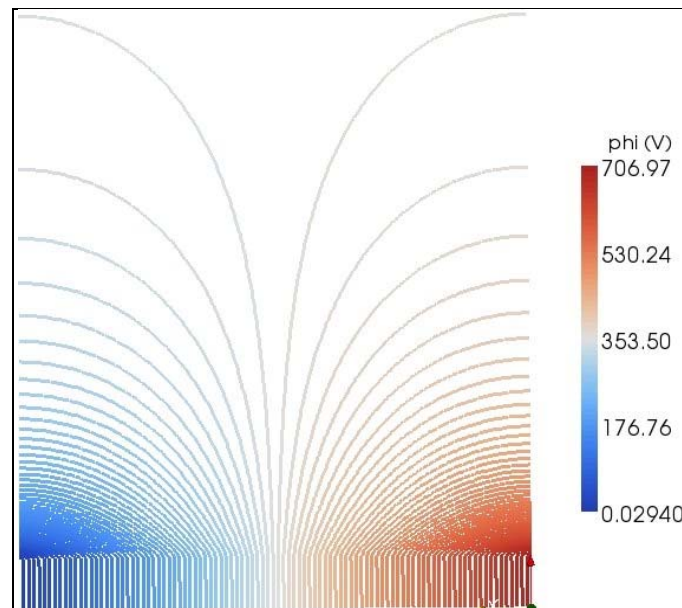


Figure 26. Electric potential isolines together with current density vectors.

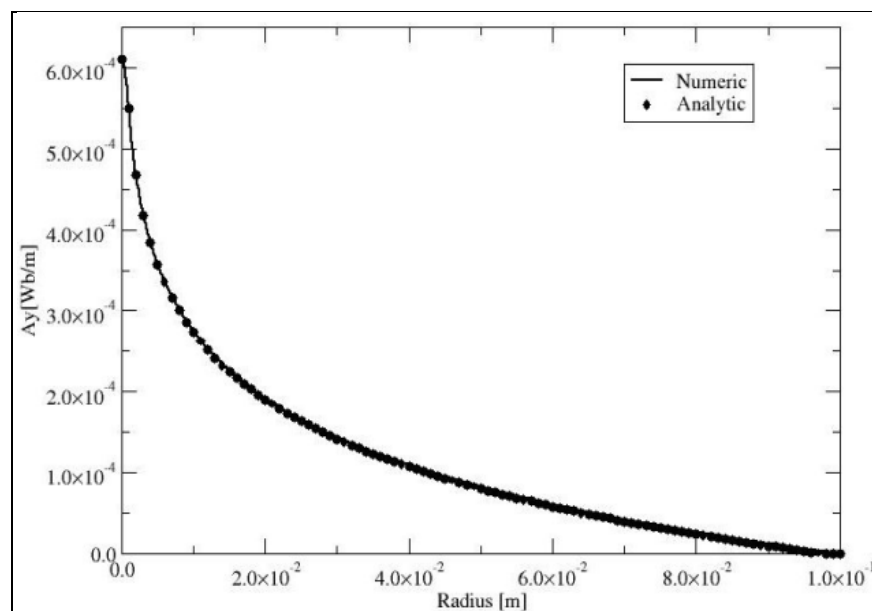


Figure 27. Numerical and analytical results.

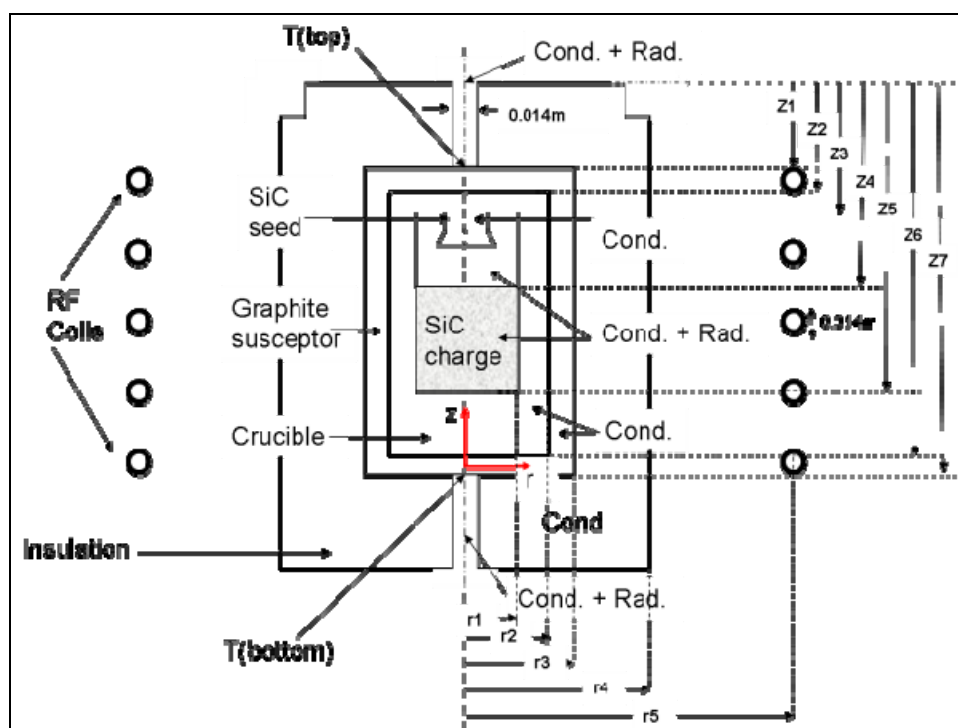


Figure 28. Schematic of the RF induction heating system for growth of SiC crystals.

polycrystalline SiC source powder and a single crystalline SiC seed. The SiC source powder is heated using RF induction heating via copper coils. The heating is generated from a current of approximately 10 kHz and 1200 amps. Due to the high electrical conductivity of the graphite susceptor, the time-harmonic electromagnetic field induces eddy currents therein, and heat is generated via the Joule effect. In general, the electromagnetic wave penetrates the susceptor within a skin depth of only a few millimeters, but is generally adequate to allow for sufficient heat generation within the inner growth region via conduction and radiation. Convection may also contribute in larger growth systems (Chen et al. 2001). The SiC charge powder is placed within the lower, heated portion of the crucible, and the seed crystal is placed above and is cooled with a blind hole. This temperature difference allows sublimation to occur at the source and crystallization to form at the seed.

The growth rate of the crystal has been shown in numerous studies to be strongly linked to the temperature distribution, particularly with respect to the temperature difference between the source and seed (Barrett et al. 1993; Kaneko 1993; Hofman et al. 1995; Bubner et al. 1999; and Ma et al. 2000;). Since SiC dissociates completely into liquid silicon and solid carbon at 3150 K, the growth temperature must remain below this upper

limit (Lilov 1993). The temperature distribution inside the growth system is determined via complex interactions among the various heat transfer mechanisms, and occurs within materials of different phases, including gases, solids, and porous media. The temperature further depends on several configuration control parameters, including coil position, heating voltage, and pressure.

Since favorable growth conditions are critically linked to the temperature distribution, its optimization is an important goal of apparatus design and control. However, because of the high temperatures (approximately 3000 K), experimental verification of the correlation between the properties of the crystal, the temperature distribution, and external control can be difficult. As a result, accurate numerical simulations have become highly desirable.

The primary objective of this phase of the work is to develop a coupled, high-resolution heat transport model to predict the electromagnetic field and temperature variation due to RF heating during SiC crystal synthesis using the modified Lely method. The model proposed here can be used to investigate the effects of variable current intensity and coil position on the temperature distribution within the growth chamber.

5.2.3 Electromagnetic field

The electromagnetic field produced by RF induction heating can be calculated using Maxwell's equations. For low-frequency ($f < 1$ MHz) induction heating, Maxwell's equations can be simplified using the quasi-steady-state approximations. Assuming the current in the coil is time-harmonic, the magnetic flux density can be expressed as the curl of a magnetic vector potential, $\mathbf{B} = \nabla \times \mathbf{A}$. The Maxwell equations can then be written in terms of the vector potential, \mathbf{A} (Jackson 1998):

$$\nabla \times \left(\frac{1}{\mu_m} \nabla \times \mathbf{A} \right) + \epsilon_m \frac{\partial^2 \mathbf{A}}{\partial t^2} + \sigma_c \frac{\partial \mathbf{A}}{\partial t} = \mathbf{J}_{coil} \quad (21)$$

where

- μ_m = magnetic permeability
- \mathbf{A} = magnetic potential vector
- ϵ_m = permittivity

σ_c = electrical conductivity
 \mathbf{J}_{coil} = current density in the coil.

If the coil and the electromagnetic field are assumed axisymmetric, both the magnetic potential vector \mathbf{A} and the current density \mathbf{J}_{coil} will have only one angular component with an exponential form, such that

$$\mathbf{A} = \begin{Bmatrix} A_0 e^{i\omega t} + 0 \\ 0 A_0 e^{-i\omega t} \end{Bmatrix}; \mathbf{J}_{coil} = \begin{Bmatrix} J_0 e^{i\omega t} + 0 \\ 0 J_0 e^{-i\omega t} \end{Bmatrix} \quad (22)$$

where i is the complex unit, and ω is the angular frequency. The final equation for vector potential, \mathbf{A} , is obtained by substituting Equation 23 into 22:

$$\left(\frac{\partial}{\partial r^2} + \frac{1}{r} \frac{\partial}{\partial r} - \frac{1}{r^2} + \frac{\partial^2}{\partial z^2} \right) \left(\frac{\mathbf{A}_0}{\mu_m} \right) + \varepsilon_m \omega^2 \mathbf{A}_0 - i\omega \sigma_c \mathbf{A}_0 = -\mathbf{J}_0 \quad (23)$$

The second term in the left side of Equation 24 is negligible. The following boundary conditions can be used to solve this equation,

$$\mathbf{A}_0 = 0 \text{ at } r = 0 \text{ and } (r^2 + z^2) \rightarrow \infty \quad (24)$$

which is based on the conditions that magnetic flux density \mathbf{B} is axisymmetric and the computational domain is sufficiently large (Wu et al. 2005). After Equation 24 is solved for the vector potential \mathbf{A} , the generated heat power in the graphite susceptor can be obtained using the principles of eddy current:

$$q_{eddy} = \frac{1}{2} \sigma_c \omega^2 (A_r^2 + A_i^2) \quad (25)$$

5.2.4 Radiation heat transfer

Diffuse gray radiation is modeled using heat flux boundary conditions at the relevant heat exchange surfaces. For this work, these include the surfaces pertaining to the SiC source powder and the growth chamber filled with inert gas. Additionally, radiation heat transfer modeling may also be applied to the top and bottom cooling holes.

In general, heat flux can consist of idealized radiation:

$$-k \frac{\partial T}{\partial n} = \sigma \epsilon (T^4 - T_{ext}^4) \quad (26)$$

where

σ = Stefan-Boltzmann constant

n = surface normal

ϵ = surface emissivity (considered herein constant for each surface)

T_{ext} = external temperature.

If the surface k is receiving radiation from another surface i in the system, then the heat flux may be represented using Elmer software

(<http://www.csc.fi/english/pages/elmer>) as

$$-k_k \frac{\partial T_k}{\partial n_k} = \sigma \epsilon_k \left(T_k^4 - \frac{1}{A_k \epsilon_k} \sum_{j=1}^N G_{jk} \epsilon_j T_j^4 A_j \right) \quad (27)$$

where the parameters A_j and A_k refer to the j and k specific surface areas, respectively, and the factors G_{ik} represent the Gebhardt factor:

$$G_{jk} = \frac{Q_{jk}}{\epsilon_j A_j \sigma T_j^4} \quad (28)$$

Here Q_{jk} is the heat transferred from surface j to k , and is computed from the product of the view factors F_{jk} and the radiosity J_j :

$$F_{jk} = \frac{Q_{jk}}{A_j J_j}. \quad (29)$$

5.2.5 Material properties

The temperature-dependent material properties were taken from the literature (Chen et al. 2001). The SiC source material was modeled with an average grain size d_p of 125 μm (Sasaki et al. 1998) and was treated as a porous medium with porosity ϵ_p and effective specific heat (C_p)

$$(\rho c_p)_{eff} = (1 - \varepsilon_p)(\rho c_p)_{SiC} + \varepsilon_p(\rho c_p)_{gas} \quad (30)$$

where ρ is the density, and a porosity of 0.4 was utilized (Chen et al. 2001).

The heat transfer inside the charge consists of both radiative and conductive components; as such, an expression for the effective thermal conductivity must account for both of these components. From Kansa et al. (1977),

$$k_{eff} = (1 - \varepsilon_p)k_{SiC} + \varepsilon_p \left(k_{gas} + \frac{8}{3} \varepsilon 4 \sigma T^3 d_p \right) \quad (31)$$

5.2.6 Convective heat transfer

The relative importance of convective heat transfer (particularly natural convection due to buoyancy effects), within the context of the aforementioned crucible dimensions, as well as the processing temperature and pressure conditions, may be approximated by the dimensionless Rayleigh number:

$$Ra = Gr * Pr = \frac{g\beta}{\nu\alpha} \Delta T D_c^3 \quad (32)$$

where

Gr = Grashoff number

Pr = Prandtl number

β = thermal expansion coefficient

ν = kinematic viscosity

α = thermal diffusivity

g = acceleration due to gravity

ΔT = temperature difference between the crucible wall and the quiescent gas

D_c = diameter of the crucible.

For a typical growth system composed of argon gas, at a pressure of 3.0E4 Pa, temperature of 2900 K, and temperature difference of 30 K (Chen et al. 2001), the Rayleigh number may be anywhere between 1.98 and 15.84 for representative (industry standard) crucible diameters between 50 and

100 mm, respectively. Since this is significantly less than the critical Raleigh number Ra_c , it is evident that the heat transfer by natural convection can be neglected in these studies (Reid and Harris 1958). If however, the crucible diameter is increased (i.e., by a factor ≥ 4), the relative importance of the buoyancy effects requires the inclusion of convective transport modeling.

5.2.7 Numerical method

In concert with Equations 26, 32, and 33, the equation governing the evolution of temperature for the growth system can be stated as

$$(\rho c_p)_{eff} \frac{\partial T}{\partial t} = \nabla \bullet (k_{eff} \nabla T) + q_{eddy} \quad (33)$$

Additionally, the boundary conditions corresponding to surface heat flux (Equation 28) and magnetic vector potential (Equation 25) are applicable.

The variational form of Equation 35, after integration by parts of the conduction term and the application of the divergence theorem yields

$$\begin{aligned} & \int_{\Omega} \frac{\partial T}{\partial t} v_i d\Omega + \int_{\Omega} \frac{k_{eff}}{(c_p \rho)_{eff}} \nabla T \cdot \nabla v_i d\Omega \\ &= \int_{\Omega} \frac{q_{eddy}}{(c_p \rho)_{eff}} v_i d\Omega + \int_{\Gamma} \frac{1}{(c_p \rho)_{eff}} (k_{eff} \nabla T) \cdot \mathbf{n} v_i d\Gamma \end{aligned} \quad (34)$$

where

- v_i = basis function
- Ω, Γ = elemental volume and its enclosing surface, respectively
- \mathbf{n} = unit normal vector to the surface.

The linearized partial differential equation for the temperature (T) in the variational formulation is stated as:

$$M_{ij} \frac{\partial T_j}{\partial t} + A_{ij} T_j = F_i \quad (35)$$

where

M_{ij} = mass matrix
 A_{ij} = stiffness matrix
 F_i = force vector.

Comparing Equation 34 and 35 leads to the following:

$$\begin{aligned}
 M_{ij} &= \int_{\Omega} v_j v_i d\Omega \\
 A_{ij} &= \int_{\Omega} \frac{k_{eff}}{(c_p \rho)_{eff}} \nabla v_j \cdot \nabla v_i d\Omega \\
 F_i &= \int_{\Omega} \frac{q_{eddy}}{(c_p \rho)_{eff}} \nabla v_i d\Omega + \int_{\Gamma} \frac{q_n}{c_p \rho} v_i d\Gamma
 \end{aligned} \tag{36}$$

where $q_n = k_{eff} \nabla T \cdot \mathbf{n}$ is the heat flux perpendicular to the surface normal.

The numerical integration of Equation 35 over each quadrilateral element is approximated by the sum over all Gauss-point contributions, and solved using the open-source, multiphysics simulation software Elmer (<http://www.csc.fi/english/pages/elmer>). Time-stepping was performed using a second-order Crank Nicolson scheme and was solved to steady-state convergence with an error tolerance of approximately 1.0 E-5.

5.2.8 Results

A computational domain of 0.25 by 0.4 m was selected for this work, and its size verified to allow for a sufficiently diminishing magnetic potential at the far-field boundaries, where, in accordance with Equation 25, a zero magnetic potential condition was imposed. A grid composed of 20,916 unstructured elements was used, and clustering was performed around the areas of high-temperature gradients (Figure 29). Figure 30 shows the in-phase (A_r) and out-of-phase (A_i) contours of magnetic potential, for five turns of coil, a current of 1200A, and a frequency of 10 kHz. As indicated, the contours are concentrated along the outer portion of the graphite susceptor and tend to bend inwards along the top and bottom of the susceptor. The in-phase component reaches its maximum strength (~ 0.0018 Webers/m) around the coil, with its shape being highly influenced by the geometry of the coil. A_i , in contrast, shows a maximum magnitude of approximately 0.00017 Webers/m and is located both near the coil and within the graphite susceptor. Of particular interest is the fact that both A_i and A_r potentials show comparable strength within the graphite susceptor and suggest the need to include both components.

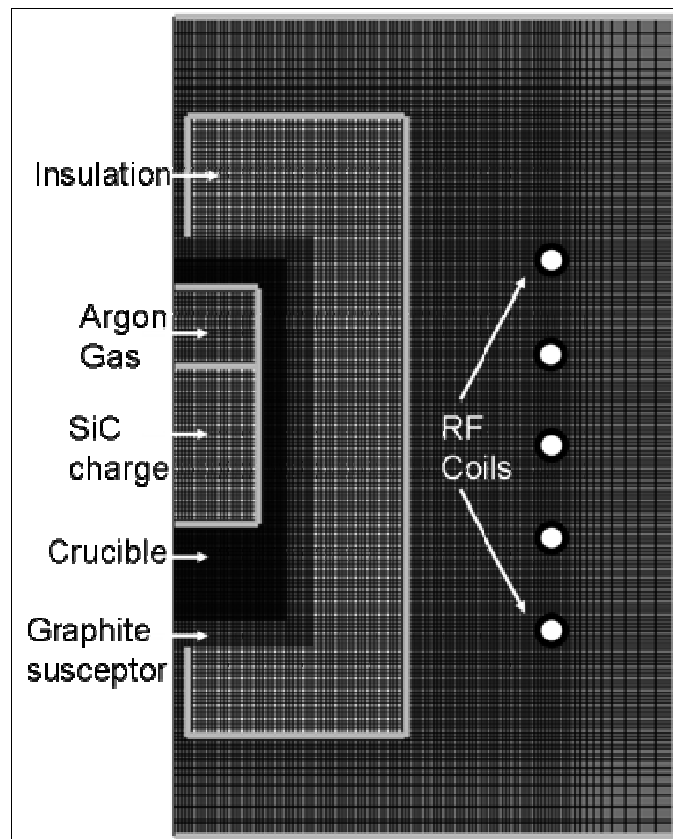


Figure 29. Computational grid for finite element method.

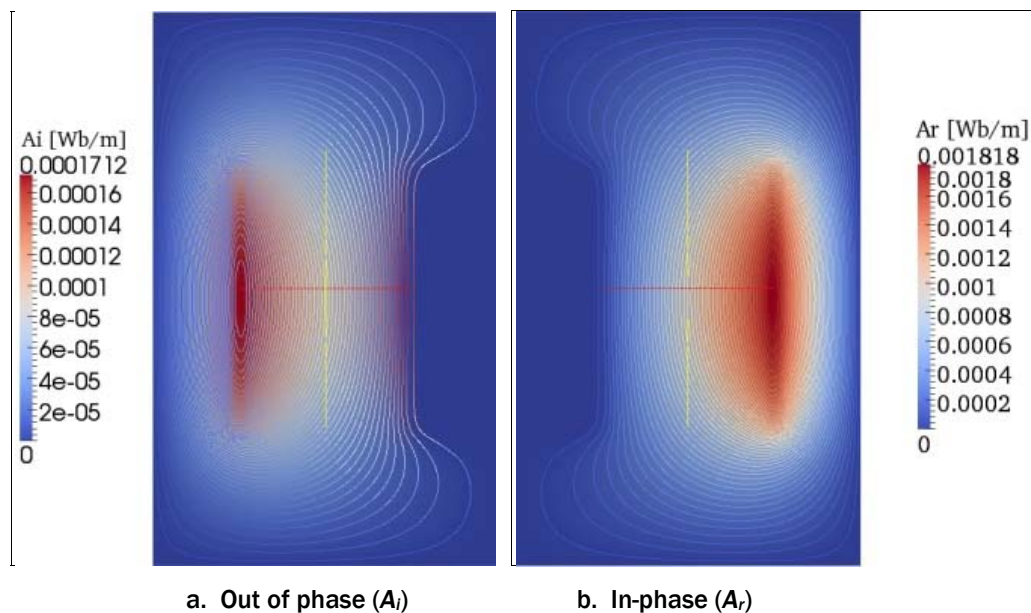


Figure 30. Contours of magnetic potential, out of phase (A_i) and in-phase (A_r), for a current of 1200 Amps and a frequency of 10 kHz.

Figure 31 compares eddy current heat generation with the existing literature (Chen et al. 2001). Specifically, the heat generation within the SiC powder charge, the crucible (modeled as an inert gas), and the graphite susceptor are shown along the radial direction (r) at the various heights (z), corresponding to $z = 0.0$, $z = 1.3R_s$, and $z = 2.6R_s$ (where R_s is the outside radius of the susceptor, $R_s = 0.07$ m). As indicated, the heat power is generated primarily in the outer portion of the graphite susceptor and reaches an approximate value of $8.7 \text{ E6 Joules/m}^3$. The discontinuity between $r/R_s = 0.6$ and $r/R_s = 0.8$ occurs as a result of the intermediate inert gas material. The heat generated within the SiC charge at $z = 1.3R_s$ is somewhat negligible compared with that generated in the graphite susceptor at $z=0$ and $2.6R_s$, showing an approximate difference of two orders of magnitude. Overall, the numerical results of this study compare well with the results of Chen et al. (2001).

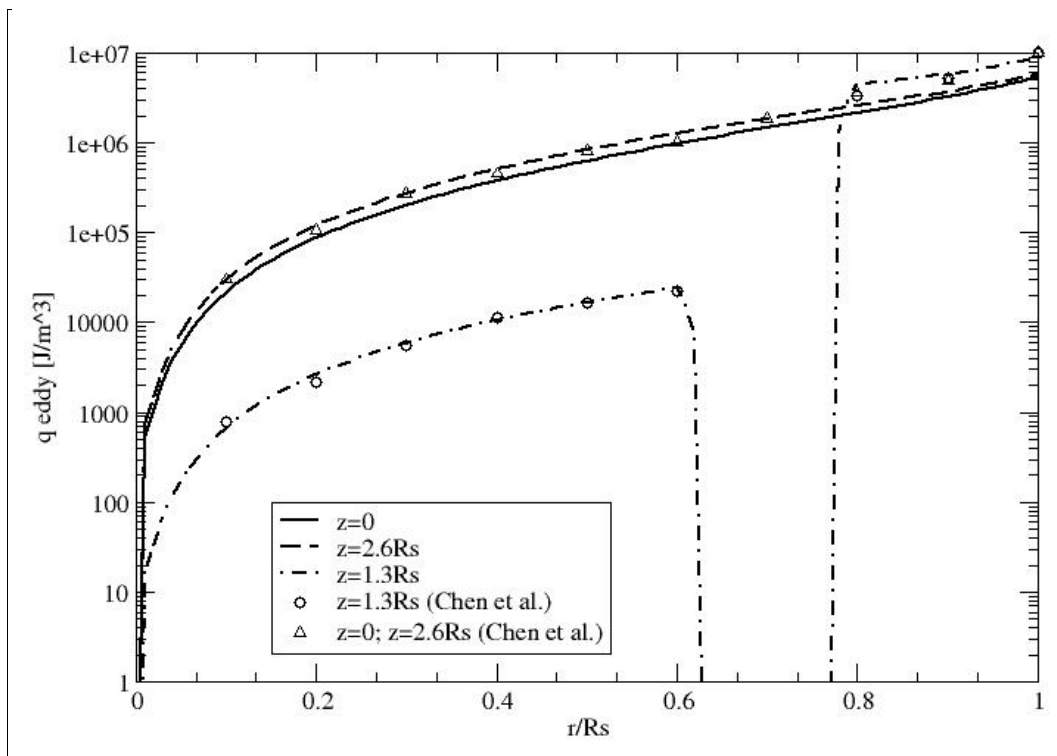


Figure 31. Comparison of generated heat power along the radial direction at different heights with results from Chen et al. (2000).

Figure 32 shows the temperature distribution for all components minus the coil apparatus. As indicated, the maximum temperature (~ 3075 K) exists within the graphite susceptor, along the geometric center of the induction coil, and extends radially inward towards the SiC source powder. The coil geometry is thus responsible for the location of the highest tempera-

ture distributions within the source powder, and therefore the first temperature distribution has been documented in several studies (e.g., Chen et al. 2001), which show these attributes to be highly correlated.

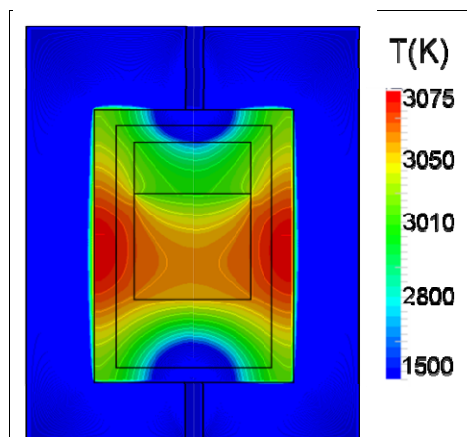


Figure 32. Temperature contours for a current of 1200 A and frequency of 10 kHz.

The process of sublimation continues as a result of the temperature difference that exists between the source powder and the seed. As shown in Figure 32, the temperature at the top of the growth chamber (T_{top}) is cooled by a hole exiting to the outside air. This hole helps maintain the positive temperature difference between the source and the seed and thus facilitates the continued sublimation growth at the seed. This temperature difference is approximately 80 K and allows for a sufficiently high growth rate. Further, this hole helps to maintain a proper radial temperature gradient at the seed (i.e., thermal variations of less than 10K at the seed surface) that ensures low thermal stresses, which subsequently assist in minimizing dislocations and micropipes (Chen et al. 2001).

The effect of radiation modeling on the temperature distribution can be seen in Figure 33. The temperature difference between neighboring isolines is 10K. As shown, neglecting radiation-modeling results in large heat gradients inside the growth chamber, where experiments have shown the temperature distribution to be nearly homogeneous. As stated previously, these erroneous predictions can lead to false conclusions not only with respect to the formation of dislocations and micropipes resulting from uncharacteristically high thermal stresses but also with respect to SiC crystal growth rates (Chen et al. 2001).

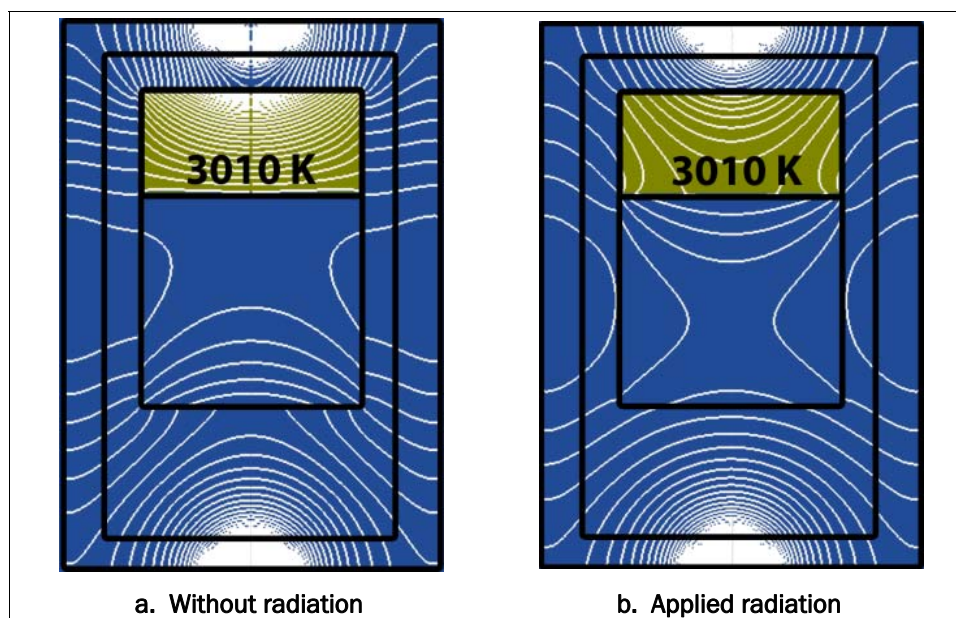


Figure 33. Effect of applying radiation to the numerical simulation.

5.3 Conclusions

A comprehensive process model for SiC growth by the modified Lely method has been developed that accounts for axisymmetric geometries, induction heating, radiation, and conductive heat transfer. The model has been successfully applied to the simulation of SiC growth and compared with existing numerical experiments (Chen et al. 2001). Computations of the magnetic potential showed the relative importance of including both the in-phase and out-of-phase components, with comparable magnitudes existing within the graphite susceptor. The graphite susceptor with its relatively high conductivity was shown to function as a barrier to the electromagnetic field, allowing only a negligible amount of eddy-induced heating within the inner crucible and growth region. By contrast, a significant amount of eddy current energy was created in the outer portion of the susceptor within a relatively small skin depth. The maximum temperature distribution was found to exist in the graphite susceptor, and at the level of the geometric center of the induction coils. Within the SiC charge, the temperature was highest in the central region near the crucible wall. The positive temperature difference between the SiC charge and the ambient air-cooled seed allows for the sublimation in the charge and deposition on the seed. The effect of radiation modeling was significant, particularly given the high-temperature ranges appropriate to this study, and resulted in a substantial decrease in temperature gradients within the growth chamber.

Future simulations will evaluate the effects of buoyancy by convection caused by increasing the growth chamber dimensions. These simulations will necessarily require the coupling of the current model with the compressible Navier-Stokes equations.

5.3.1 Spark plasma sintering

This phase of the work attempts to predict the temperature and stress field evolution during the Spark Plasma Sintering (SPS) process. SPS is a powder consolidation technique that employs pulsed electric current and mechanical pressure to assist in the sintering process (Munoz 2010).

While several recent studies have used the finite element method to investigate the current and temperature distributions in the SPS process (Anselmi-Tamburini et al. 2005; Antou et al. 2009; McWilliams and Zavaliangos 2008; Vanmeensel et al. 2005; Wang et al. 2007; and Zavaliangos et al. 2004), the mechanical input and the resulting stress distributions have largely been neglected. Experimental studies show this to be a significant omission because the processing pressure is a crucially important densification mechanism (Anselmi-Tamburini et al. 2006); (Munir et al. 2006). Only a few exceptions exist that include coupled electrical–thermal–mechanical analysis (e.g., Munoz et al. 2010; Wang et al. 2007; and Antou et al. 2009).

This work will also incorporate a coupled electrical-thermal-mechanical analysis and will use one or more of the references cited in the preceding paragraphs for validation. Clearly the modeling effort will not only incorporate the capabilities demonstrated in both the infinite rod problem and modified Lely method, but will also require the need for modeling the stress distribution due to a mechanical input and will thus require solutions to the strain displacement relations.

The outputs that will be provided to other AMI researchers from the continuum SPS model will therefore include the thermal and stress fields contained within the growth chamber.

6 Material Diagnostics

A large amount of research has been performed in the scientific community to understand the mechanical properties of various materials, and how they may be influenced by factors such as stress states, length scales, and the internal structure of the material. As discussed in Horstemeyer (2009) on multiscale modeling, Bazant and Chen (1997) summarized the research to date on length scale effects on properties. As early as the 1500's DaVinci claimed two ropes of equal thickness and material but with different lengths exhibited different tensile strengths: the longer of the two ropes would not be as strong as the shorter rope. As for compressive strength, in the 1700's, Euler examined column length with respect to buckling. Research performed by Cauchy in the 1800's and Bridgman (1923) in the 1900's examined stress state effects on materials. More currently, as technology progressed and diagnostic capabilities improved, Griffith (1921) pioneered fracture mechanics developing Griffith's criterion, which is most applicable to brittle materials, while Irwin's (1957) research group included plasticity to better predict the fracture behavior of ductile materials. Additionally, Olson (1998, 2000) identified how various structures such as grains, defects, and inclusions in a certain material will influence the material's properties.

To assist the modeling effort at the U.S. Army Engineer Research and Development Center (ERDC), the Center for Advance Research and Material Characterization (CARMA), ERDC, is being used to support the polycrystalline center-directed research project. The CARMA is equipped with Zeiss optical microscopy (OM) workstations and an environmental scanning electron microscope (eSEM) manufactured by FEI Company, Hillsboro, OR, which allows for micro- and nano-scale material characterization. Mechanical property information at submicron length scale is obtained by a nanoindenter (Agilent, Santa Clara, CA) and an in situ SEM picoindenter (Hysitron, Minneapolis, MN). At higher length scales, universal testing machines (Instron, Norwood, MA) and load frames by MTS, Eden Prairie, MN, with loading capabilities ranging from 5 kN to 200 kN provide stress state and temperature effects analysis for quasi-static and cyclic loading conditions. The CARMA is also capable of characterizing elemental composition of materials by implementing either a wavelength-dispersive X-ray fluorescence (XRF) spectrometer

(Panalytical, Almelo, The Netherlands) or an energy-dispersive X-ray (EDX) spectrometer detector (Bruker, Billerica MA) attached to the eSEM. The arrangement of atoms within a crystal structure may be characterized with a Panalytical X-ray diffractometer (XRD). Besides the characterization capabilities at CARMA, collaborations between various universities and government laboratories have been initiated. Carnegie-Mellon University will assist in 3-D microstructure analysis; the Center for Advanced Vehicular Materials (CAVs) at Mississippi State University provided their image analysis program; the Beckmann Institute at the University of Illinois Urbana-Champaign provides additional material testing and characterization capabilities; and the Center for Advanced Microstructures and Devices (CAMD) at Louisiana State University will provide in situ XRD mechanical testing and computed tomography.

This chapter discusses characterization and testing performed to date of fracture toughness, elastic modulus, hardness, grain size, and crystalline phases examined for a commercially available SiC, which will aid in providing the necessary structure-property relationships of various polycrystalline materials to aid in microstructure-based model development, calibration, and validation efforts at the ERDC.

6.1 Material preparation

Laboratory capabilities were demonstrated through tests of as-sintered SiC commercially available from Saint-Gobain Ceramics, Amherst, NY, obtained from the Army Research Laboratory (ARL), Adelphi, MD. The original size of the as-received tile was 4.22 by 4.22 by 0.36 in. The fracture toughness, nanoindentation, and XRD specimens were all machined from the same tile. In addition, material from the tile was subjected to grain size analysis. Fracture toughness specimens were machined using a Secotom-10 high-precision cut-off saw with a diamond wheel oil-cooled blade (Struers, Westlake, OH). Machined specimens had dimensions of 0.2 by 0.3 by 3.0 in. with cutting occurring down the length of the 0.2-in. sides. Surface grinding occurred on the 0.3-in. side with a 36-micron diamond wheel to remove surface defects from manufacturing.

After initial machining, a digital caliper (Mitutoyo, Chicago, IL) measured the dimensions of the length, width, and thickness of the fracture toughness specimen. Three measurements for each direction were obtained. Additionally, for density determinations of the fracture

toughness specimens, a laboratory balance (Sartorius, Bradford, MA) measured the wet and dry masses of the specimens.

Once the mass and dimensional measurements were completed, the fracture toughness specimens were notched by precision cuts in the center of the specimens using a 0.015-in.-thick diamond wheel resulting in a ratio of average notch depth to specimen depth, a_o/d , of 0.378. An optical microscope (Imager, Zeiss, Thornwood, NY) was used to examine the notch depths after machining, as depicted in Figure 34.

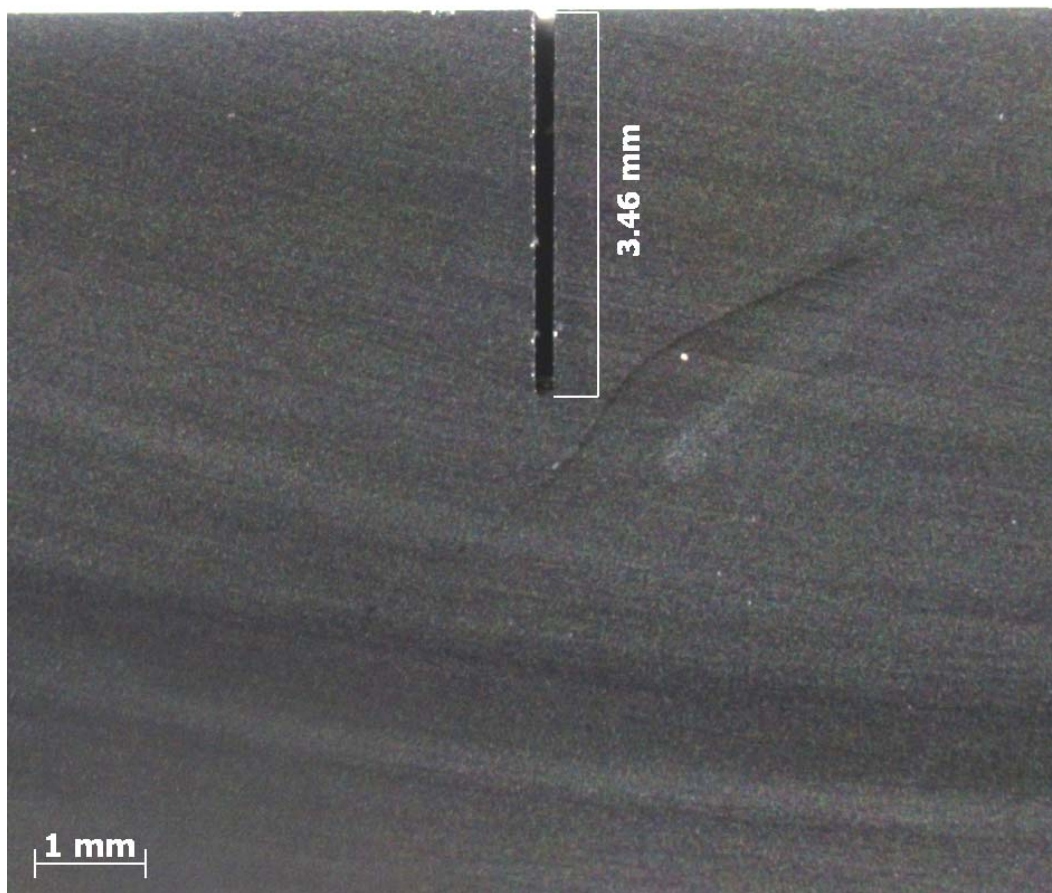


Figure 34. Optical micrograph image of 0.015-in.-thick notch.

Noticeable machining damage is evident for the specimen in Figure 34, which is representative of the other specimens as well. As Srinivasan and Seshadri (1980) previously reported, the cracked grains act as natural flaws from which fractures initiate, obviating the need for precracking the specimens prior to testing.

The bulk density of the fracture toughness specimens was performed by the Archimedes water immersion method according to ASTM B311-08 (American Society for Testing and Materials 2008). Srinivasan and Seshadri (1980) used this technique previously to quantify the bulk density of a sintered SiC.

Figure 35 represents the 4-point bend-loading configuration used to test ten single-edge notched-beam (SENB) specimens. An Instron 8852 (Norwood, MA) load frame loaded the specimens to fracture at a crosshead velocity of 0.02 in./min with load and displacement data recorded until fracture.

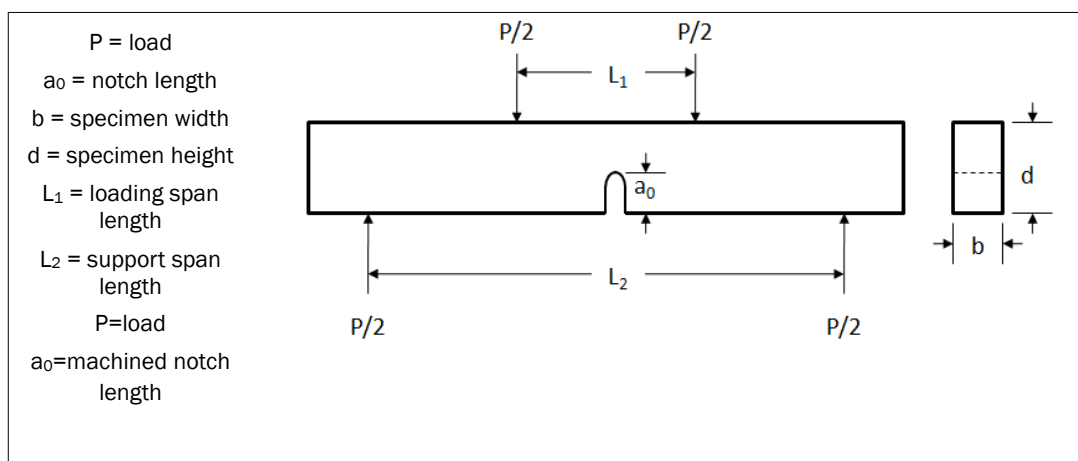


Figure 35. Loading configuration for SENB specimens.

Table 2 details the dimensions for the testing configuration shown in Figure 35.

Table 2. Loading and support span lengths for the SENB specimens.

	Distance (in.)
Loading Span L_1	0.6
Support Span L_2	1.8

An FEI Nova eSEM 630 field emission gun scanning electron microscope (FEG-SEM) provided fracture surface analysis of the fracture toughness specimens while chemical composition analysis used the energy-dispersive X-ray (EDX) detector attached to the eSEM.

The nanoindentation specimen was machined using a Struers Secotom-10 high-precision cut-off saw with diamond wheel oil-cooled blade. The nanoindentation specimen dimensions were 0.5 by 0.5 by 0.36 in. After machining, the specimen was mounted in 1.25-in. diameter molds using a commercially available epoxy (EpoMet, Buehler, Lake Bluff, IL). The procedure used for performing stepwise polishing of the specimens is outlined in Table 3.

Table 3. Polishing of SiC for Nanoindentation.

Step	Abrasive/Size	Base Speed (rpm)	Load (lbf)	Time (min:sec)
1	35-micron diamond pad	240	6	Until plane
2	9-micron diamond paste	240	6	8:00
3	3-micron diamond paste	120	6	6:00
4	0.05micron colloidal silica	120	6	4:00

The specimens were ultrasonically cleaned with ethanol between polishing steps while still held in the automatic polishing specimen holder to ensure that polishing occurred only in the one direction. Once the polished surface was analyzed in the SEM, the specimen was placed in a Nano Indenter G200 (Agilent, Englewood, CO) with a Berkovich indenter tip. The nanoindenter performed load control experiments on the SiC samples at maximum loads of 5, 10, 50, 100, 200, and 400 mN using the traditional quasi-static (QS) method and the continuous stiffness measurement (CSM) method. To compare the results of these experiments with previous work performed by Guicciardi et al. (2007), the DSI experiments were performed at a loading and unloading rate of 2.5 mN/s with no hold time. The CSM experiments were performed at a surface approach velocity of 10 nm/s, a strain rate of 0.05/s, and a target frequency of 45 Hz. Both methods performed a minimum of ten indents placed 50 μ m apart. Machine compliance and thermal drift are automatically accounted for with the G200 testing software, which are based on the Oliver and Pharr (1992) analysis of nanoindentation data. A standard fused silica reference sample was used for tip area calibration.

The bright field image feature of a Zeiss Imager Z1m optical microscope in reflected mode presented the images necessary for grain size analysis. Specimens were polished according to the procedure detailed previously in Table 3. After polishing, the sample was etched for grain size analysis using a modified Murakami's solution outlined in Table 4.

Table 4. Modified Murakami's solution used for etching.

Constituent	Amount
Distilled Water	100 mL
Sodium Hydroxide	3 g
Potassium Ferricyanide	30 g

An optimal etching time of 30 minutes in the boiling solution yielded visible grain boundaries. The image analysis process used a MATLAB program developed at CAVs to post-process the optical microscopy images and provided the statistical data of the microstructure as described in Allison et al. (2011).

6.2 Results and discussion

Calculations of fracture toughness values implemented the equation by Brown and Srawley (1966), which Srinivasan and Seshadri (1980) used for calculations of their values as reported in Table 5. Fracture toughness values reported by the manufacturer for SENB experiments are also included in Table 5, although the equation and initial notch depth ratio were not provided.

Table 5. Mechanical property results for the fracture toughness specimens.

Mechanical Property	Experimentally Determined Value (this study)	Manufacturer Reported Value (Saint-Gobain Advanced Ceramics 2010)	Value Calculated by Srinivasan and Seshadri (1980)
Density (g/cm ³)	3.13±0.05	3.13	3.125-3.155
Fracture toughness (MPa x m ^{0.5})	4.65±0.483	4.60	4.783±0.277
Initial Notch Depth Ratio (a_0/d)	0.378±0.003	N/A	0.408±0.005

Table 5 reports the average and standard deviation of 10 specimens for this study. Slight differences in specimen preparation, geometry, and material are likely causes for the difference in the average fracture toughness values reported. However, the data for this study agree with manufacturer's reported values.

An FEI Nova SEM 630 FEG-SEM provided fracture surface analysis images. Under quasi-static loading the SENB specimen exhibited predominately transgranular fracture as Figure 36 exhibits.

The predominant transgranular fracture observed on the fracture surfaces in this study was very similar to the transgranular fracture depicted in Shih et al. (1998) of a conventional SiC loaded quasi-statically in flexure that used boron and carbon as sintering aids.

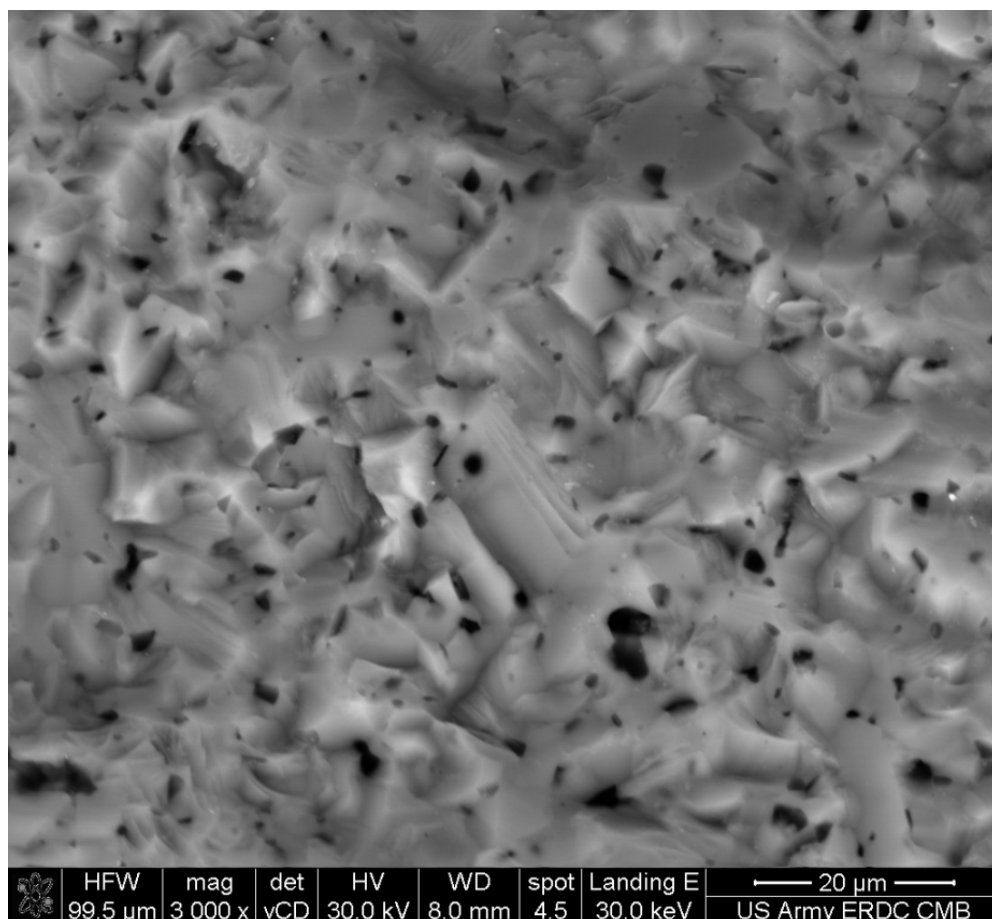


Figure 36. Fracture surface of SENB test specimen.

The indentation modulus of the SiC sample determined by the QS and CSM methods are plotted in Figure 37 in which Young's modulus is plotted versus the maximum indentation load applied during testing. The modulus was determined by the nanoindenter TestWorks v4.8 software, which automatically corrects for thermal drift and machine compliance.

In Figure 37, most noticeable is the reduction in modulus for the QS method data when loads exceeded 10 mN. This reduction indicates more of a bulk modulus response influenced by microstructural features such as porosity instead of a modulus response of the individual phases at lower loads. The CSM method did not depict this trend; only the scatter of the data appeared reduced at loads greater than 10 mN. Both methods did

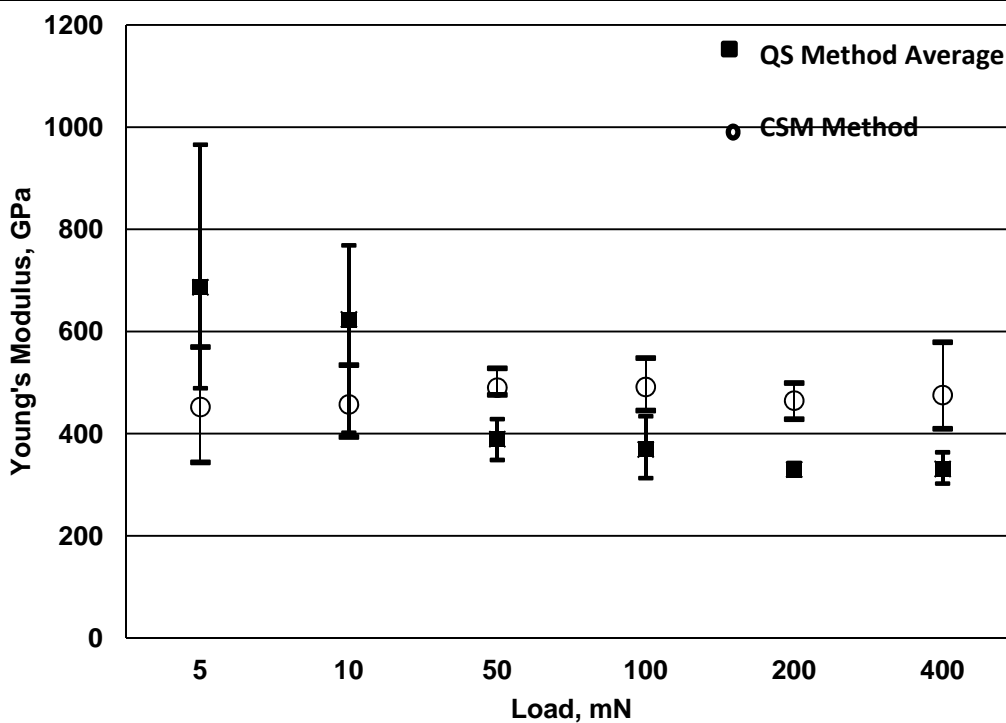


Figure 37. Plot of Young's modulus calculated using Oliver and Pharr (1992) versus peak indentation load. Bars represent maximum and minimum values of each data set.

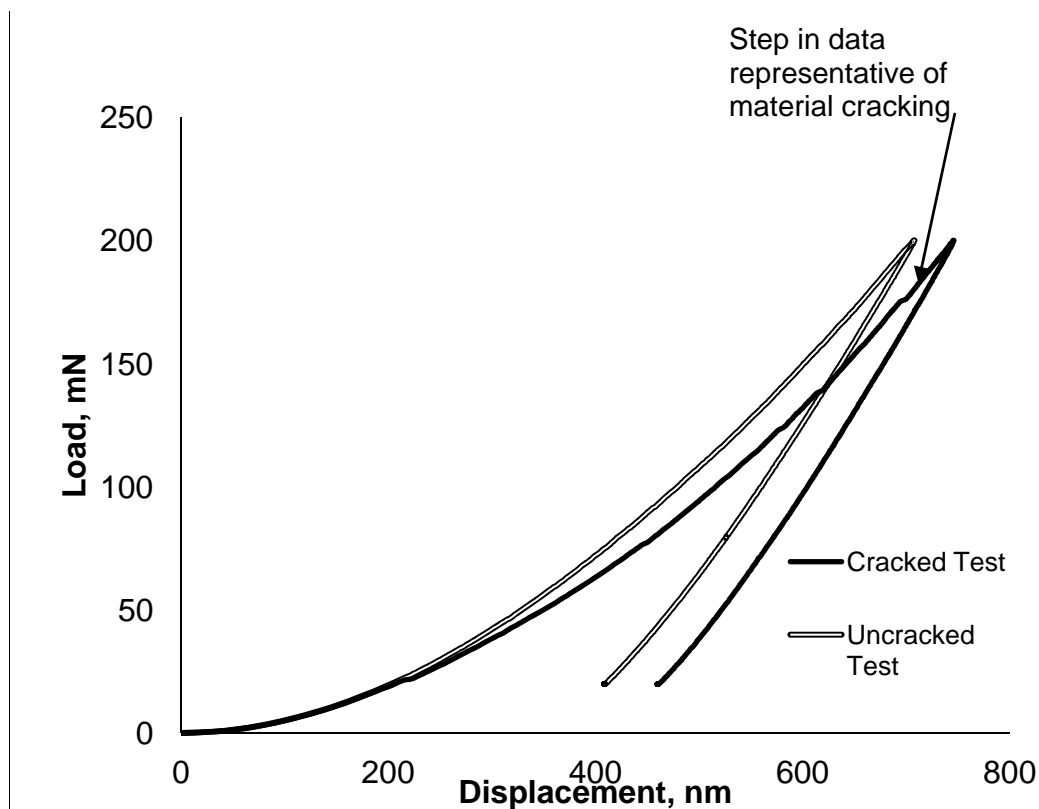


Figure 38. Load versus displacement curves of QS nanoindentation method experiments for a cracked and uncracked test.

depict larger amounts of scatter at maximum loads below 10 mN with the exception of the CSM data at 400 mN. The CSM data appears to show much more stability than the QS data in the average data points for the material across the various maximum loads. The reported bulk modulus of elasticity from the manufacturer's data sheet is 410 GPa. The manufacturer did not report how the modulus value was measured. Both QS and CSM method averages appear to overpredict the modulus reported by the manufacturer below 10-mN loads; however, the QS method did capture the manufacturer's reported value in the scatter of the data at 5 mN while both captured the reported value at 10 mN. This trend suggests that at lower loads the methods were not capturing a bulk modulus of elasticity value. At loads above 10 mN the scatter in the data decreased for both methods. At 50- and 100-mN loads, only the QS method captured the manufacturer's reported bulk modulus while the data for the CSM method was slightly increased. For maximum loads of 200 and 400 mN the QS data exhibited lower modulus values than the CSM method data. The deviation between the CSM and QS data at higher loads might be due to the fact that the QS method provides data in observable steps, allowing experiments with cracking to be identified and removed from the data sets prior to making statistical comparison. Figure 38 depicts load-unload curves for the QS method with cracked and uncracked responses.

A noticeable step in the load displacement curve is visible for the cracked test in Figure 38. Analyzing every load displacement curve for the QS method data allows researchers to determine invalid tests that do not represent valid measurement of modulus for intact material.

Hardness results are reported for the QS and CSM methods in Figure 39. The hardness was determined by the nanoindenter TestWorks v4.8 software, which automatically corrects for thermal drift and machine compliance.

As observed with the modulus data reported in Figure 37, the hardness data shown in Figure 39 exhibits less scatter at loads above 10 mN. Unlike the modulus data, the hardness data exhibit much greater overlap between values obtained by the QS and CSM methods. In addition, the average CSM results display less dependence on load than the average QS results.

Figure 40 provides a post-processed image of the etched SiC grains after using the MSU image analyzer program. The grains are shown as gray ob-

jects in the image, while the black objects are pores. Only the gray objects are analyzed for grain size measurements. A total of five images were analyzed for grain size measurements.

The average grain size diameter determined from the image analysis software was $6.5\text{ }\mu\text{m}$, which correlates to the manufactured reported grain size of 4-10 μm .

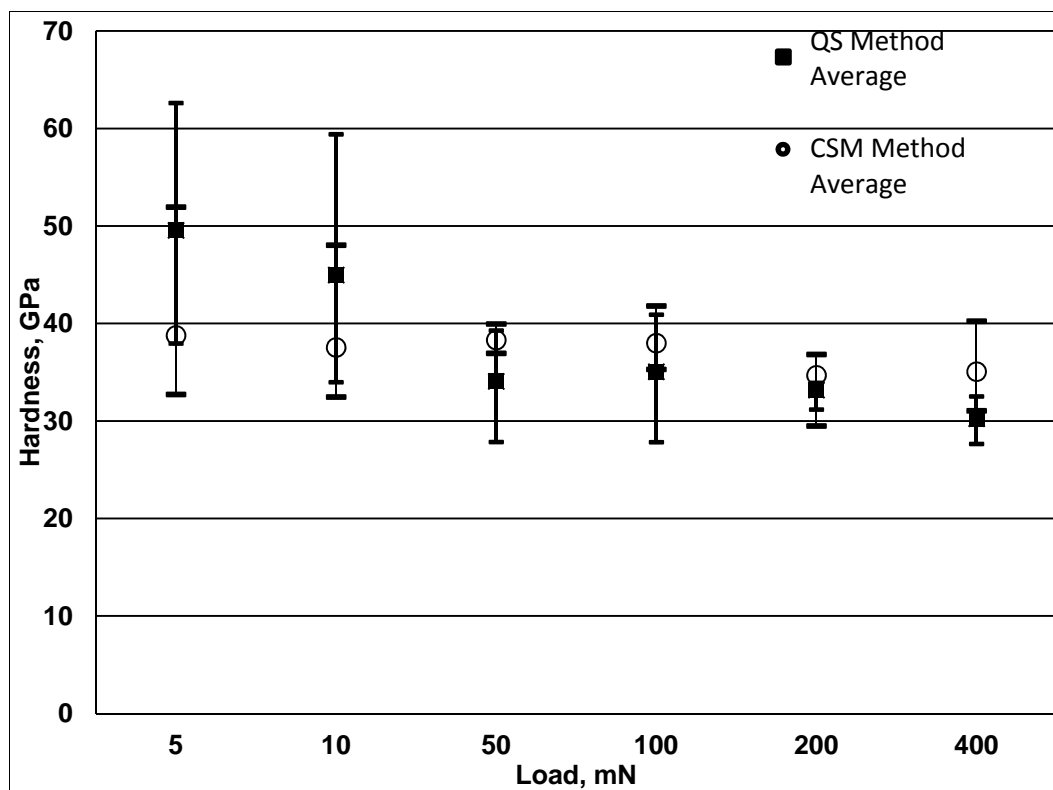


Figure 39. Oliver and Pharr (1992) calculated hardness versus peak indentation load. Bars represent maximum and minimum values of each data set.

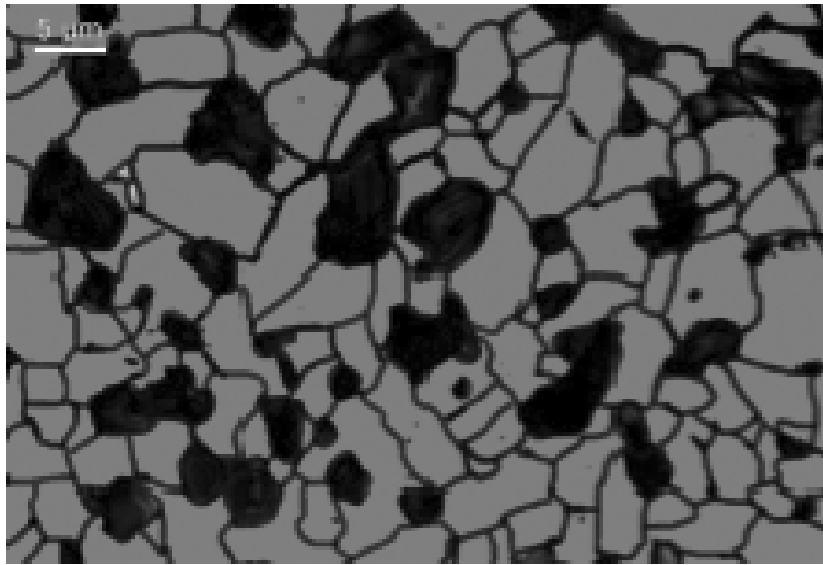


Figure 40. XRD pattern of commercially available SiC.

References

- Allen, J. B., C. F. Cornwell, N. J. Lee, C. P. Marsh, J. F. Peters, and C. R. Welch. 2011. Modeling Heat Transfer During Sublimation Growth of Silicon Carbide Single Crystals by Physical Vapor Transport. In *Advances in Ceramic Armor VII: Ceramic Engineering and Science Proceedings*, Volume 32, edited by J. J. Swab, S. Widjaja, and D. Singh. Hoboken, NJ: John Wiley.
- Allison, P. G., M. F. Horstemeyer, Y. Hammi, M.T. Tucker, H. R. Brown, and Y.-K. Hwang. 2011. Microstructure–property relations of a steel powder metal under varying temperatures, strain rates, and stress states. *Materials Science and Engineering A* 529(25):335-344.
- American Society for Testing and Materials. 2008. Standard test method for density of powder metallurgy (PM) materials containing less than two percent porosity. ASTM B311-08. West Conshohocken, PA: ASTM International.
- Anselmi-Tamburini, U., J. E. Garay, and Z. A. Munir. 2006. Fast low-temperature consolidation of bulk nanometric ceramic materials. *Scripta Materialia* 54(5):823-828.
- Anselmi-Tamburini, U., S. Gennari, J. E. Garay, and Z. A. Munir. 2005. Fundamental investigations on the spark plasma sintering/synthesis process: II. modeling of current and temperature distributions. *Materials Science and Engineering A* 394(1-2):139–148.
- Antou, G., G. Mathieu, G. Trolliard, and A. Maitre. 2009. Spark plasma sintering of zirconium carbide and oxycarbide: Finite element modeling of current density, temperature, and stress distributions. *Journal of Materials Research* 24(2):404–412.
- Askari, E., F. Bobaru, R. B. Lehoucq, M. L. Parks, S. A. Silling, O. Weckner. 2008. Peridynamics for multiscale materials modeling. *Journal of Physics: Conference Series* 125 (1) 012078.
- Barrett, D. L., J. P. McHugh, H. M. Hobgood, R. H. Hopkins, P. G. McMullin, R. C. Clarke, and W.J. Choyke. 1993. Growth of large SiC single crystals. *Journal of Crystal Growth* 128(1-4):358–362.
- Bazant, Z. P., and E. P. Chen. 1997. Scaling of structural failure. *Applied Mechanics Reviews*, ASME, 50(10):593-627.
- Biswas, K. 2009. Liquid phase sintering of SiC-ceramics. *Materials Science Forum, Sintering Fundamentals* 624:91-108.
- Braginsky, M., V. Tikare , and E. Olevsky. 2005. Numerical simulation of solid state sintering. *International Journal of Solids and Structures* 42(2) 621-636.
- Brahme, A., M. H. Alvi, D. Saylor, J. Fridy, A. D. Rollett. 2006. 3-D reconstruction of microstructure in a commercial purity aluminum. *Scripta Materialia* 55(1):75-80.

- Bratzel, G. H., S. W. Cranford, H. Espinosa, and M. J. Buehler. 2010. Bioinspired noncovalently crosslinked ‘fuzzy’ carbon nanotube bundles with superior toughness and strength. *Journal of Materials Chemistry*, First published on the web 23 September 2010.
- Brenner, D. W. 1990. Empirical potential for hydrocarbons for use in simulating the chemical vapor deposition of diamond films. *Physical Review B* 42(15): 9458–9471.
- Bridgman, P. W. 1923. The compressibility of the thirty metals as a function of pressure and temperature. *Proceedings of the American Academy of Arts and Sciences* 58(5): 164-242.
- Brown, W. F., Jr., and J. E. Srawley, J. E. 1966. Plane strain crack toughness testing of high strength metallic materials. ASTM Special Technical Publication No. 410. Philadelphia: American Society for Testing and Materials.
- Bruet, B. J. F., J. Song, M. C. Boyce, and C. Ortiz. 2008. Materials design principles of ancient fish armour. *Nature Materials* 7(9):748-756.
- Bubner, N., O. Klein, P. Philip, J. Sprekels, and K. Wilmaski. 1999. A transient model for the sublimation growth of silicon carbide single crystals. *Journal of Crystal Growth* 205(3):294-304.
- Buehler, M. J. 2010. Tu(r)ning weakness to strength. *nanotoday* 5(5):379–383.
- Cao, J. J., W. J. MoberlyChan, L. C. De Jonghe, C. J. Gilbert, and R. O. Ritchie. 1996. In situ toughened silicon carbide with Al-B-C additions. *Journal of the American Ceramic Society* 79(2):461-69.
- Chandler, M. Q., J. F. Peters, and D. Pelessone. 2010. Modeling nanoindentation of calcium-silicate-hydrate. *Transportation Research Record: Journal of the Transportation Research Board* 2142:67-74.
- Chen, Q.-S., H. Zhang, V. Prasad, Z. M. Balkas, and N. K. Yushin. 2001. Modeling of Heat Transfer and kinetics of physical vapor transport growth of silicon carbide crystals. *ASME Journal of Heat Transfer*, 123.
- Chenoweth, K., A. C. T. van Duin, and W. A. Goddard III, 2008. ReaxFF reactive force field for molecular dynamics simulations of hydrocarbon oxidation. *Journal of Physical Chemistry A* 112 (5): 1040–1053.
- Cornwell, C. F., and R. W. Noack. 2005. Realistic three-dimensional digital microstructure systems. In *Computational Methods and Experiments in Materials Characterization II* (ISSN 1743-3533), 51:251-257.
- CSC — IT Center for Science Ltd. Elmer: Open Source Finite Element Software for Multiphysical Problems. <http://www.csc.fi/elmer> accessed 01 May 2012.
- Dillon S. J., and M. P. Harmer. 2008. Demystifying the role of sintering additives with ‘complexion’. *Journal of the European Ceramic Society* 28(7):1485-1493.

- Espinosa, H. D., and S. Lee. 2002. Advances in microscale modeling of failure mechanisms in ceramics and fiber composites. In *The First Sino-US Joint Symposium on Multi-Scale Analysis in Material Sciences and Engineering*, Beijing, China, June 17-20, 2002, 1-22.
- Espinosa, H. D., and P. D. Zavattieri. 2003. A grain level model for the study of failure initiation and evolution in polycrystalline brittle materials; Part I: Theory and numerical implementation. Part II: Numerical examples. *Mechanics of Materials* 35(3-6): 333-394.
- Espinosa, H. D., J. E. Rim, F. Barthelat, and M. J. Buehler. 2009. Merger of structure and material in nacre and bone: Perspectives on *de Novo* Biomimetic Materials. *Progress in Materials Science* 54(8):1059-1100.
- Espinosa, H. D., A. L. Juster, F. J. Latourte, O. Y. Loh, D. Gregoire, and P. D. Zavattieri. 2011. Tablet-level origin of toughening in abalone shells and translation to synthetic composite materials. *Nature Communications* 2.
- Fratzl, P. 2007. Biomimetic materials research: What can we really learn from nature's structural materials? *Journal of the Royal Society Interface* 4(15):637-642.
- Garcia, A. P., D. Sen, and M. J. Buehler. 2010. Hierarchical silica nanostructures inspired by diatom algae yield superior deformability, toughness, and strength. *Metallurgical and Materials Transactions A*. published online 1 may 2012 DOI: 10.1007/s11661-010-0477-y.
- Griffith, A. A. 1921. the phenomena of rupture and flow in solids. *Philosophical Transactions of the Royal Society of London A* 221: 163-198.
- Groeber, M., S. Ghosh, M. D. Uchic, and D. M. Dimiduk. 2008. A framework for automated analysis and simulation of 3-D polycrystalline microstructures; Part 2: Synthetic structure generation. *Acta Materialia* 56(6):1274-1287.
- Guicciardi, S., A. Balbo, D. Sciti, C. Melandri, and G. Pezzotti. 2007. Nanoindentation characterization of SiC-based ceramics. *Journal of the European Ceramics Society* 27:1399-1404.
- Hofmann, D., M. Heinze, A. Winnacker, F. Durst, L. Kadinski, P. Kaufmann, Y. Makarov, M. Schäfer. 1995. 'On the sublimation growth of SiC bulk crystals: Development of a numerical process model.' *Journal of Crystal Growth* 146(1-4):214-219.
- Horstemeyer, M. F. 2009. Multiscale modeling: A review. In *Practical Aspects of Computational Chemistry*, edited by J. Leszczynski and M. K. Shukla, 87-135. New York: Springer Science+Business Media.
- Irwin, G. 1957. Analysis of stresses and strains near the end of a crack traversing a plate. *Journal of Applied Mechanics* 24, 361-364.
- Jackson, J. D. 1998. *Classical Electrodynamics*. New York: John Wiley.
- Kaneko, T. 1993. Growth kinetics of vapor-grown SiC. *Journal of Crystal Growth* 128(1-4):354-357.

- Kansa, E. J., H. E. Perlee, and R. F. Chaiken. 1977. Mathematical model of wood pyrolysis including internal forced convection. *Combustion and Flame* 29:311-324.
- Karandikar, P. G., G. Evans, and M. K. Aghajanian. 2008. Carbon nanotube and carbon fiber reinforced high toughness reaction bonded composites. In *Nanostructured Materials and Nanotechnology: Ceramic Engineering and Science Proceedings* 28(6):53-63.
- Kikuchi, H., R. K. Kalia, A. Nakano, P. Vashishta, P. S. Branicio, and F. Shimojo. 2005. Brittle dynamic fracture of crystalline cubic silicon carbide (3C-SiC) via molecular dynamics simulation. *Journal of Applied Physics* 98(10):103524 (4 pages).
- Kim, Y.-W., M. Mitomo, and H. Hirotsuru. 1997. Microstructural development of silicon carbide containing large seed grains. *Journal of the American Ceramic Society* 80(1):99-105.
- Klein, O., P. Philip, J. Sprekels, K. Wilmski. 2001. Radiation- and convection-driven transient heat transfer during sublimation growth of silicon carbide single crystals. *Journal of Crystal Growth*, 222:832-851.
- Kwon, H., M. Estili, K. Takagi, T. Miyazaki, A. Kawasaki. 2009. Combination of hot extrusion and spark plasma sintering for producing carbon nanotube reinforced aluminum matrix composites. *Carbon* 47(3):570-577.
- LaSalvia, J. C., J. Campbell, J.J. Swab, and J.W. McCauley. 2010. Beyond hardness: Ceramics and ceramic-based composites for protection. *JOM Journal of the Minerals, Metals and Materials Society* 62(1):16-23.
- Lee, S., R. Kraft, H. Thornburg, M. Groeber, Y. Choi, C. Woodward, S. Sintay, C. Cornwell, R. Noack, and A. D. Rollett. 2009. 3-D finite element meshes for materials microstructure. DoD High Performance Computing Modernization Program Users Group Conference, Proceedings, DoD High Performance, San Diego, 15-18 June.
- Lee, S.-B. J. M. Rickman, and A. D. Rollett. 2007. Three-dimensional simulation of isotropic coarsening in liquid phase sintering; I: A model. *Acta Materialia* 55(2):615-626.
- Lee, S.-G., Y.-W. Kim, and M. Mitomo. 2001. Relationship between microstructure and toughness of toughened silicon carbide ceramics. *Journal of the American Ceramic Society* 84(6):1347-53.
- Li, H., C.S. Ha, I. Kim. 2009. *Fabrication of Carbon Nanotube/SiO₂ and Carbon Nanotube/SiO₂/Ag Nanoparticles Hybrids by Using Plasma Treatment*. Nanoscale Research Letters, DOI 10.1007/s11671-009-9409-4, 13 August.
- Li, Z., and R. C. Bradt. 1987. The single-crystal elastic constants of cubic (3C) SiC to 1000° C. *Journal of Materials Science* 22(7):2557-2559.
- Lill, J., S. Sinnott, S. Stuart, J. Larentzos, and A. Rollett. 2011. Using AIREBO potentials to optimize properties of SiC composites reinforced with carbon nanotubes. PETTT Project: PP-CCM-KY01-011-P3 Final Technical Report.

- Lilov, S. K. 1993. Study of the equilibrium processes in the gas phase during silicon carbide sublimation. *Materials Science and Engineering B* 21(1):65–69.
- Ma, R.-H., Q.-S. Chen, H. Zhang, V. Prasad, C. M. Balkas, and N. K. Yushin. (2000). Modeling of silicon carbide crystal growth by physical vapor transport method. *Journal of Crystal Growth* 211(1-4):352–359.
- Maizza, G., S. Grasso, Y. Sakka, T. Noda, O. Ohashi. 2007. Relation Between Microstructure, properties and spark plasma sintering (SPS) parameters of pure ultrafine WC powder. *Science and Technology of Advanced Materials* 8(7-8):644-654.
- McWilliams, B, and A. Zavaliangos. 2008. Multi-phenomena simulation of electric field assisted sintering. *Journal of Materials Science* 43(14):5031–5503.
- Munir, Z. A., U. Anselmi-Tamburini, and M. Ohyanagi. 2006. The effect of electric field and pressure on the synthesis and consolidation of materials: A review of the spark plasma sintering method. *Journal of Materials Science* 41(3):763–777.
- Munoz, S., U. Anselmi-Tamburini. 2010. Temperature and Stress Fields Evolution during Plasma Sintering Processes. *J Mater Sci.*, 45, 6528-6539.
- Niu, Y., F. Xu, X. Hu, J. Zhao, H. Miao, X. Wu, and Z. Zhang. 2011. In situ investigation of the silicon carbide particles sintering. *Journal of Nanomaterials*. Volume 2011, 728617-728623.
- Oliver, W. C., and G. M. Pharr. 1992. An improved technique for determining hardness and elastic modulus using load and displacement sensing indentation experiments. *Journal of Material Research* 7:1564-1583.
- Olson, G. B. 1998. Systems design of hierarchically structured materials: advanced steels. *Journal of Computer-Aided Material Design* 4(3):143-156.
- Olson, G. B. 2000. New age of design. *Journal of Computer-Aided Material Design* 7(3):142-144.
- Pan, W., and J. Gong. 2010. Effects of sintering additives on the microstructure and mechanical properties of silicon nitride ceramic by GPS. *Advanced Material Research* 105-106:27-30.
- Parks, M. L., P. Seleson, S. J. Plimpton, R. B. Lehoucq, and S. A. Silling. 2010. *Peridynamics with LAMMPS: A User Guide vo.2 Beta*. Sandia Report 2010-5549. Albuquerque, NM, and Livermore, CA: Sandia National Laboratories.
- Pettifor, D. G. 1989. New many-body potential for the bond order. *Physical Review Letters* 63(22): 2480-2483.
- Plimpton, S. 1995. Fast parallel algorithms for short-range molecular dynamics. *Journal of Computational Physics* 117:1-19.
- Postek, E. W., T. Sadowski, and S. J. Hardy. 2005. The mechanical response of a ceramic polycrystalline material with inter-granular layer. In *VIII International Conference on Computational Plasticity, COMPLAS VIII*, Barcelona, Spain, 5-7 September 2005, edited by E. Oñate and D. R. J. Owen, 1-4.

- Reid, W. D. and D. L. Harris. 1958. Some further results on the Benard problem, *Phys. Fluids* 1:102-110.
- Rhee, H., M. F. Horstemeyer, Y. Hwang, H. Lim, H. El Kadiri, and W. Trim. 2009. A study on the structure and mechanical behavior of the *Terrapene carolina* Carapace: A pathway to design bio-inspired synthetic composites. *Materials Science and Engineering: C* 29(8): 2333-2339.
- Rim, J. E., P. Zavattieri, A. Juster, and H. D. Espinosa. 2011. Dimensional analysis and parametric studies for designing artificial nacre. *Journal of the Mechanical Behavior of Biomedical Materials* 4:190-211.
- Rollett, A. D., S.-B. Lee, R. Campman, and G. S. Rohrer. 2007. Three-dimensional characterization of microstructure by electron back-scatter diffraction. *Annual Review of Materials Research* 37:627-658.
- Rollett, A. D., D. Saylor, J. Fridy, B. S. El-Dasher, A. Brahme, S.-B. Lee, C. Cornwell, and R. Noack. 2004. Modeling polycrystalline microstructures in 3-D. In *Materials Processing and Design: Modeling, Simulation, and Applications, NUMIFORM 2004*, Edited by S. Ghosh, J. C. Castro, and J. K. Lee. 71-77. Melville, NY: American Institute of Physics.
- Saint-Gobain Advanced Ceramics. 2010. Hexoloy® SA Silicon Carbide; Technical Data. Bulletin Form No. B-1045. <http://www.hexoloy.com/data-sheets/silicon-carbide-products/pdf/b-1045.pdf>.
- M. Sasaki, Y. Nishio, S. Nishina, S. Nakashima, and H. Harima. 1998. Defect formation mechanism of bulk SiC. *Mater. Sci. Forum* 264-268, 41-44.
- Sass-Tisovskaya, M. 2009. Plasma Arc Welding Simulation with Open FOAM. Thesis for the Degree of Licentiate of Engineering, Department of Applied Mechanics. Goteborg, Sweden: Chalmers University of Technology.
- Schiotz, J., and K. W. Jacobsen. 2003. A Maximum in the strength of nanocrystalline Copper. *Science* 301(5638):1357-1359.
- Shan, T.-R., B. D. Devine, J. M. Hawkins, A. Asthagiri, S. R. Phillpot, and S. B. Sinnott. 2010. Second-generation charge-optimized many-body potential for Si/SiO₂ and amorphous silica. *Physical Review B* 82(23):235302.
- Shinozaki, S. S., J. Hangas, K. R. Carduner, and M. J. Rokosz. 1993. Correlation between microstructure and mechanical properties in silicon carbide with alumina addition. *J. Mater. Res.* 8(7):1635-1643.
- Shih, C. J., V. F. Nesterenko, and M. A. Meyers. 1998. High-strain-rate deformation and comminution of silicon carbide. *Journal of Applied Physics* 83(9):4660-4671.
- Silling, S. A., and E. Askari. 2005. A meshfree method based on the peridynamic model of solid mechanics. *Computers and Structures* 83 (17-18) 1526-1535.
- Srinivasan, M., and S. G. Seshadri. 1981. The Application of Single Edge Notched Beam and Indentation Techniques To Determine Fracture Toughness of Alpha Silicon Carbide. In *ASTM Symposium on Fracture Mechanics for Ceramics, Rock, and Concrete*, ASTM 23-24 June 1980, Philadelphia, PA.

- Steif, P. S., and A. Trojnecki. 1992. Bend strength versus tensile strength of fiber-reinforced ceramics. *Journal of the American Ceramic Society* 77(1):221-229.
- Steinhauser, M. O., K. Grass, E. Strassburger, and A. Blumen. 2008. Impact failure of granular materials–non-equilibrium multiscale simulations and high-speed experiments. *International Journal of Plasticity* 25(1): 161-182.
- Stuart, S. J., A. B. Tutein, and J. A. Harrison. 2000. A reactive potential for hydrocarbons with intermolecular interactions. *Journal of Chemical Physics* 112:6472.
- Trim, M. W., M. F. Horstemeyer, H. Rhee, J. Liao, and L. Williams. 2010. Energy absorbent materials design: lessons from nature 27th Army Science Conference, Orlando, FL, November 29-December 2, 2010.
- Tsurekawa, S., S. Nitta, H. Nakashima and H. Yoshinaga. 1995. Grain boundary structures in silicon carbide: verification of the extended boundary concept. *Interface Science* 3(1):75-84.
- van Duin, A. C. T., S. Dasgupta, F. Lorant, and W. A. Goddard III. 2001. ReaxFF: A reactive force field for hydrocarbons. *Journal of Physical Chemistry A* 105(41): 9396–9409.
- K. Vanmeensel, A. Laptev, J. Hennicke, J. Vleugels, and O. Van der Biest. Modeling of the temperature distribution during field-assisted sintering, *Acta Materialia*. 53, 4379-4388 (2005).
- Walker, L. S., V. R. Marotto, M. A. Rafiee, N. Koratkar, and E. L. Corral. 2011. Toughening in graphene ceramic composites. *ACS Nano* 5(4): 3182–3190. published online March 28, 2011.
- X. Wang, S. R. Casolco, G. Xu, and J. E. Garay. Finite element modeling of electric current activated sintering: the effect of coupled electrical potential, temperature and stress. *Acta Materialia*. 55, 3611–3622 (2007).
- Wang, Y., G. A. Voronin, T. W. Zerda, and A. Winiarski. 2006. SIC-CNT nanocomposites: high pressure reaction synthesis and characterization. *Journal of Physics: Condensed Matter* 18(1):275-282.
- Welch, C.R., M. Savoie, C.P. Marsh, C.F. Cornwell, R.M. Ebeling, R. Kirgan, N.J. Lee, R.W. Haskins, J.B. Allen. 2009. *Super Carbon Nanotube Tensile and Compressive Infrastructure Materials, Science and Technology White Paper*. 09 July 2009 Internal White Paper. Vicksburg, MS: U.S. Army Engineer Research and Development Center.
- Wu, B., V. Noveski, H. Zhang, R. Schlessner, S. Mahajan, S. Beaudoin, and Z. Sitar. 2005. Design of an RF-heated bulk AlN growth reactor: induction heating and heat transfer modeling. *Crystal Growth and Design* 5(4), 1491-1498.
- Xia, Z., W. A. Curtin, and B. W. Sheldon. 2004. “Fracture Toughness of Highly Ordered Carbon Nanotube/Alumina Nanocomposites.” *Journal of Engineering Materials and Technology*, ASME, 126(3):238-244.

- Yamamoto, G., M. Omori, T. Hashida, and H. Kirmura. 2008. A novel structure for carbon nanotube reinforced alumina composites with improved mechanical properties. *Nanotechnology* 19(31):315708.
- Yang, P. 2007. Dependency of deformation twinning on grain orientation in an fcc and an HCP metal. *Frontiers of Materials Science in China* 1(4): 331-341.
- Yao, H., M. Dao, T. Imholt, J. Huang, K. Wheeler, A. Bonilla, S. Suresh, and C. Ortiz. 2010. Protection mechanisms of the iron-plated armor of a deep-sea hydrothermal vent gastropod. *PNAS* 107(3):987-997.
- Yu, J., S. B. Sinnott, and S. R. Phillpot. 2007. Charge optimized many-body potential for the SiSiO₂ system. *Physical Review B* 75: 085311.
- A. Zavaliangos, J. Zhang, M. Krammer, and J. R. Groza. Temperature evolution during field activated sintering. *Mater Sci Eng A*, 379, 218-228 (2004).
- Zavattieri, P. D., and H. D. Espinosa. 2001. Grain level analysis of crack initiation and propagation in brittle materials. *Acta Materialia* 49(20):4291-4311.
- Zavattieri, P. D., and H. D. Espinosa. 2003. An Examination of the competition between bulk behavior and interfacial behavior of ceramics subjected to dynamic pressure-shear loading. *Journal of the Mechanics and Physics of Solids* 51(4):607-635.
- Zhan, G.-D., J. D. Kuntz, J. Wan, and A. K. Mukherjee. 2003. Single-wall carbon nanotubes as attractive toughening agents in alumina-based nanocomposites. *Nature Materials* 2:38-42.
- Zhang, K. S., M. S. Wu, R. Feng. 2005. Simulation of microplasticity-induced deformation in uniaxially strained ceramics by 3-D voronoi polycrystal modeling. *International Journal of Plasticity* 21 (4) 801-834.
- Zhou, Y., K. Hirao, M. Toriyama, Y. Yamauchi, and S. Kanzaki. 2001. Effects of intergranular phase chemistry on the microstructure and mechanical properties of silicon carbide ceramics densified with rare-earth oxide and alumina additions. *Journal of the American Ceramic Society* 84(7):1642-1644.

REPORT DOCUMENTATION PAGE				Form Approved OMB No. 0704-0188	
Public reporting burden for this collection of information is estimated to average 1 hour per response, including the time for reviewing instructions, searching existing data sources, gathering and maintaining the data needed, and completing and reviewing this collection of information. Send comments regarding this burden estimate or any other aspect of this collection of information, including suggestions for reducing this burden to Department of Defense, Washington Headquarters Services, Directorate for Information Operations and Reports (0704-0188), 1215 Jefferson Davis Highway, Suite 1204, Arlington, VA 22202-4302. Respondents should be aware that notwithstanding any other provision of law, no person shall be subject to any penalty for failing to comply with a collection of information if it does not display a currently valid OMB control number. PLEASE DO NOT RETURN YOUR FORM TO THE ABOVE ADDRESS.					
1. REPORT DATE (DD-MM-YYYY) August 2012		2. REPORT TYPE Final Report		3. DATES COVERED (From - To)	
4. TITLE AND SUBTITLE Towards Development of a Super Ceramic Composite - Initial Investigation into Improvement of Strength and Toughness of Polycrystalline Ceramics				5a. CONTRACT NUMBER	
				5b. GRANT NUMBER	
				5c. PROGRAM ELEMENT NUMBER	
6. AUTHOR(S) John F. Peters, Jeffrey P. Allen, Paul G. Allison, Thomas A. Carlson, Mei Q. Chandler, Charles F. Cornwell, Bryce D. Devine, Francis C. Hill, N. Jabari Lee, Charles P. Marsh, Peter B. Stynoski, Laura Walizer, and Charles R. Welch				5d. PROJECT NUMBER	
				5e. TASK NUMBER	
				5f. WORK UNIT NUMBER	
7. PERFORMING ORGANIZATION NAME(S) AND ADDRESS(ES) Geotechnical and Structures Laboratory U.S. Army Engineer Research and Development Center 3909 Halls Ferry Road, Vicksburg, MS 39180-6199; Construction Engineering Research Laboratory U.S. Army Engineer Research and Development Center 2902 Newmark Drive, Champaign, IL 61822; Information Technology Laboratory U.S. Army Engineer Research and Development Center 3909 Halls Ferry Road, Vicksburg, MS 39180-6199				8. PERFORMING ORGANIZATION REPORT NUMBER ERDC TR-12-9	
9. SPONSORING / MONITORING AGENCY NAME(S) AND ADDRESS(ES) U.S. Army Corps of Engineers Washington, DC 20314-1000				10. SPONSOR/MONITOR'S ACRONYM(S)	
				11. SPONSOR/MONITOR'S REPORT NUMBER(S)	
12. DISTRIBUTION / AVAILABILITY STATEMENT Approved for public release; distribution is unlimited.					
13. SUPPLEMENTARY NOTES					
14. ABSTRACT This report outlines the initial findings of the research team conducting the ERDC-directed research project "Nanoscale Studies of Polycrystalline Materials with Emphasis on Ceramics Syntheses." It provides an assessment of the state-of-the-art in the multi-scale simulation methods that can predict polycrystalline ceramic mechanical properties and ceramic sintering from basic physics and material structure. The report's findings will be used to identify strengths and weaknesses in the technology, to understand how the different simulation components must fit together, and to guide follow-on research programs towards the long-term development a ceramic composite that has fracture toughness and tensile strength approximately 5 times that of existing polycrystalline ceramics, such as silicon carbide or boron carbide. If such a ceramic composite were developed, then, based on current strength-to-weight and stiffness-to-weight ratios, it could replace steel and aluminum for most structural applications with an attendant two-thirds reduction in weight. This would have enormous impact on Army portable protective structures, equipment, and logistics. Key to this development is the growing capability in numerical simulations to predict material behavior based on atomic and crystalline morphology. Such simulations provide new insight into the causal relationships between material structure and material behavior. The simulations can guide both polycrystalline material design and synthesis methods such as sintering.					
15. SUBJECT TERMS Ceramic composite Ceramic syntheses		Multi-scale simulation methods Nanoscale studies of polycrystalline materials Polycrystalline Ceramics		Sintering of silicon carbide (SiC) Technical ceramics	
16. SECURITY CLASSIFICATION OF:			17. LIMITATION OF ABSTRACT	18. NUMBER OF PAGES	19a. NAME OF RESPONSIBLE PERSON: Bradley Johnson
a. REPORT Unclassified	b. ABSTRACT Unclassified	c. THIS PAGE Unclassified			19b. TELEPHONE NUMBER (include area code) (305) 650-0506